University of West Bohemia
Faculty of Applied Sciences

Thin-film alloys and non-oxide ceramics with amorphous or metastable crystalline structure

Ing. Michaela Červená

A thesis submitted for the degree of Doctor of Philosophy
in the field of Plasma Physics and Physics of Thin Films

Supervisor: prof. Ing. Petr Zeman, Ph.D.
Department of Physics

Plzeň 2021

Západočeská univerzita v Plzni
Fakulta aplikovaných věd

Tenkovrstvé slitiny a neoxidové keramiky s amorfní nebo metastabilní krystalickou strukturou

Ing. Michaela Červená

Disertační práce
k získání akademického titulu doktor
v oboru Fyzika plazmatu a tenkých vrstev

Školitel: prof. Ing. Petr Zeman, Ph.D.
Katedra fyziky

Plzeň 2021

Preface

I declare that I wrote this Ph.D. thesis by myself using the duly cited literature. All results reported here were obtained during my doctoral study at the Department of Physics of the Faculty of Applied Sciences at the University of West Bohemia since 2016. The thesis is submitted in a form of four scientific papers and one draft of the paper submitted for publication.

Plzeň, 9.7.2021 ....

Ing. Michaela Červená

Acknowledgments

First of all, I would like to express my thanks to my supervisor prof. Ing. Petr Zeman, Ph.D. for his patience, lots of helpful advice and valuable discussions during my Ph.D. study. I would also like to thank prof. RNDr. Jaroslav Vlček, CSc. for his support and motivation. My thanks go to Ing. Šárka Batková for creating a family atmosphere in our laboratory and for correcting my grammar. Last but not least, I would like to thank my family and my husband for their support during my whole study.

Contents

I Introduction ... 8

1. Alloys ... 9

1.1 Miscible and immiscible binary systems ... 9

1.2 Metallic glasses ... 11

2. Multicomponent high-temperature coatings ... 16

2.1. Hf–B–Si–C films ... 17

2.2. Hf–B–Si–C–N films ... 17

2.3. Protective coatings with rare-earth elements ... 19

3. References ... 20

II Aims ... 25

III Results ... 26

A On crystallization and oxidation behavior of $Zr_{54}Cu_{46}$ and $Zr_{27}Hf_{27}Cu_{46}$ thin-film metallic glasses compared to a crystalline $Zr_{54}Cu_{46}$ thin-film alloy ... 27

Abstract ... 28

1. Introduction ... 28

2. Experimental details ... 28

3. Results and discussion ... 29

3.1. Structure ... 29

3.2. Non-isothermal crystallization behavior ... 29

3.3. Isothermal oxidation behavior ... 31

4. Conclusions ... 33

Acknowledgments ... 34

References ... 34

B Impact of Al or Si addition on properties and oxidation resistance of magnetron sputtered Zr–Hf–Al/Si–Cu metallic glasses ... 35

Abstract ... 36

1. Introduction ... 36

2. Experimental details ... 37

3. Results and discussion ... 37

3.1. Elemental composition ... 38

3.2. Structure ... 38

3.3. Thermal behavior 38
3.4. Mechanical properties 42
3.5. Surface properties 42
3.6. Electrical resistivity 42
3.7. Oxidation resistance 43
4. Conclusions 43
Acknowledgments 43
References 43
C Metastable structures in magnetron sputtered W–Zr thin-film alloys 45
Abstract 46
1. Introduction 47
2. Experimental details 48
3. Results and discussion 49
3.1. Elemental composition 50
3.2. Structure 51
3.3. Microstructure and surface morphology 56
3.4. Hardness and residual stress 61
3.5. Electrical resistivity 63
4. Conclusions 64
Acknowledgments 65
References 65
D Self-formation of dual glassy-crystalline structure in magnetron sputtered W–Zr films 68
Abstract 69
Introduction 69
Experimental 69
Results and discussion 70
Conclusions 72
Declaration of competing interest 72
References 72
E Enhancement of high-temperature oxidation resistance and thermal stability of hard and optically transparent Hf–B–Si–C–N films by Y or Ho addition 73
Abstract 74

1. Introduction 74
2. Experimental 75
3. Results and discussion 75
3.1. Structure and properties of as-deposited films 76
3.2. Thermogravimetric measurements 76
3.3. Evolution of hardness and optical properties 77
3.4. DSC measurements 77
3.5. SEM imaging 78
4. Conclusions 79
CRediT authorship contribution statement 79
Declaration of Competing Interest 79
Acknowledgments 79
References 79
IV Conclusions 81
V Further publications of the candidate 84
1. Papers in impacted international journals 84
2. Contributions at international conferences 84
Abstract 87
Resumé 90

I Introduction

The continual development of technologies in all types of industries requires development in the field of preparation and characterization of new materials. In the last decades, considerable attention has been paid to the materials in a form of thin films prepared by magnetron sputtering technique. By depositing a thin film onto the surface of the underlying material, diverse properties can be improved such as mechanical, electrical, optical, chemical or thermal properties. By magnetron sputtering, which is non-equilibrium process, it is also possible to prepare films in the metastable state, which can lead to unique material properties.

The high-temperature behavior of the material is also crucial for miscellaneous applications, especially when used in severe environments. For this reason, the development of new materials with heat-resistant capabilities and the understanding of processes and phenomena in the material occurring at elevated temperature is very important.

This Ph.D. thesis therefore aims at the extension of knowledge in these fields. It deals with thin-film alloys and non-oxide ceramics with an amorphous or metastable crystalline structure. The main part is devoted to the high-temperature behavior of these materials investigated primarily by differential scanning calorimetry and thermogravimetry. The crystallization and oxidation behavior of Zr–Cu and Zr–Hf–Cu thin films is presented and discussed in Part A. The effect of the addition of Al or Si into Zr–Hf–Cu thin-film alloys on their thermal behavior and oxidation resistance is evaluated in Part B. Parts C and D are devoted to the preparation and characterization of binary W–Zr thin-film alloys with different metastable structures. Last Part E is focused on the characterization of the high-temperature oxidation resistance and thermal stability of hard and optically transparent Hf–B–Si–C–N films with an Y or Ho addition (2 – 3 at.%).

This thesis has been carried out within the framework of the projects SGS–2016–056 (2016–2018): New nanostructured thin-film materials formed by plasma technologies, SGS–2019–031 (2019–2021): New thin-film materials formed by advanced plasma technologies, GA ČR 16-18183S (2016–2018): Advanced surface coatings with enhanced properties and thermal stability, and MŠMT LO1506 (2015–2020): Sustainability support of the centre NTIS - New Technologies for the Information Society.

1. Alloys

In general, alloys can be characterized as a mixture of one metal and at least one other element [1,2]. The main reason for adding other elements to a pure metal is to improve its properties, such as mechanical [3,4] or corrosion properties [5]. Thin-film alloys can be prepared by magnetron sputtering, because it is possible, in principle, to sputter any metal (even those with a very high melting point) and thus prepare films with various compositions [6]. The resulting structure of the prepared alloys can be homogeneous (consisting of one solid solution or one intermetallic compound) or heterogeneous (consisting of a mixture of these phases) [7,8]. The difference between the crystal structure of a solid solution and an intermetallic compound is that the solid solution lattice is the same as the lattice of one of the constituent elements while the intermetallic compound lattice differs from those of the constituting elements.

From another point of view, the structure of the alloy may comprise stable or metastable phases. Moreover, the metastable phases may be amorphous or crystalline. Musil et al. [9] showed that magnetron sputtering is a very suitable technique for preparation of alloys with a high-temperature metastable phases, because it combines a sufficiently high temperature of the material at the atomic level during the deposition of thin film, which is necessary to form the high-temperature phase, and very fast cooling to room temperature, which prevents the conversion of the high-temperature phase to the low-temperature phase. They also stated that in order to prepare films with the high-temperature phase, it is necessary to use elements crystallizing in different crystal structures, such as Ti–Nb [10] or Ti–Cr [11].

1.1 Miscible and immiscible binary systems

As mentioned above, mixing a metal with another element can lead to several different results. In case of a miscible system, a solid solution or an intermetallic compound can be formed. On the other hand, two separate elements are preserved in an immiscible system. Of course, there can be systems with complete miscibility in liquid state and immiscibility in solid state.

According to the equilibrium W–Zr phase diagram [12], the W–Zr system, which will be discussed in this Ph.D. thesis, exhibits a complete liquid solubility, but almost negligible mutual solid solubility of Zr in α-W and W in α-Zr at ambient temperature (see Fig. 1). In a very narrow range of the elemental composition (33 – 35 at.% Zr), only a pure intermetallic phase W_2Zr can be formed [13]. At higher temperatures, the solubility is slightly increased to 3.56 at.% Zr in α-

W at peritectic temperature of 2160 °C and 3.98 at.% W in β-Zr at eutectic temperature of 1739 °C.

Since the generation of experimental phase diagrams is a relatively expensive and time-consuming process, it was necessary to define some rules for determining the mutual solubility of elements. It was found that the extent of solubility of substitutional solid solutions is determined by a few factors formulated by Hume-Rothery. First, the increasing difference in the electronegativity of both elements increases the tendency to form the intermetallic compound [14,15]. In other words, the mutual solubility of two metals increases with a decreasing difference of their electronegativities. Second, the size factor rule states that two metals, whose atomic radii differ by more than 15 %, have very low mutual solubility [15,16]. This is due to the difficulty of forming a mixed crystal with properly distributed atoms at the lattice sites, but it is not the case of an intermetallic compound that can still be formed. Third, a metal with a smaller number of valence electrons dissolves in a metal with a higher number of valence electrons more likely than the other way round.

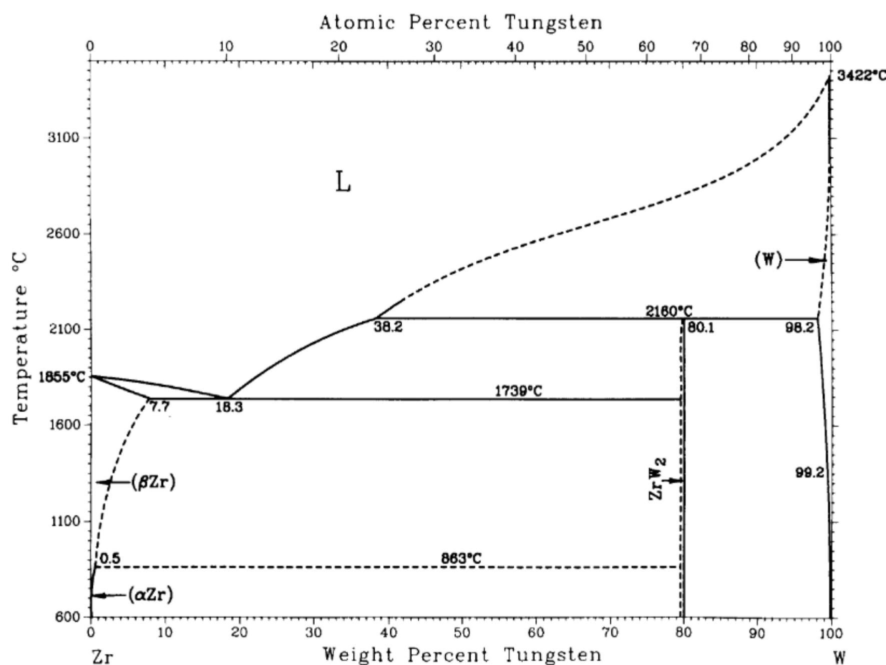

Fig. 1. The equilibrium W–Zr phase diagram [12].

Because the applicability of the individual rules (or their combination) was not always satisfactory [17], Miedema et al. introduced a new empirical model with a very high certainty (around 98 %) in predicting the alloying behavior of two metal elements [18,19]. In this model, the value of the formation enthalpy is used to predict the miscibility or immiscibility of the system

– a miscible system corresponds to a negative formation enthalpy, while an immiscible system to a positive formation enthalpy. Zhang et al. [20] showed that the results of Miedema's model are very accurate in case of highly positive (> 10 kJ/mol) or highly negative (< -10 kJ/mol) binary alloy systems, but their inaccuracy increases when the formation enthalpy is close to 0.

1.2 Metallic glasses

One of the very interesting groups of alloys are metallic glasses. Metallic glasses are amorphous alloys with neither a long-range periodical arrangement nor a completely random arrangement of atoms in their structure. By using molecular dynamic simulations, it has been shown that they exhibit a short- or medium-range ordering of atoms in a form of base units called icosahedral clusters [21–23]. Metallic glasses are isotropic and have a homogeneous structure without lattice defects and grain boundaries [24]. The first metallic glass (specifically, the binary $Au_{80}Si_{20}$) was prepared by Klement et al. in 1960 by rapid quenching of the alloy from the molten state [25]. It was found that the cooling rate necessary for the preparation of a metallic glass from melt or gas must be high enough (in order of 10^3 – 10^6 K/s) to prevent the formation of nuclei and crystal growth and to preserve the amorphous structure of the alloys [26,27]. This leads to the preparation of a materials that have very interesting and unique properties, such as high yield strength and elastic strain, good corrosion and wear resistance or smooth surface [28–30].

The difference between the conventional amorphous materials and metallic glasses is in the process of their crystallization. While the structure of a conventional amorphous material transforms directly to crystalline with increasing temperature, in case of metallic glasses it is a bit more complicated. The crystallization process of metallic glasses can be investigated by differential scanning calorimetry (DSC) [31,32]. Fig. 2 presents a detail of the DSC curve of $Zr_{54}Cu_{46}$ thin-film metallic glass (TFMG) annealed to 600 °C in argon (the direction of an exothermic reaction is upwards). One can recognize a characteristic decrease of the heat flow before the onset of the exothermic crystallization peak (see Fig. 2). The onset of this decrease determines the glass transition temperature T_g and onset of the exothermic crystallization peak then corresponds to the crystallization temperature T_c. The region between these temperatures is called a supercooled liquid region ΔT. These three values are characteristic for the metallic glasses and strongly depend on their elemental composition.

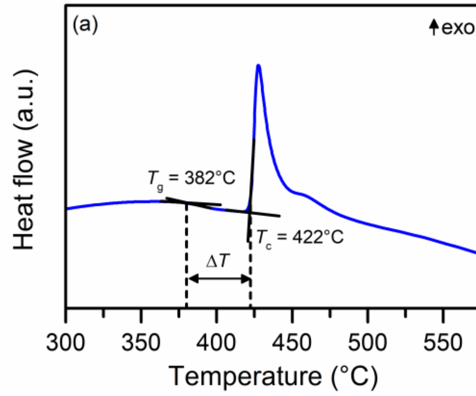

Fig. 2. DSC curve of $Zr_{54}Cu_{46}$ TFMG annealed to 600 °C in argon. The glass transition temperature T_g, crystallization temperature T_c and supercooled liquid region ΔT are highlighted.

Metallic glasses can also exhibit a "self-healing" effect [33,34]. It means that the surface defects (scratches, dents or indentation imprints) with a size of a few micrometers can be partially or completely recovered by annealing of the metallic glass within the supercooled liquid region because of their viscous flow in this region. As can be seen in Fig. 3, annealing of the Zr-based metallic glass within ΔT for 1 minute leads to a decrease of the indentation depth (by almost 14 % in this case). This capability can be very beneficial when the metallic glasses are used as an antiscratching coatings.

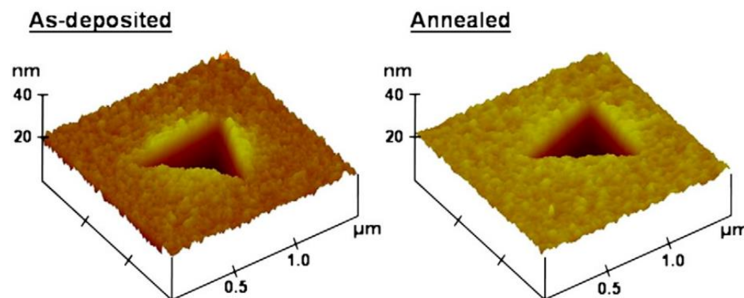

Fig. 3. Atomic force microscopy images of the indentation imprint in Zr-based TFMG before and after annealing at 460°C for 1 minute [34].

The amorphous structure of metallic glasses without any columns and grain boundaries exhibits enhanced corrosion resistance compared to the crystalline alloys, because the grain-boundary-free microstructure serves as a more effective diffusion barrier. The surface of metallic glasses is very smooth (below 1.5 nm for Zr–Cu [35]), so they can be used as a surface layer to reduce the surface roughness of the base material [36]. For example, the $Zr_{51}Cu_{32}Al_{10}Ni_7$ surface layer

reduced the surface roughness of the ZK60 magnesium alloy from 54.6 to 24.2 nm and significantly increased the fatigue life of the material [37]. It was also found that the surface roughness of the Zr-based metallic glasses can be further reduced by annealing of the film within ΔT for 1 minute [38].

In addition, the mechanism of plastic deformation of metallic glasses differs from the mechanism of conventional crystalline metals. The plastic deformation in crystalline metals takes place by the dislocation slip. On the other hand, the metallic glasses, which are free of dislocations, exhibit higher elastic limit compared to the crystalline metals (i.e. are able to store more elastic energy) and the plastic deformation proceeds via shear-banding in their case. The shear bands, which can be clearly seen around the indent in Fig. 4, occur as a consequence of relieving of an accumulated localized plastic strain during the deformation resulting in the shear-softening of the deformed area compared to the surrounding undeformed area. Further deformation then leads to the catastrophic failure of the material. However, it should be emphasized that the metallic glasses have higher yield strengths than crystalline metallic films and larger ductility than ceramics [39–41].

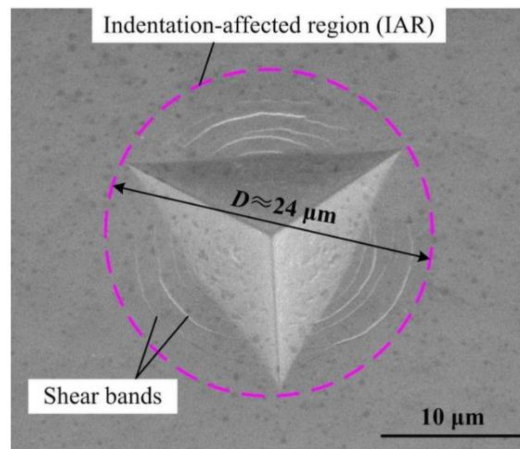

Fig. 4. Scanning electron microscopy image of the indent made on the $Zr_{51.2}Ti_{13.8}Cu_{12.5}Ni_{10}Be_{22.5}$ bulk metallic glass at a load of 1000 mN [41].

In terms of preparation, Inoue [42] proposed three empirical rules to obtain a glassy alloy by various casting processes. The alloy should be composed of three or more elements, where the atomic size of the main elements differs by more than 12 %, and they should exhibit a negative heat of mixing. Of course, binary metallic glasses can be prepared as well, but the cooling rate required to preserve the amorphous structure must be higher than in the previous case.

Since magnetron sputtering allows high-cooling rates ($\geq 10^6$ K/s), the research on TFMGs started in our labs a few years ago. A systematic study has been done on the binary Zr–Cu system because this system is characterized one of the highest glass forming ability. This is caused by a large difference in the atomic sizes of Zr and Cu (1.6 Å for Zr and 1.28 Å for Cu) combined with a large negative heat of mixing (-23 kJ/mol) [43]. Zeman et al. [35] found that the Zr–Cu TFMGs can be prepared with the Cu content between approximately 30 and 65 at.%. The glass transition temperature increased gradually with increasing Cu content and a clear correlation between the evolution of the crystallization and glass transition temperature and mechanical properties with increasing Cu content was observed (Fig. 5). In addition, benefits of sputtering of Cu in a high-power impulse magnetron sputtering (HiPIMS) regime were demonstrated, e.g., a moderate compressive stress, an enhanced hardness (up to 7.5 GPa), very smooth (surface roughness < 1 nm) and hydrophobic (water contact angle up to 108°) surface of the Zr–Cu TFMGs.

In the recent paper published by Houška et al. [44], these experimentally achieved results were correlated with and explained by extensive molecular dynamics simulations of the atom-by-atom growth. After the confirmation of compositional ranges corresponding to crystalline and amorphous Zr–Cu films, a short- and medium-range order of the amorphous films was evaluated. An increasing flux of deposited Cu atoms resulted in an increasing coordination of Zr and Cu elements in the films, increasing packing factor, increasing number of shortest-path network rings of length 3 and 5, and increasing number of 555 triplets in the common neighbor statistics (Fig. 5). Changes in the two latter quantities correspond to an increasing number of icosahedral clusters, which correlates well not only with an increasing densification and hardness, but also with an increasing glass transition temperature (for compositions which exhibit the glass transition) and crystallization temperature.

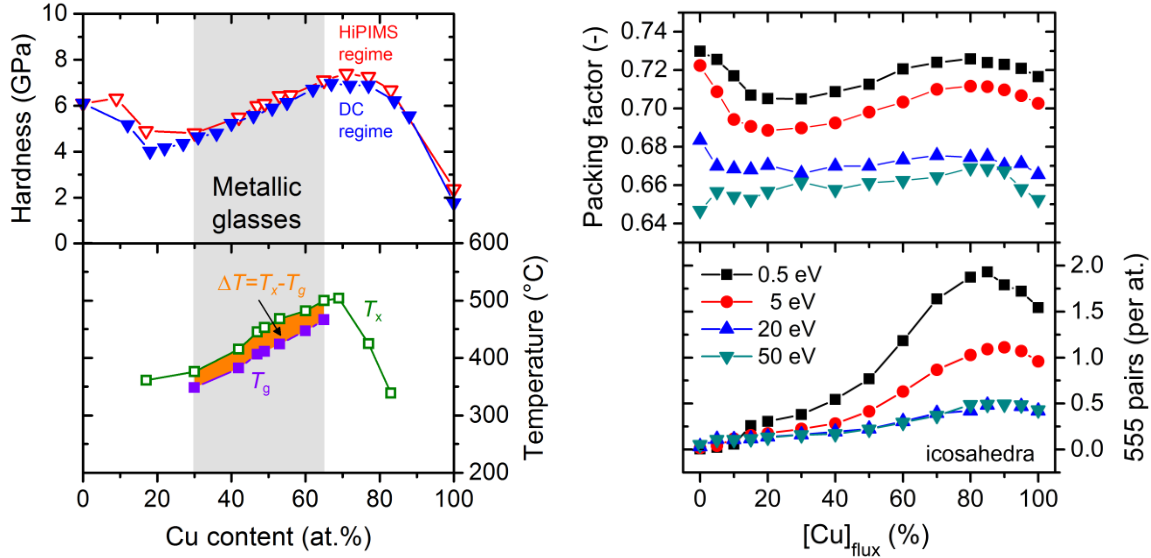

Fig. 5. Dependence of hardness (HiPIMS and DC regimes), crystallization (T_x) and glass transition (T_g) temperature (HiPIMS regime) of Zr–Cu films on the Cu content (experimental data) [35] and the dependence of the average packing factor and the number of 555 triplets (icosahedral clusters) on the film-forming flux composition and energy (calculation data) [44]. Correlations of the data are well visible.

To investigate the effect of an incorporation of Hf into binary Zr–Cu films on the properties and thermal behavior, Zítek et al. [45] performed an experimental study of the Zr–Hf–Cu system in our labs. It was shown that a gradual substitution of Hf for Zr is beneficial in terms of an enhanced hardness and thermal stability of the glassy state. This was explained by increasing average bond energy as Hf with a more covalent character of bonds gradually substitutes Zr in the amorphous structure. Tuning of the elemental composition of the Zr–Hf–Cu TFMGs allowed also to control the supercooled liquid region in a very wide temperature range (405 – 533 °C) and to maintain a high oxidation resistance even in the supercooled liquid region.

Part A of this Ph.D. thesis follows up on these previous studies and focuses on the investigation of the crystallization behavior of $Zr_{54}Cu_{46}$ and $Zr_{27}Hf_{27}Cu_{46}$ TFMGs and their oxidation behavior compared to a crystalline $Zr_{54}Cu_{46}$ thin-film alloy.

Since alloying with Al or Si has been reported to affect the crystallization temperature and also the width of the supercooled liquid region of Zr- or Cu-based metallic glasses [46,47] and no Zr–Hf–Al/Si–Cu films have been studied yet, we paid attention also to these two quaternary systems. Zítek et. al [48] prepared Zr–Hf–Al/Si–Cu thin-film alloys with up to 17 at.% Al or up to 12 at.% Si. It was found that all films were amorphous and that the addition of Al or Si

enhanced mechanical properties of the films. In addition, the films were very smooth, electrically conductive and also hydrophobic up to 17 at.% Al or 6 at.% Si. Part B of this Ph.D. thesis is then focused on the investigation of the thermal behavior and oxidation resistance of these quaternary Zr–Hf–Al/Si–Cu films.

Another binary system with a larger negative enthalpy of mixing and difference in atomic sizes of both elements is the W–Zr system. So far, only a few studies have dealt with magnetron sputtered W–Zr alloys and, moreover, only in a limited range of the elemental composition. Bhattarai et al. [49] investigated the corrosion resistance of W–Zr thin-film alloys with 14 – 76 at.% Zr, while Horwat et al. focused on the investigation of mechanical properties of W_2Zr Laves phase and W–Zr thin films with 19 – 57 at.% Zr [50] and on the effect of structure evolution on the electrical and optical properties in the same range of the elemental composition [51].

Part C of this Ph.D. thesis is devoted to the preparation of W–Zr thin-film alloys in a very wide range of the elemental composition (3 – 99 at.% Zr) and to the investigation of relationships between the structure and the microstructure, surface morphology, mechanical properties and electrical resistivity in detail. Part D is then focused on self-formation of a unique dual glassy-crystalline structure in this system at 28 at.% Zr.

2. Multicomponent high-temperature coatings

An effective way to obtain new materials with a unique combination of material properties is the preparation of multicomponent coatings. Very often, the stability of these properties at elevated temperature and even in oxidizing environment is required. From this point of view, one of the interesting groups are multicomponent ceramic coatings. In combination with a high optical transparency, these materials can be used as a high-temperature passive protection of optical and optoelectronic devices [52,53]. On the other hand, materials with high oxidation resistance and thermally stable electrical conductivity are suitable candidates for capacitive pressure or tip clearance sensors in harsh environments [54,55].

2.1 Hf–B–Si–C films

Recently, Hf–B–Si–C materials have been prepared in the form of thin films by non-reactive magnetron sputtering in our labs [56,57]. The main motivation was to prepare highly electrically conductive thin-film materials with an improved oxidation behavior. Therefore, the effect of Si addition (0 – 50 % Si in the target erosion area) on the structure, mechanical and electrical properties, and oxidation resistance was investigated. It was shown that a pure Hf–B–C film exhibited a nanocolumnar structure, high hardness (up to 37 GPa) and low electrical resistivity (1.8×10^{-6} Ωm). A gradual addition of Si led to a structure amorphization and a significant improvement of the oxidation resistance up to 30 % Si fraction (see oxidation thermogravimetric curves in Fig. 6). The addition of up to 7.5 % Si did not affect the hardness of the films, which was around 34 – 37 GPa. For the films with 10 – 50 % Si fraction, the hardness gradually decreased down to 12 GPa. The electrical resistivity gradually increased with increasing Si content but remained within the order of 10^{-6} Ωm. Based on these results, Hf–B–Si–C film prepared at 20 % Si fraction was chosen for further investigation, because it exhibited a sufficiently high hardness (above 20 GPa) and a high oxidation resistance at least up to 800 °C.

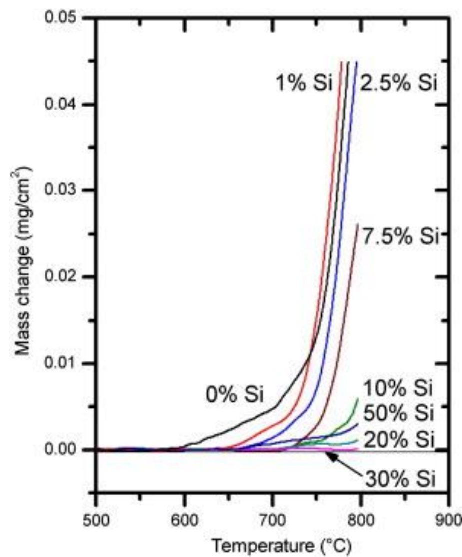

Fig. 6. Thermogravimetric oxidation curves of as-deposited Hf–B–Si–C films measured in synthetic air at a heating rate of 10 °C/min. The films were prepared at different Si fractions (0 – 50%) in the target erosion area [57].

2.2 Hf–B–Si–C–N films

In order to further improve the oxidation resistance above 1000 °C and to limit the B release from the films during annealing in air, N was added into the Hf–B–Si–C films [58]. The most

promising films were prepared with 20 % Si fraction in the target erosion area and with 15 % and 25 % N_2 fraction in Ar–N_2 gas mixture. Both films exhibited an amorphous structure, sufficiently high hardness (20 – 22 GPa), a very high oxidation resistance up to 1500 °C (mass change ≤ 5 mg/cm^2) and an electrical conductivity ($Hf_7B_{23}Si_{22}C_6N_{40}$ film prepared at 15 % N_2) or an optical transparency ($Hf_6B_{21}Si_{19}C_4N_{47}$ film prepared at 25 % N_2). A very interesting result is that such a small difference in the elemental composition leads to a large difference in the electrical and optical properties of the films.

As can be seen in the left side of Fig. 7, the microstructure of the electrically conductive $Hf_7B_{23}Si_{22}C_6N_{40}$ film after annealing to 1500 °C consists of a two-layer structure – an original film and a protective surface oxide layer. The 360 nm thick surface oxide layer is composed of m- and t- or o-HfO_2 nanocrystallites, which are embedded in a SiO_2-based amorphous matrix. While m-HfO_2 nanocrystallites are located predominantly near the surface, t- or o-HfO_2 nanocrystallites are distributed throughout the thickness of the oxide layer (see the right side of Fig. 7). It can be seen that the structure of the original film changed after annealing to 1500 °C from amorphous to partially crystalline and consisted of HfCN and HfB_2 nanocrystallites surrounded by Si_3N_4 and BN boundary phases [59].

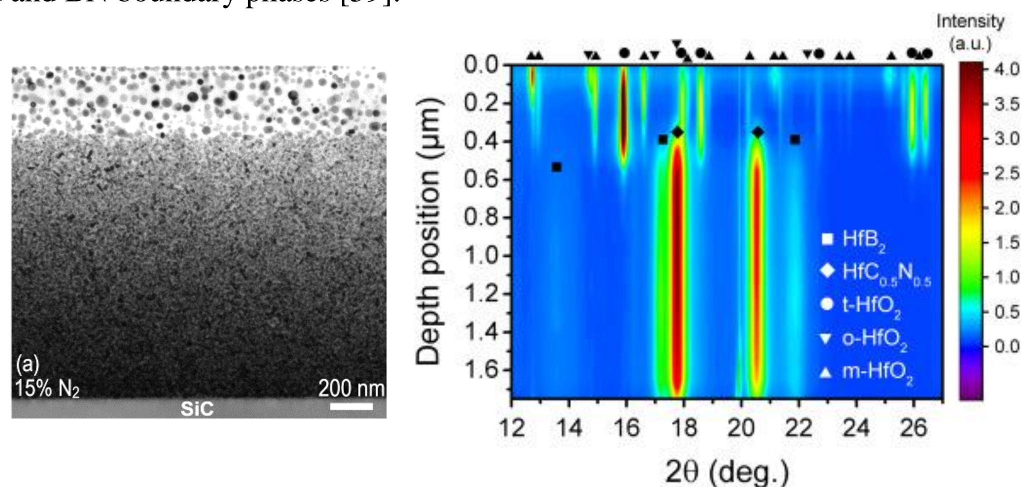

Fig. 7. Cross-section HRTEM image of the $Hf_7B_{23}Si_{22}C_6N_{40}$ film annealed in air up to 1500 °C (left side) [58] and a phase distribution plot across the thickness this film. The plot was obtained by azimuthal integration of Debye–Scherrer rings measured by cross-sectional X-ray nanodiffraction. Zero depth on the vertical axis corresponds to the surface of the oxidized film (right side) [59].

A detailed examination of the structure of the $Hf_7B_{23}Si_{22}C_6N_{40}$ film after annealing to 1500 °C by high-resolution transmission electron microscopy (HRTEM) revealed that the HfB_2 and HfCN nanocrystallites form a sandwich structure, where the strips of HfB_2 nanocrystals are in the middle and HfCN nanocrystallites are placed on both sides, as can be seen in Fig. 8. Based

on this geometry, it appears that the HfB_2 forms first and then serves as a low energy nucleation site for the coherent growth of the HfCN phase [60].

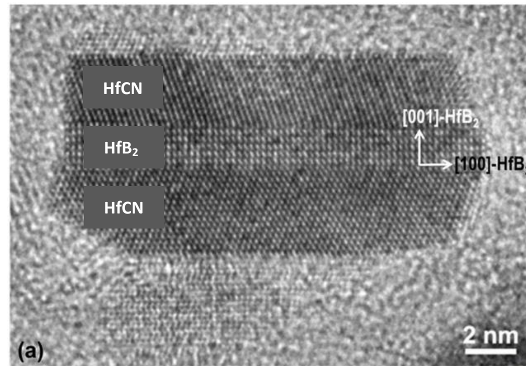

Fig. 8. HRTEM image of a HfB_2 and HfCN sandwich structure. Adjusted according to [60].

Fig. 9 shows the microstructure of the optically transparent $Hf_6B_{21}Si_{19}C_4N_{47}$ film after annealing to 1500 °C, where the two-layer structure was also created. The surface oxide layer with the thickness of 370 nm is very similar to the oxide layer of $Hf_7B_{23}Si_{22}C_6N_{40}$ film mentioned above. In addition, the structure of the original film remains amorphous even after the annealing to 1500 °C, which indicates an extraordinary thermal stability of the structure of this film [58,60].

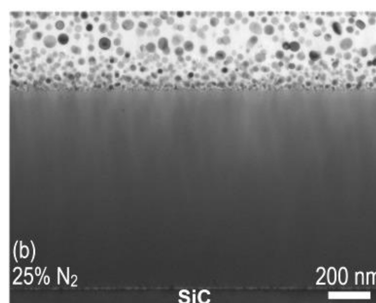

Fig. 9. Cross-section HRTEM images of the $Hf_6B_{21}Si_{19}C_4N_{47}$ film annealed in air up to 1500 °C [58].

2.3 Protective coatings with rare-earth elements

Recently, it has been reported in the literature that monosilicates and disilicates of rare-earth elements (such as Y, Yb or Ho) are suitable for use as protective barrier layers of hot sections of gas turbine engines, because they exhibit a higher stability during the reaction with high-temperature steam compared to pure silica [61–63]. In addition, large atomic radius of Y or Ho might also be beneficial to retard the diffusion during the oxidation and crystallization processes.

Therefore, part E of this Ph.D. thesis follows up on the previous studies of Hf–B–Si–C–N films and is focused on the investigation of the effect of Y or Ho addition (2 – 3 at.%) into Hf–B–Si–C–N films on their oxidation resistance and thermal stability at temperatures significantly exceeding 1000 °C.

3. References

[1] W.D. Callister, D.G. Rethwisch, Materials Science and Engineering: An Introduction, 8th ed., Wiley, 2009.

[2] D.R. Askeland, W.J. Wright, The Science and Engineering of Materials, 7th ed., Cengage Learning, 2015.

[3] B. Ma, X. Qi, R. Li, R. Zhang, H. Shang, The Zr alloying effect on microstructure evolution and mechanical properties of nanostructured Al-Zr alloyed films, J. Alloys Compd. 858 (2021) 157707. doi:10.1016/j.jallcom.2020.157707.

[4] S.X. Liang, L.X. Yin, M.Z. Ma, R. Jing, P.F. Yu, Y.F. Zhang, B.A. Wang, R.P. Liu, A multi-component Zr alloy with comparable strength and Higher plasticity than Zr-based bulk metallic glasses, Mater. Sci. Eng. A. 561 (2013) 13–16. doi:10.1016/j.msea.2012.10.061.

[5] B. Yan, J. Tan, D. Wang, J. Qiu, X. Liu, Surface alloyed Ti–Zr layer constructed on titanium by Zr ion implantation for improving physicochemical and osteogenic properties, Prog. Nat. Sci. Mater. Int. 30 (2020) 635–641. doi:10.1016/j.pnsc.2020.09.006.

[6] D. Depla, S. Mahieu, J.E. Greene, Chapter 5 - Sputter Deposition Processes, in: P.M.B.T.-H. of D.T. for F. and C. (Third E. Martin (Ed.), Handb. Depos. Technol. Film. Coatings, William Andrew Publishing, Boston, 2010: pp. 253–296. doi:10.1016/B978-0-8155-2031-3.00005-3.

[7] H. Ibach, H. Lüth, Solid-State Physics: An Introduction to Principles of Materials Science, 4th ed., Springer Science & Business Media, 2009.

[8] A. Ovchinnikov, V. Smetana, A.V. Mudring, Metallic alloys at the edge of complexity: structural aspects, chemical bonding and physical properties, J. Phys. Condens. Matter. 32 (2020). doi:10.1088/1361-648X/ab6b87.

[9] J. Musil, Kos, S. Zenkin, Z. Čiperová, D. Javdošňák, R. Čerstvý, β- (Me1, Me2) and MeNx films deposited by magnetron sputtering: Novel heterostructural alloy and compound films, Surf. Coatings Technol. 337 (2018) 75–81. doi:10.1016/j.surfcoat.2017.12.057.

[10] E.D. Gonzalez, T.C. Niemeyer, C.R.M. Afonso, P.A.P. Nascente, Ti-Nb thin films deposited by magnetron sputtering on stainless steel, J. Vac. Sci. Technol. A Vacuum, Surfaces, Film. 34 (2016) 021511. doi:10.1116/1.4940753.

[11] F. Zhang, C. Li, M. Yan, J. He, Y. Yang, F. Yin, Microstructure and nanomechanical properties of co-deposited Ti-Cr films prepared by magnetron sputtering, Surf. Coatings Technol. 325 (2017) 636–642. doi:10.1016/j.surfcoat.2017.07.005.

[12] H. Okamoto, M.E. Schlesinger, E.. Mueller, eds., ASM Handbook: Alloy Phase Diagrams, ASM International, 2016. doi:10.31399/asm.hb.v03.a0006217.

[13] R.F. Domagala, D.J. McPherson, M. Hansen, Systems Zirconium-Molybdenum and Zirconium-Wolfram, JOM. 5 (1953) 73–79. doi:10.1007/BF03397454.

[14] L. Brewer, A most striking confirmation of the Engel metallic correlation, Acta Metall. 15 (1967) 553–556. doi:10.1016/0001-6160(67)90088-0.

[15] W. Hume-Rothery, Phase stability in metals and alloys, McGraw-Hill, New York, 1967.

[16] W. Hume-Rothery, The sizes of atoms in metallic crystals, Physica. 15 (1949) 29–33. doi:https://doi.org/10.1016/0031-8914(49)90021-X.

[17] J.T. Waber, K. Gschneider Jr., A.C. Larson, M.Y. Prince, Prediction of Solid Solubility in Metallic Alloys, Trans. Met. Soc., AIME. 227 (1963) 717–723.

[18] A.R. Miedema, A simple model for alloys, 33 (1973).

[19] A.R. Miedema, The electronegativity parameter for transition metals: Heat of formation and charge transfer in alloys, J. Less Common Met. 32 (1973) 117–136. doi:https://doi.org/10.1016/0022-5088(73)90078-7.

[20] R.F. Zhang, X.F. Kong, H.T. Wang, S.H. Zhang, D. Legut, S.H. Sheng, S. Srinivasan, K. Rajan, T.C. Germann, An informatics guided classification of miscible and immiscible binary alloy systems, Sci. Rep. 7 (2017) 1–12. doi:10.1038/s41598-017-09704-1.

[21] D.Z. Chen, C.Y. Shi, Q. An, Q. Zeng, W.L. Mao, W.A. Goddard, J.R. Greer, Fractal atomic-level percolation in metallic glasses, Science (80-.). 349 (2015) 1306 LP – 1310. doi:10.1126/science.aab1233.

[22] G.A. Almyras, C.E. Lekka, N. Mattern, G.A. Evangelakis, On the microstructure of the Cu65Zr35 and Cu35Zr65 metallic glasses, Scr. Mater. 62 (2010) 33–36. doi:https://doi.org/10.1016/j.scriptamat.2009.09.019.

[23] H.W. Sheng, W.K. Luo, F.M. Alamgir, J.M. Bai, E. Ma, Atomic packing and short-to-medium-range order in metallic glasses, Nature. 439 (2006) 419–425. doi:10.1038/nature04421.

[24] J.P. Chu, J.C. Huang, J.S.C. Jang, Y.C. Wang, P.K. Liaw, Thin film metallic glasses: Preparations, properties, and applications, JOM. 62 (2010) 19–24. doi:10.1007/s11837-010-0053-3.

[25] W. Klement, R.H. Willens, P. Duwez, Non-crystalline structure in solidified Gold-Silicon alloys, Nature. 187 (1960) 869–870. doi:10.1038/187869b0.

[26] M.J. Kramer, H. Mecco, K.W. Dennis, E. Vargonova, R.W. McCallum, R.E. Napolitano, Rapid solidification and metallic glass formation – Experimental and theoretical limits, J. Non. Cryst. Solids. 353 (2007) 3633–3639. doi:https://doi.org/10.1016/j.jnoncrysol.2007.05.172.

[27] F. Hayat, J. Yin, A. Tabassum, H. Hou, S. Lan, T. Feng, Effects of cooling rate and sub-Tg annealing on Ni80P20 metallic glass: A molecular dynamic (MD) study, Comput. Mater. Sci. 179 (2020) 109681. doi:https://doi.org/10.1016/j.commatsci.2020.109681.

[28] H.-R. Jiang, J.-Y. Hu, N. Neuber, B. Bochtler, B. Adam, S.S. Riegler, M. Frey, L. Ruschel, W. Lu, A.-H. Feng, R. Busch, J. Shen, Effect of sulfur on the glass-forming ability, phase transformation, and thermal stability of Cu-Zr-Al bulk metallic glass, Acta Mater. (2021) 116923. doi:https://doi.org/10.1016/j.actamat.2021.116923.

[29] K.R. Lim, J.M. Park, S.J. Kim, E.-S. Lee, W.T. Kim, A. Gebert, J. Eckert, D.H. Kim, Enhancement of oxidation resistance of the supercooled liquid in Cu–Zr-based metallic glass by forming an amorphous oxide layer with high thermal stability, Corros. Sci. 66 (2013) 1–4. doi:https://doi.org/10.1016/j.corsci.2012.09.018.

[30] M. Telford, The case for bulk metallic glass, Mater. Today. 7 (2004) 36–43. doi:10.1016/S1369-7021(04)00124-5.

[31] G. Höhne, W. Hemminger, H.-J. Flammersheim, Differential Scanning Calorimetry, Springer-Verlag Berlin Heidelberg, 1996. doi:10.1007/978-3-662-03302-9.

[32] Q. Zheng, Y. Zhang, M. Montazerian, O. Gulbiten, J.C. Mauro, E.D. Zanotto, Y. Yue, Understanding Glass through Differential Scanning Calorimetry, Chem. Rev. 119 (2019) 7848–7939. doi:10.1021/acs.chemrev.8b00510.

[33] P. Yiu, W. Diyatmika, N. Bönninghoff, Y.C. Lu, B.Z. Lai, J.P. Chu, Thin film metallic glasses: Properties, applications and future, J. Appl. Phys. 127 (2020). doi:10.1063/1.5122884.

[34] J.P. Chu, J.S.C. Jang, J.C. Huang, H.S. Chou, Y. Yang, J.C. Ye, Y.C. Wang, J.W. Lee, F.X. Liu, P.K. Liaw, Y.C. Chen, C.M. Lee, C.L. Li, C. Rullyani, Thin film metallic glasses: Unique properties and potential applications, Thin Solid Films. 520 (2012) 5097–5122. doi:10.1016/J.TSF.2012.03.092.

[35] P. Zeman, M. Zítek, Zuzjaková, R. Čerstvý, Amorphous Zr-Cu thin-film alloys with metallic glass behavior, J. Alloys Compd. (2017). doi:10.1016/j.jallcom.2016.12.098.

[36] C.M. Lee, J.P. Chu, W.Z. Chang, J.W. Lee, J.S.C. Jang, P.K. Liaw, Fatigue property improvements of Ti-6Al-4V by thin film coatings of metallic glass and TiN: A comparison study, Thin Solid Films. 561 (2014) 33–37. doi:10.1016/j.tsf.2013.08.027.

[37] C.H. Chang, C.M. Lee, J.P. Chu, P.K. Liaw, S.C.J. Jang, Fatigue property improvements of ZK60 magnesium alloy: Effects of thin film metallic glass, Thin Solid Films. 616 (2016) 431–436. doi:10.1016/j.tsf.2016.09.010.

[38] J.P. Chu, C.M. Lee, R.T. Huang, P.K. Liaw, Zr-based glass-forming film for fatigue-property improvements of 316L stainless steel: Annealing effects, Surf. Coatings Technol. 205 (2011) 4030–4034. doi:10.1016/j.surfcoat.2011.02.040.

[39] Y.M. Lu, B.A. Sun, L.Z. Zhao, W.H. Wang, M.X. Pan, C.T. Liu, Y. Yang, Shear-banding Induced Indentation Size Effect in Metallic Glasses, Sci. Rep. 6 (2016) 1–12. doi:10.1038/srep28523.

[40] A.L. Greer, Y.Q. Cheng, E. Ma, Shear bands in metallic glasses, Mater. Sci. Eng. R Reports. 74 (2013) 71–132. doi:10.1016/j.mser.2013.04.001.

[41] H. Huang, J. Yan, Multi-scale dimple creation on metallic glass by a two-step method involving nanoindentation and polishing, Appl. Surf. Sci. 462 (2018) 565–574. doi:10.1016/j.apsusc.2018.08.180.

[42] A. Inoue, Stabilization of metallic supercooled liquid and bulk amorphous alloys, Acta

Mater. 48 (2000) 279–306. doi:10.1016/S1359-6454(99)00300-6.

[43] M. Apreutesei, P. Steyer, L. Joly-Pottuz, A. Billard, J. Qiao, S. Cardinal, F. Sanchette, J.M. Pelletier, C. Esnouf, Microstructural, thermal and mechanical behavior of co-sputtered binary Zr–Cu thin film metallic glasses, Thin Solid Films. 561 (2014) 53–59. doi:10.1016/j.tsf.2013.05.177.

[44] J. Houska, P. Machanova, M. Zitek, P. Zeman, Molecular dynamics and experimental study of the growth, structure and properties of Zr–Cu films, J. Alloys Compd. 828 (2020) 154433. doi:10.1016/j.jallcom.2020.154433.

[45] M. Zítek, P. Zeman, Š. Zuzjaková, M. Kotrlová, R. Čerstvý, Tuning properties and behavior of magnetron sputtered Zr-Hf-Cu metallic glasses, J. Alloys Compd. 739 (2018) 848–855. doi:10.1016/J.JALLCOM.2017.12.301.

[46] T.L. Cheung, C.H. Shek, Thermal and mechanical properties of Cu-Zr-Al bulk metallic glasses, J. Alloys Compd. 434–435 (2007) 71–74. doi:10.1016/j.jallcom.2006.08.109.

[47] H. Choi-Yim, R. Busch, W.L. Johnson, The effect of silicon on the glass forming ability of the Cu47Ti34Zr11Ni8 bulk metallic glass forming alloy during processing of composites, J. Appl. Phys. 83 (1998) 7993–7997. doi:10.1063/1.367981.

[48] M. Zítek, P. Zeman, M. Kotrlová, R. Čerstvý, Impact of Al or Si addition on properties and oxidation resistance of magnetron sputtered Zr–Hf–Al/Si–Cu metallic glasses, J. Alloys Compd. 772 (2019). doi:10.1016/j.jallcom.2018.09.069.

[49] J. Bhattarai, E. Akiyama, H. Habazaki, A. Kawashima, K. Asami, K. Hashimoto, Electrochemical and xps studies of the corrosion behavior of sputter-deposited amorphous W-Zr alloys in 6 and 12 M HCl solutions, Corros. Sci. 39 (1997) 355–375. doi:10.1016/S0010-938X(97)83351-3.

[50] D. Horwat, E. Jimenez-Pique, J.F. Pierson, S. Migot, M. Dehmas, M. Anglada, High hardness, low Youngs modulus and low friction of nanocrystalline ZrW 2 Laves phase and Zr 1-xW x thin films, J. Phys. Chem. Solids. 73 (2012) 554–558. doi:10.1016/j.jpcs.2011.12.009.

[51] D. Horwat, M. Dehmas, E. Aubry, J. Zollinger, S. Migot, J.F. Pierson, Properties of nanocrystalline and nanocomposite WxZr1-x thin films deposited by co-sputtering, Intermetallics. 17 (2009) 421–426. doi:10.1016/j.intermet.2008.11.020.

[52] J. Kalaš, R. Vernhes, S. Hřeben, J. Vlček, J.E. Klemberg-Sapieha, L. Martinu, High-temperature stability of the mechanical and optical properties of Si–B–C–N films prepared by magnetron sputtering, Thin Solid Films. 518 (2009) 174–179. doi:10.1016/J.TSF.2009.06.017.

[53] J. Vlček, P. Calta, P. Steidl, P. Zeman, R. Čerstvý, J. Houška, J. Kohout, Pulsed reactive magnetron sputtering of high-temperature Si–B–C–N films with high optical transparency, Surf. Coatings Technol. 226 (2013) 34–39. doi:10.1016/J.SURFCOAT.2013.03.033.

[54] D.J. Young, J. Du, C. a Zorman, W.H. Ko, L. Fellow, A. Single-crystal, Capacitive Pressure Sensor, 4 (2004) 464–470.

[55] T. Fabian, F.B. Prinz, G. Brasseur, Capacitive sensor for active tip clearance control in a palm-sized gas turbine generator, IEEE Trans. Instrum. Meas. 54 (2005) 1133–1143. doi:10.1109/TIM.2005.847233.

[56] M. Zhang, J. Jiang, P. Mareš, J. Houška, J. Vlček, E.I. Meletis, Effect of the Si content on the microstructure of hard, multifunctional Hf-B-Si-C films prepared by pulsed magnetron sputtering, Appl. Surf. Sci. 357 (2015) 1343–1354. doi:10.1016/j.apsusc.2015.09.249.

[57] J. Kohout, J. Vlček, J. Houška, P. Mareš, R. Čerstvý, P. Zeman, M. Zhang, J. Jiang, E.I. Meletis, Š. Zuzjaková, Hard multifunctional Hf-B-Si-C films prepared by pulsed magnetron sputtering, Surf. Coatings Technol. 257 (2014) 301–307. doi:10.1016/j.surfcoat.2013.12.007.

[58] V. Šímová, J. Vlček, Š. Zuzjaková, J. Houška, Y. Shen, J. Jiang, E.I. Meletis, V. Peřina, Magnetron sputtered Hf–B–Si–C–N films with controlled electrical conductivity and optical transparency, and with ultrahigh oxidation resistance, Thin Solid Films. 653 (2018) 333–340. doi:10.1016/j.tsf.2018.03.064.

[59] P. Zeman, Š. Zuzjaková, P. Mareš, R. Čerstvý, M. Zhang, J. Jiang, E.I. Meletis, J. Vlček, Superior high-temperature oxidation resistance of magnetron sputtered Hf–B–Si–C–N film, Ceram. Int. 42 (2016) 4853–4859. doi:10.1016/J.CERAMINT.2015.11.171.

[60] Y. Shen, J.C. Jiang, P. Zeman, V. Šímová, J. Vlček, E.I. Meletis, Microstructure evolution in amorphous Hf-B-Si-C-N high temperature resistant coatings after annealing to 1500 °C in air, Sci. Rep. 9 (2019) 1–11. doi:10.1038/s41598-019-40428-6.

[61] K.N. Lee, D.S. Fox, N.P. Bansal, Rare earth silicate environmental barrier coatings for SiC/SiC composites and Si3N4 ceramics, J. Eur. Ceram. Soc. 25 (2005) 1705–1715. doi:10.1016/j.jeurceramsoc.2004.12.013.

[62] B.K. Jang, F.J. Feng, K.S. Lee, E. García, A. Nistal, N. Nagashima, S. Kim, Y.S. Oh, H.T. Kim, Thermal behavior and mechanical properties of Y2SiO5 environmental barrier coatings after isothermal heat treatment, Surf. Coatings Technol. 308 (2016) 24–30. doi:10.1016/j.surfcoat.2016.09.088.

[63] Z. Tian, L. Zheng, Z. Li, J. Li, J. Wang, Exploration of the low thermal conductivities of γ-Y2Si2O7, β-Y2Si2O7, β-Yb2Si2O7, and β-Lu2Si2O7 as novel environmental barrier coating candidates, J. Eur. Ceram. Soc. 36 (2016) 2813–2823. doi:10.1016/j.jeurceramsoc.2016.04.022.

II Aims

The Ph.D. thesis is focused on investigation of the high-temperature behavior of binary Zr–Cu, ternary Zr–Hf–Cu and quaternary Zr–Hf–Al/Si–Cu TFMGs and senary Hf–B–Si–Y/Ho–C–N ceramic films with an amorphous structure, and on preparation and characterization of thin-film alloys from the binary W–Zr system. The high-temperature behavior was primarily characterized by differential scanning calorimetry and high-resolution thermogravimetry.

Main aims of the Ph.D. thesis are formulated as follows:

1) To investigate and compare the crystallization and oxidation behavior of Zr–Cu and Zr–Hf–Cu TFMGs and the oxidation behavior of a Zr–Cu TFMG and a crystalline Zr–Cu film of the identical composition. To determine the activation energy of the crystallization and oxidation process.

2) To systematically investigate the effect of an addition of Al or Si into Zr–Hf–Cu TFMGs on the glass transition temperature, the width of the supercooled liquid region, the thermal stability and the oxidation behavior of the prepared Zr–Hf–Al/Si–Cu films.

3) To prepare W–Zr thin-film alloys in a very wide composition range and to identify structures and phases, including metastable ones, that can be prepared by non-equilibrium process of magnetron sputtering. In addition, to find relationships between the structure and the microstructure, surface morphology, mechanical properties, and electrical resistivity of the films.

4) To investigate the effect of an addition of small amount (2 – 3 at.%) of Y or Ho into hard and optically transparent Hf–B–Si–C–N amorphous films on their high-temperature oxidation resistance and on the thermal stability of their structure, hardness, and optical properties upon annealing in air and inert gases.

III Results

The results are presented in a form of four scientific papers (Parts A, B, D and E) published in international journals and one draft of the paper submitted for publication in international journal (Part C). These papers summarize the most important results obtained during my Ph.D. study at the Department of Physics, Faculty of Applied Sciences University of West Bohemia in Pilsen since September 2016.

I carried out all measurements of the high-temperature behavior of binary, ternary and quaternary Zr–Cu based TFMGs (Parts A and B) and senary Hf–B–Si–Y/Ho–C–N ceramic films (Part E) by differential scanning calorimetry and high-resolution thermogravimetry. I evaluated measured data and actively participated in the interpretation of the results. I also actively participated in the evaluation of the results of other analyses supporting the interpretation of the high-temperature behavior of the films. I wrote the first version of the papers (Parts A and E) and actively participated in completing and writing of the final version of the papers (Parts A, B and E). Note that the films investigated in Parts A, B and E were deposited by other Ph.D. students.

I carried out all depositions of the W–Zr thin-film alloys (Parts C and D) by magnetron co-sputtering. I measured the elemental composition, thickness, residual stress, mechanical and electrical properties of the films. I performed imaging of the films in top and cross-sectional views. In addition, I actively participated in the interpretation of the results of other analyses. I wrote the first version of the paper (Part C) and actively participated in completing and writing of the final version of the paper (Parts C and D).

A

On crystallization and oxidation behavior of $Zr_{54}Cu_{46}$ and $Zr_{27}Hf_{27}Cu_{46}$ thin-film metallic glasses compared to a crystalline $Zr_{54}Cu_{46}$ thin-film alloy

M. Kotrlová, P. Zeman, Š. Zuzjaková, M. Zítek

Journal of Non-Crystalline Solids 500 (2018) 475–481

Journal of Non-Crystalline Solids 500 (2018) 475–481

Contents lists available at ScienceDirect

Journal of Non-Crystalline Solids

journal homepage: www.elsevier.com/locate/jnoncrysol

On crystallization and oxidation behavior of $Zr_{54}Cu_{46}$ and $Zr_{27}Hf_{27}Cu_{46}$ thin-film metallic glasses compared to a crystalline $Zr_{54}Cu_{46}$ thin-film alloy

M. Kotrlová, P. Zeman*, Š. Zuzjaková, M. Zítek

Department of Physics and NTIS – European Centre of Excellence, University of West Bohemia, Univerzitní 8, 306 14 Plzeň, Czech Republic

ARTICLE INFO

Keywords:
Zr–Cu
Zr–Hf–Cu
Metallic glass
Crystallization kinetics
Oxidation kinetics
Activation energy

ABSTRACT

Amorphous $Zr_{54}Cu_{46}$ and $Zr_{27}Hf_{27}Cu_{46}$ thin-film metallic glasses were prepared by non-reactive magnetron co-sputtering of Zr, Hf and Cu in pure argon. Several as-deposited $Zr_{54}Cu_{46}$ films were post-annealed in high vacuum to create a crystalline thin-film alloy of the identical composition. The non-isothermal crystallization behavior of the amorphous $Zr_{54}Cu_{46}$ and $Zr_{27}Hf_{27}Cu_{46}$ films and the effect of a substitution of Hf for Zr on the crystallization process were studied by differential scanning calorimetry. The activation energy of the crystallization was obtained by the Kissinger–Akahira–Sunose method. The results show that the activation energy of the $Zr_{27}Hf_{27}Cu_{46}$ film was higher for all conversion fractions, which indicates that the substitution of Hf for Zr enhances the thermal stability of the glassy state. Considerable attention was also paid to the isothermal oxidation behavior of the amorphous and crystalline $Zr_{54}Cu_{46}$, and amorphous $Zr_{27}Hf_{27}Cu_{46}$ films investigated by thermogravimetric analysis. It was shown that all oxidation curves in the temperature range from 400 to 575 °C obeyed the parabolic law. The activation energy of the oxidation process determined by the Arrhenius equation for the oxidation rate constants was found to be the highest for the $Zr_{27}Hf_{27}Cu_{46}$ film, which indicates that its surface oxide layer is a more effective barrier against the diffusion of species.

1. Introduction

Metallic glasses have attracted considerable interest in recent years due to their unique properties such as high tensile strength, high elastic strain and hardness, temperature-independent electrical resistivity, low wear and high corrosion resistance, excellent surface finishing, and biocompatibility [1–3]. Metallic glasses are amorphous materials with a short-range order on the atomic scale, which gives rise to some specific properties such as homogeneity, isotropy, and absence of grain boundaries [4,5] compared to conventional crystalline materials.

Zr- and Cu-based metallic glasses are one of the most studied systems because of their high crystallization temperature and a wide supercooled liquid region [6,7]. Their unique properties make them attractive for miscellaneous applications. An important prerequisite to use them in industry is their ability to resist an oxidizing environment at elevated temperatures. Recently, several studies have been conducted with the aim to investigate the oxidation behavior and determine the oxidation kinetics of Zr- and Cu-based glassy and/or crystalline thin films [8–12]. To better understand the thermal behavior of the Zr- and Cu-based metallic glasses, several studies have been also focused on the crystallization kinetics, most of them on isothermal [13–15] or a combination of isothermal and non-isothermal kinetics [16,17] and only a few on non-isothermal kinetics [18–20].

In the present work, thermally activated processes in $Zr_{54}Cu_{46}$ and $Zr_{27}Hf_{27}Cu_{46}$ films prepared by magnetron co-sputtering of Zr, Hf and Cu in argon atmosphere are systematically investigated. We use differential scanning calorimetry to study the non-isothermal crystallization behavior of the amorphous $Zr_{54}Cu_{46}$ and $Zr_{27}Hf_{27}Cu_{46}$ thin-film metallic glasses and to evaluate the influence of a substitution of Hf for Zr on the crystallization process and its activation energy. We pay considerable attention to thermogravimetric analysis of the oxidation behavior of amorphous and crystalline $Zr_{54}Cu_{46}$, and amorphous $Zr_{27}Hf_{27}Cu_{46}$ films. We determine oxidation rate constants and activation energies of the relevant oxidation processes. The selection of the elemental composition of the films investigated was done based on our previous studies [21,22] reporting on properties and thermal behavior of these films.

2. Experimental details

Amorphous $Zr_{54}Cu_{46}$ and $Zr_{27}Hf_{27}Cu_{46}$ thin films were deposited by non-reactive magnetron co-sputtering of Zr (99.5% purity), Hf (99.9% purity) and Cu (99.99% purity) targets in pure argon at a pressure of 0.53 Pa. Magnetrons with the Zr and Hf targets were operated in dc

* Corresponding author.
E-mail address: zemanp@kfy.zcu.cz (P. Zeman).

https://doi.org/10.1016/j.jnoncrysol.2018.09.004
Received 13 July 2018; Received in revised form 29 August 2018; Accepted 2 September 2018
Available online 07 September 2018
0022-3093/ © 2018 Elsevier B.V. All rights reserved.

regimes while the magnetron with the Cu target was operated in a high-power impulse regime. The films were deposited onto Si(100) wafers and molybdenum foils (0.1 mm in thickness) held at a floating potential without any external heating. The substrates were rotated above the targets at a speed of 40 rpm and located at a target-to-substrate distance of 150 mm. More technical details concerning the preparation of Zr—Cu and Zr—Hf—Cu films are given in our previous papers [21,22].

In order to create a $Zr_{54}Cu_{46}$ crystalline alloy film of the identical composition for the comparison study, several as-deposited films were post-annealed at 465 °C (above the crystallization temperature of 422 °C) for 5 min in a high-vacuum chamber (evacuated down to a base pressure of 5×10^{-6} Pa).

The crystallization behavior of the $Zr_{54}Cu_{46}$ and $Zr_{27}Hf_{27}Cu_{46}$ films was investigated by differential scanning calorimetry (DSC) using a Setaram Labsys DSC 1600 system. Approximately 5 µm thick film deposited onto the molybdenum foil was relatively easily delaminated from this substrate. Obtained freestanding film fragments of a total mass of 5 mg were then inserted into a 100 µl alumina crucible covered with a lid. An identical uncharged crucible was used as a reference. The DSC measurements were carried out at different heating rates (10, 20, 30 and 40 °C/min) in argon (a flow rate of 1 l/h) in the temperature range from room temperature up to 600 °C. The cooling rate was in all cases the same as the heating rate. Each run was immediately followed by a second run under the same conditions to serve as a baseline. The calorimeter was calibrated by melting of Pb, Zn and Al standards with purity of 99.998 ± 0.001%. After heating, the film fragments were mechanically ground in an agate mortar to provide a fine powder used for X-ray diffraction measurements.

The oxidation behavior of the $Zr_{54}Cu_{46}$ and $Zr_{27}Hf_{27}Cu_{46}$ films with an area of $1 \times 1\ cm^2$ was investigated by high-resolution thermogravimetry (TG) using a symmetrical Setaram TAG 2400 system. The TG analysis was carried out in synthetic air (a flow rate of 1 l/h) with dynamical heating in the temperature range from room temperature up to 800 °C and isothermal annealing at various temperatures in the range from 400 °C to 575 °C for 3 h. The heating rate was set to 10 °C/min upon dynamical heating and 50 °C/min before reaching the isothermal temperature. The cooling rate was set to 30 °C/min in both cases. The Si (100) substrates used were coated on one side only. After subtracting the thermogravimetric signal corresponding to oxidation of the uncoated sides, the resulting thermogravimetric curve gives us the thermogravimetric signal of the film only.

The structure of the as-deposited and annealed films on the Si(100) substrate and powdered heated films was characterized by X-ray diffraction (XRD) using a PANalytical X'Pert PRO diffractometer in the Bragg–Brentano configuration using the Cu K_α radiation ($\lambda = 0.154187$ nm).

The elemental composition of the as-deposited films on the Si(100) substrate was analyzed by a Hitachi SU-70 scanning electron microscope operated at a primary electron energy of 20 keV using a Thermo Scientific UltraDry energy dispersive spectrometer (EDS). Zr, Hf and Cu standards were used for the quantitative analysis. The error of the elemental analysis was established to be 1 at.%.

The thickness of the surface oxide layer was determined by a J.A. Woollam Co. variable angle spectroscopic ellipsometer. The measurements were performed in the wavelength range from 300 to 2000 nm using angles of incidence of 65°, 70° and 75° in reflection.

3. Results and discussion

The following section is divided into three subsections. The first one characterizes the structure of all three films investigated in this paper. The second one is focused on the non-isothermal crystallization behavior of the $Zr_{54}Cu_{46}$ and $Zr_{27}Hf_{27}Cu_{46}$ thin-film metallic glasses and on the discussion of the influence of a Hf substitution for Zr on the crystallization process. The third one describes the effect of the structure and the elemental composition on the oxidation behavior and kinetics of the crystalline $Zr_{54}Cu_{46}$ film and amorphous $Zr_{54}Cu_{46}$ and $Zr_{27}Hf_{27}Cu_{46}$ films.

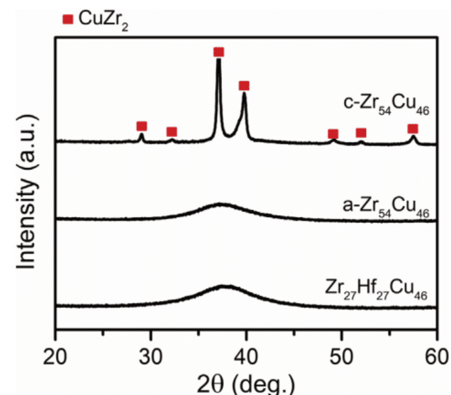

Fig. 1. XRD patterns of as-deposited (a-$Zr_{54}Cu_{46}$ and $Zr_{27}Hf_{27}Cu_{46}$) and annealed (c-$Zr_{54}Cu_{46}$) films.

3.1. Structure

XRD patterns of two as-deposited films, $Zr_{54}Cu_{46}$ and $Zr_{27}Hf_{27}Cu_{46}$, and one $Zr_{54}Cu_{46}$ film annealed at 465 °C for 5 min in high vacuum are shown in Fig. 1. It can be seen that the as-deposited films are X-ray amorphous while the annealed film is crystalline. The XRD patterns of the amorphous films contain one very broad peak of a low intensity at the position $2\theta \approx 38°$, which confirms a disordered structure of the films lacking any long-range periodic arrangement of atoms. On the other hand, the XRD pattern of the annealed film is characterized by the occurrence of several diffraction peaks that can be assigned to the crystalline tetragonal $CuZr_2$ (PDF Card No. 00-018-0466) phase. The thickness of all films investigated was around 2 µm.

3.2. Non-isothermal crystallization behavior

The non-isothermal crystallization behavior of the amorphous $Zr_{54}Cu_{46}$ and $Zr_{27}Hf_{27}Cu_{46}$ was investigated by differential scanning calorimetry. Both films were heated from room temperature up to 600 °C with a heating rate of 10, 20, 30 and 40 °C/min in pure argon as freestanding film fragments. The non-isothermal crystallization behavior was investigated only for the amorphous films because there was no pronounced response upon heating in case of the crystalline film, as expected.

Fig. 2 shows the most relevant part of DSC curves of both films heated with a heating rate of 30 °C/min. The glass transition temperature T_g, crystallization temperature T_c and the supercooled liquid region $\Delta T = T_c – T_g$ are highlighted on the DSC curves. One can recognize that both films exhibit the glass transition, which gives evidence about their glassy behavior. The substitution of Hf for Zr has nearly no effect on the width of the supercooled liquid region (close to 40 °C for both films) but it shifts the onset of the glass transition and the crystallization to higher temperatures. The enhanced thermal stability of the glassy state of the $Zr_{27}Hf_{27}Cu_{46}$ film compared to the $Zr_{54}Cu_{46}$ film may be explained by a more covalent character of the metallic-covalent bonds of Hf (a higher average bond energy) and also by a lower mobility of Hf during diffusion-controlled processes (approximately twice higher atomic mass of Hf than Zr). Furthermore, the crystallization process of the $Zr_{54}Cu_{46}$ film (Fig. 2a) is characterized by two overlapping exothermic peaks of a higher and lower intensity in contrast to the $Zr_{27}Hf_{27}Cu_{46}$ film (Fig. 2b). These peaks are most likely related to a primary and secondary crystallization (more details given later).

The sets of the crystallization peaks recorded at a heating rate of 10, 20, 30 and 40 °C/min for both films are shown in Fig. 3. The peaks are

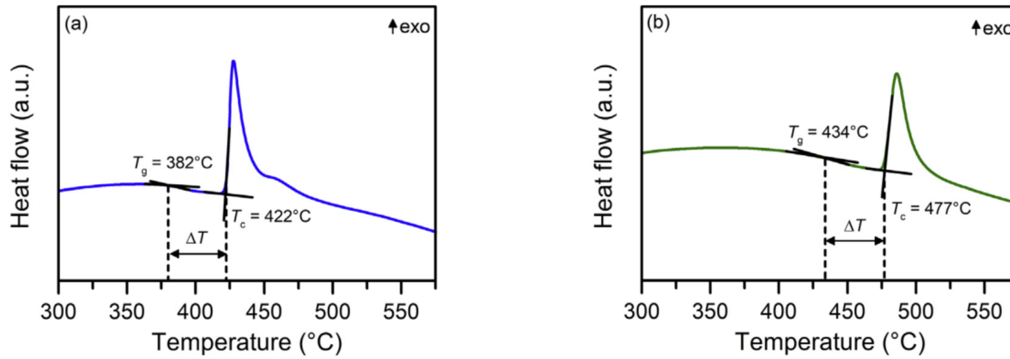

Fig. 2. DSC curves of amorphous (a) $Zr_{54}Cu_{46}$ and (b) $Zr_{27}Hf_{27}Cu_{46}$ films heated to 600 °C at a heating rate of 30 °C/min in argon. The glass transition temperature T_g, crystallization temperature T_c and supercooled liquid region ΔT are highlighted.

displayed after being processed by subtraction of baselines. One can see that the peaks shift to higher temperatures and their intensity increases with increasing heating rate. At a higher heating rate, the films remain in each particular temperature interval for a shorter period of time and therefore there is less time for their crystallization. The crystallization takes place at a higher temperature, which results in an increase in the crystallization rate and consequently in a higher peak intensity.

Since the crystallization of the $Zr_{54}Cu_{46}$ film is characterized by two overlapping peaks, the Fraser-Suzuki function [23,24] was used for their deconvolution procedure:

$$y = a_0 \exp\left[-\ln 2\left[\frac{\ln\left(1 + 2a_3\frac{x-a_1}{a_2}\right)}{a_3}\right]^2\right] \quad (1)$$

where a_0, a_1, a_2 and a_3 are the parameters giving the amplitude, position, half-width and asymmetry of the peak, respectively. Fig. 4 represents an example of this deconvolution for a heating rate of 30 °C/min. It shows the original double exothermic peak (black curve) along with a fitting peak of a higher (blue curve) and lower (orange curve) intensity and a cumulative peak corresponding to the sum of the two fitting peaks (red curve). It is seen that the cumulative peak is in very good agreement with the original one.

In order to evaluate the activation energy corresponding to the onset of the crystallization in both thin-film metallic glasses, we limited our non-isothermal kinetic analysis only to the first well-defined exothermic peak in case of the $Zr_{54}Cu_{46}$ film. After integration and subsequent normalization of the crystallization peaks, the conversion fraction α, which determines the amount of the material converted during the non-isothermal crystallization, was calculated for both films, see Fig. 5. All curves exhibit a sigmoidal shape with increasing temperature. The conversion fraction α increases rapidly from 0.05 to 0.95 in contrast to the beginning and end of the conversion. That is, the

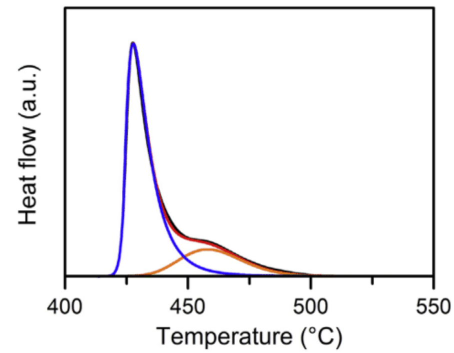

Fig. 4. Example of the deconvolution of the original double exothermic peak (black curve) of the $Zr_{54}Cu_{46}$ film heated at a heating rate of 30 °C/min. The blue and orange curves correspond to peaks fitted by using Fraser-Suzuki function and the red curve represents their sum. (For interpretation of the references to colour in this figure legend, the reader is referred to the web version of this article.)

crystallization process occurs primarily in this range. This behavior is typical in amorphous materials upon isothermal and non-isothermal heating [25].

The apparent activation energy E_a of the crystallization process under non-isothermal heating can be determined, for instance, by the Kissinger–Akahira–Sunose (KAS) method based on the following equation [26,27]:

$$\ln\left(\frac{T_\alpha^2}{\beta}\right) = \frac{E_a}{RT_\alpha} + C \quad (2)$$

where β is the heating rate, R is the universal gas constant, T_α is the absolute temperature at the given value of α and C is a constant. The

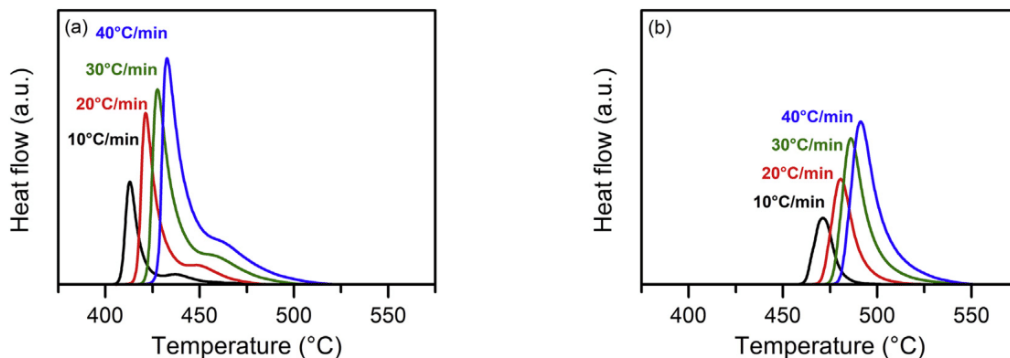

Fig. 3. Exothermic peaks of (a) $Zr_{54}Cu_{46}$ and (b) $Zr_{27}Hf_{27}Cu_{46}$ films recorded at four different heating rates (10, 20, 30 and 40 °C/min) in argon.

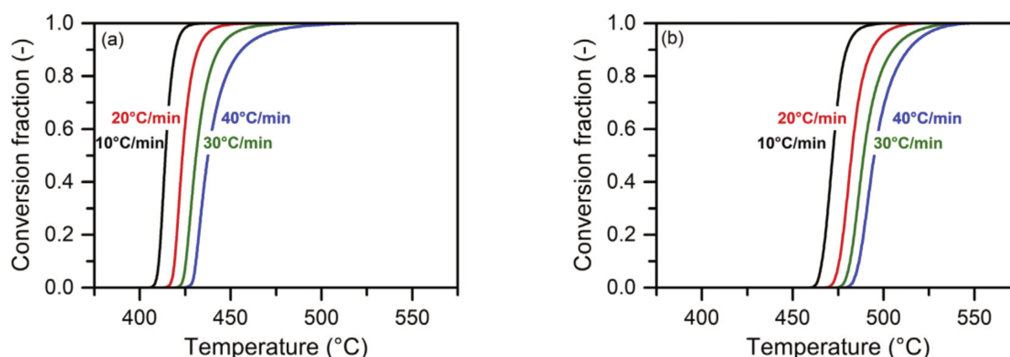

Fig. 5. Conversion fractions α for (a) $Zr_{54}Cu_{46}$ and (b) $Zr_{27}Hf_{27}Cu_{46}$ films corresponding to four different heating rates (10, 20, 30 and 40 °C/min).

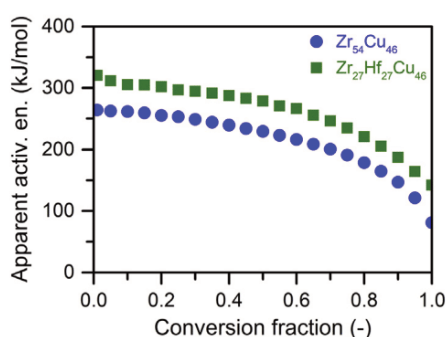

Fig. 6. Apparent activation energies as a functions of the conversion fraction for $Zr_{54}Cu_{46}$ (blue circles) and $Zr_{27}Hf_{27}Cu_{46}$ (green squares) films. (For interpretation of the references to colour in this figure legend, the reader is referred to the web version of this article.)

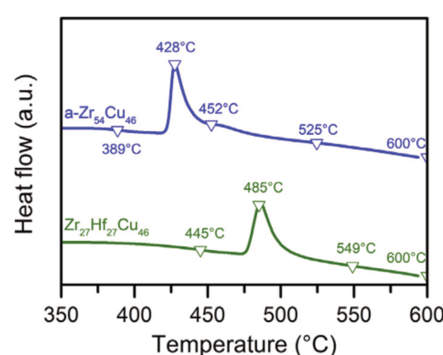

Fig. 7. DSC curves of $Zr_{54}Cu_{46}$ (upper curve) and $Zr_{27}Hf_{27}Cu_{46}$ (lower curve) films with highlighted temperatures corresponding to XRD patterns shown in Fig. 8.

plot of $\ln(T_\alpha^2/\beta)$ versus $1/T_\alpha$ provides a straight line and from the slope of this line the activation energy of the crystallization can be calculated. The obtained values of the apparent activation energy as a function of the conversion fraction α are plotted in Fig. 6. It can be seen that the apparent activation energy of both films decreases as the conversion fraction increases. The highest apparent activation energy at the early stage of the process suggests that there is a high-energy barrier which needs to be overcome to start the crystallization process. It may be related to the nucleation of crystalline phase(s). Its value (an intercept with the y-axis) is 264 and 320 kJ/mol for the $Zr_{54}Cu_{46}$ and $Zr_{27}Hf_{27}Cu_{46}$ film, respectively. The subsequent decrease of the apparent activation energy is caused by the fact that the nucleation requires higher energy than grain growth [7,28]. The value of the apparent activation energy for $\alpha = 0.5$ is 230 and 279 kJ/mol for the $Zr_{54}Cu_{46}$ and $Zr_{27}Hf_{27}Cu_{46}$ film, respectively. As clearly seen from Fig. 6, the apparent activation energy is higher in case of the $Zr_{27}Hf_{27}Cu_{46}$ film compared to the $Zr_{54}Cu_{46}$ film for all conversion fractions. This indicates that the amorphous structure of the $Zr_{27}Hf_{27}Cu_{46}$ film is more resistant to the crystallization.

For better understanding of the crystallization process, the $Zr_{54}Cu_{46}$ and the $Zr_{27}Hf_{27}Cu_{46}$ film fragments were heated to selected characteristic temperatures, which are highlighted on the DSC curves shown in Fig. 7. XRD patterns of the powdered film fragments after their heating to these selected temperatures are shown in Fig. 8. As can be seen, the heating of both films to the beginning of the supercooled liquid region (389 °C for the $Zr_{54}Cu_{46}$ film and 445 °C for the $Zr_{27}Hf_{27}Cu_{46}$ film) preserves their amorphous structure, compare Figs. 1 and 8. Upon the heating to the temperature corresponding to the peak maxima (428 °C for the $Zr_{54}Cu_{46}$ film and 485 °C for the $Zr_{27}Hf_{27}Cu_{46}$ film), the amorphous structure of the films is converting to the crystalline one. In case of the $Zr_{54}Cu_{46}$ film, all diffraction peaks can be assigned to the tetragonal $CuZr_2$ (PDF Card No. 00-018-0466) phase. In case of the $Zr_{27}Hf_{27}Cu_{46}$ film, diffraction peaks lie just in the middle of the positions corresponding to the tetragonal $CuZr_2$ and $CuHf_2$ (PDF Card No. 04-004-2396) phases, and the orthorhombic $Cu_{10}Zr_7$ (PDF Card No. 00-047-1028) and $Cu_{10}Hf_7$ (PDF Card No. 01-082-6313) phases. That means, a double-phase solid-solution structure is crystallizing in this film consisting of the tetragonal $Cu(Hf,Zr)_2$ and orthorhombic $Cu_{10}(Hf,Zr)_7$ phases. More details about the substitution of Hf for Zr in the structure of Zr-Hf-Cu films have been reported in our previous paper [22].

As can be seen from the XRD patterns in Fig. 8b, a further increase of the heating temperature up to 600 °C does not cause any other changes in the structure of the $Zr_{27}Hf_{27}Cu_{46}$ film. This behavior is significantly different from that of the $Zr_{54}Cu_{46}$ film, see Fig. 8a. A further increase of the temperature in this film beyond the first exothermic peak leads to the appearance of other low-intensity diffraction peaks. The intensity of these diffraction peaks gradually increases at least up to 525 °C (beyond the second low-intensity exothermic peak) and these peaks correspond to the orthorhombic $Cu_{10}Zr_7$ phase. In summary, the crystallization of the $CuZr_2$ and $Cu_{10}Zr_7$ phases from the amorphous state of the binary $Zr_{54}Cu_{46}$ thin-film metallic glass takes place in two successive steps in contrast to the ternary $Zr_{27}Hf_{27}Cu_{46}$ thin-film metallic glass, in which the $Cu(Hf,Zr)_2$ and $Cu_{10}(Hf,Zr)_7$ phases crystallize from the amorphous state simultaneously.

3.3. *Isothermal oxidation behavior*

The oxidation behavior of the amorphous $Zr_{54}Cu_{46}$ and $Zr_{27}Hf_{27}Cu_{46}$ thin-film metallic glasses and the crystalline $Zr_{54}Cu_{46}$ thin-film alloy was investigated by high-resolution thermogravimetry upon a dynamical and isothermal heating.

Dynamical thermogravimetric oxidation curves measured from room temperature up to 800 °C in synthetic air at a heating rate of

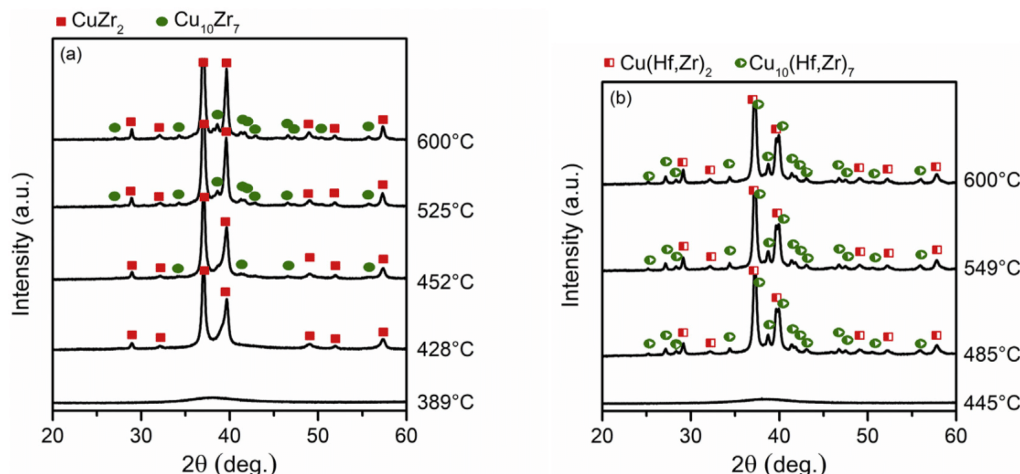

Fig. 8. XRD patterns of (a) $Zr_{54}Cu_{46}$ and (b) $Zr_{27}Hf_{27}Cu_{46}$ powdered films after their heating to the temperatures highlighted in Fig. 7.

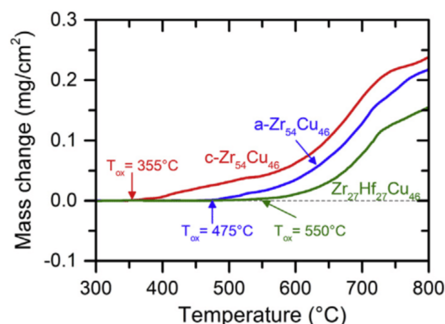

Fig. 9. Dynamical thermogravimetric oxidation curves of crystalline c-$Zr_{54}Cu_{46}$ and amorphous a-$Zr_{54}Cu_{46}$, and amorphous $Zr_{27}Hf_{27}Cu_{46}$ films recorded at a heating rate of 10 °C/min in air.

10 °C/min are presented in Fig. 9. It can be seen that the onset of the oxidation of the $Zr_{54}Cu_{46}$ film, defining the oxidation temperature T_{ox}, is dependent on its structure. Moreover, the change of the elemental composition, i.e. the substitution of Hf for Zr, also strongly affects the onset of the oxidation. The crystalline $Zr_{54}Cu_{46}$ film starts to oxidize at about 355 °C while the amorphous $Zr_{54}Cu_{46}$ and $Zr_{27}Hf_{27}Cu_{46}$ films at about 475 °C and 550 °C, respectively. That is, T_{ox} of the thin-film metallic glasses is distinctly shifted to higher temperatures (by about 120 °C for the $Zr_{54}Cu_{46}$ film and by about 195 °C for the $Zr_{27}Hf_{27}Cu_{46}$ film). Above T_{ox}, the mass gain follows a very similar trend for all three films, see Fig. 9. This can be ascribed to the fact that all films are already crystalline at these temperatures and the mechanism of the oxidation is very similar. The lowest mass gain (0.15 mg/cm^2) at a final temperature of 800 °C is measured for the $Zr_{27}Hf_{27}Cu_{46}$ film.

Isothermal thermogravimetric oxidation curves of all three films measured at various temperatures ranging from 400 to 575 °C for 3 h in synthetic air are shown in Fig. 10. Because the thermogravimetric signal at the beginning of each isothermal measurement was affected by oscillations of the temperature signal due to the transition from the dynamical ramp heating to the isothermal steady-state annealing, corresponding thermogravimetric data are not shown for the first 14 min. The films were heated up to each temperature as fast as possible (50 °C/min) to reduce their initial oxidation before starting the isothermal annealing. When the initial mass change was not zero, it was added to each isothermal curve.

Fig. 10 shows that the structure and the elemental composition of the studied films has a significant effect on their isothermal oxidation behavior. All oxidation curves in the temperature range from 400 to 575 °C obey the parabolic law, i.e. the oxidation proceeds with a continuously reducing oxidation rate. The rate is then inversely proportional to the mass of the oxide grown:

$$\frac{dm}{dt} = \frac{k}{m} \quad (3)$$

where m is the mass of the oxide, t is the time and k denotes the oxidation rate constant.

This oxidation behavior indicates that a dense barrier oxide layer forms on the surface of the films and the oxidation through this layer is a diffusion-controlled process [29].

It is evident that the $Zr_{27}Hf_{27}Cu_{46}$ film exhibits the lowest mass change upon the isothermal annealing at any temperature investigated. A higher oxidation rate was observed in case of the amorphous $Zr_{54}Cu_{46}$ film and even higher was observed for the crystalline $Zr_{54}Cu_{46}$ film. The highest oxidation rate for the crystalline $Zr_{54}Cu_{46}$ film may be explained by the existence of grain boundaries in this film. These boundaries serve as channels for the interdiffusion of species resulting in a rapid oxidation of the film. On the other hand, the absence of grain boundaries in the amorphous thin-film metallic glasses limits their oxidation. In addition, the substitution of Hf for Zr enhances the oxidation resistance of the film more and slows down the oxidation process upon both isothermal and dynamical heating. This indicates that the oxide layer, which grows on the surface of the $Zr_{27}Hf_{27}Cu_{46}$ film, is a more effective barrier against the diffusion of species through this layer than in the case of the $Zr_{54}Cu_{46}$ film. XRD measurements (not shown here) unraveled that the oxide surface layer contains monoclinic HfO_2. This phase is most likely responsible for the better oxidation resistance of the $Zr_{27}Hf_{27}Cu_{46}$ film compared to the $Zr_{54}Cu_{46}$ film that contains only monoclinic ZrO_2. This is in agreement with the results obtained by Opila et al. on diboride-based ceramics [30]. They observed a higher oxidation resistance HfB_2-based ceramics than those based on ZrB_2. A first-principle study of Zheng et al. on native point defects in HfO_2 and ZrO_2 also supports our results. They found out that HfO_2 is less prone to the formation of oxygen point defects than ZrO_2 and thus is more defect-free [31]. Moreover, the unit cell volume of HfO_2 (138.28 A^3 [PDF Card No. 00-034-0104]) is smaller than that of ZrO_2 (140.70 A^3 [PDF Card No. 00-037-1484]).

The thicknesses of surface oxide layers of selected films measured after their isothermal annealing by spectroscopic ellipsometry are depicted in Fig. 11. As can be seen, the lowest oxide-layer thicknesses are achieved for the $Zr_{27}Hf_{27}Cu_{46}$ film for all temperatures. On the other hand, the highest thicknesses are measured for the crystalline $Zr_{54}Cu_{46}$ film. These results corroborate very well the thermogravimetric data described above. Note that the 70 nm thickness of the oxide layer grown

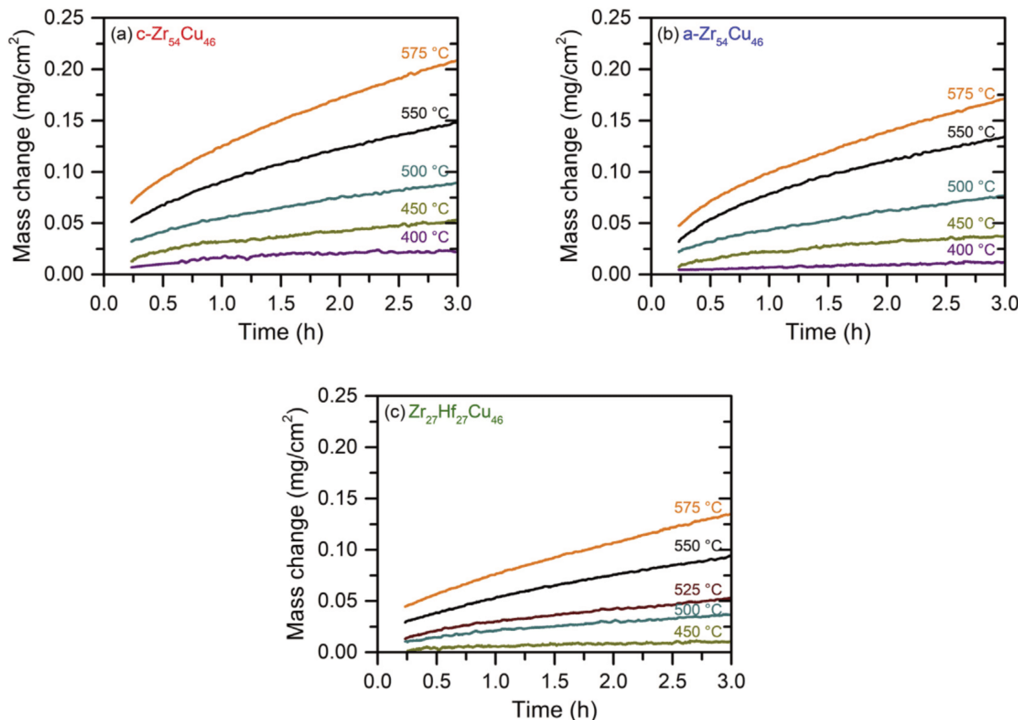

Fig. 10. Isothermal thermogravimetric oxidation of crystalline c-$Zr_{54}Cu_{46}$ and amorphous a-$Zr_{54}Cu_{46}$, and amorphous $Zr_{27}Hf_{27}Cu_{46}$ films recorded at temperatures ranging from 400 to 575 °C for 3 h in air.

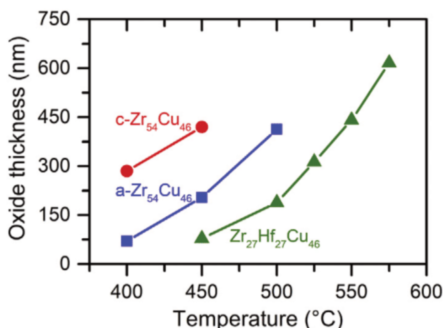

Fig. 11. Thicknesses of a surface oxide layer of crystalline c-$Zr_{54}Cu_{46}$ (circles) and amorphous a-$Zr_{54}Cu_{46}$ (squares), and amorphous $Zr_{27}Hf_{27}Cu_{46}$ (triangles) films after the isothermal annealing for 3 h in air.

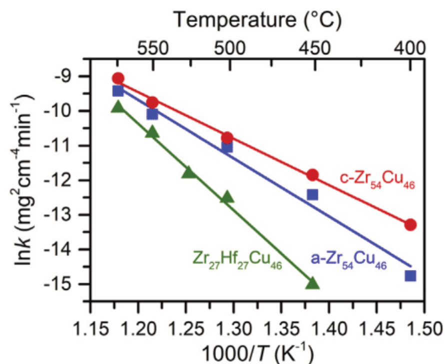

Fig. 12. Arrhenius plots of parabolic oxidation rate constants for crystalline c-$Zr_{54}Cu_{46}$ (circles) and amorphous a-$Zr_{54}Cu_{46}$ (squares), and amorphous $Zr_{27}Hf_{27}Cu_{46}$ (triangles) films.

on the $Zr_{27}Hf_{27}Cu_{46}$ film upon annealing at 450 °C is the same as that of the amorphous $Zr_{54}Cu_{46}$ film annealed at 400 °C.

The activation energy E of the oxidation process upon the isothermal annealing in the temperature range from 400 to 575 °C can be determined by taking the logarithm of the Arrhenius equation [32] for the temperature dependence of the parabolic oxidation rate constant k,

$$\ln k = \ln k_0 - \frac{E}{RT} \quad (4)$$

where k_0 is the value of the pre-exponential factor, R is the universal gas constant and T is the absolute temperature. The plot of ln$k$ as a function of the reciprocal temperature 1/T (Fig. 12) provides a straight line and the slope of this line is equal to $-E/R$. The obtained value of E is 111.5 kJ/mol for the crystalline $Zr_{54}Cu_{46}$ film, 142.5 kJ/mol for the amorphous $Zr_{54}Cu_{46}$ film and 208 kJ/mol for the $Zr_{27}Hf_{27}Cu_{46}$ film in the temperature range investigated. It should be mentioned that the activation energy E is the minimum energy needed to realize the oxidation via the diffusion of species and its value is inversely proportional to the diameter of the diffusion channel. Therefore, the highest activation energy corresponds to the $Zr_{27}Hf_{27}Cu_{46}$ film with the highest oxidation resistance. Its dense surface oxide layer serves as the most efficient diffusion barrier compared to those grown on the $Zr_{54}Cu_{46}$ films.

4. Conclusions

The crystallization and oxidation behavior of binary $Zr_{54}Cu_{46}$ and ternary $Zr_{27}Hf_{27}Cu_{46}$ thin-film metallic glasses were systematically investigated by differential scanning calorimetry and high-resolution thermogravimetry, respectively, and the oxidation behavior was compared with that of a crystalline $Zr_{54}Cu_{46}$ thin-film alloy. The main results can be summarized as follows:

- The crystallization of the $Zr_{54}Cu_{46}$ film takes place at a lower temperature and in two successive steps in contrast to the $Zr_{27}Hf_{27}Cu_{46}$

film. The apparent activation energy E_a of the primary crystallization determined by non-isothermal kinetics using the Kissinger–Akahira–Sunose method is higher in the case of the $Zr_{27}Hf_{27}Cu_{46}$ film for all conversion fractions α compared to the $Zr_{54}Cu_{46}$ film (e.g. E_a = 279 kJ/mol vs. 230 kJ/mol for α = 0.5). This suggests that the crystallization process of the $Zr_{27}Hf_{27}Cu_{46}$ film is more difficult and the film is more thermally stable than the $Zr_{54}Cu_{46}$ film.

- The onset of the oxidation of the crystalline $Zr_{54}Cu_{46}$ alloy, and the amorphous $Zr_{54}Cu_{46}$ and $Zr_{27}Hf_{27}Cu_{46}$ metallic glasses is 355 °C, 475 °C and 550 °C, respectively, upon the dynamical heating. The poorest oxidation resistance in the case of the crystalline $Zr_{54}Cu_{46}$ film is caused by the presence of grain boundaries that serve as channels for fast interdiffusion of species. Since an amorphous structure is free of grain boundaries, the metallic glasses exhibit an enhanced oxidation resistance. Moreover, the substitution of Hf for Zr further improves the oxidation resistance because of the formation of more protective oxide surface layer.
- The oxidation behavior upon the isothermal annealing is governed by diffusion-controlled kinetics in the temperature range from 400 to 575 °C. The activation energy of the oxidation process determined from the Arrhenius equation for the parabolic oxidation rate constants is 112, 143 and 208 kJ/mol for the crystalline $Zr_{54}Cu_{46}$ film, and the amorphous $Zr_{54}Cu_{46}$ and $Zr_{27}Hf_{27}Cu_{46}$ films, respectively. These results confirm that the most protective oxide layer is formed on the surface of the $Zr_{27}Hf_{27}Cu_{46}$ film.

Acknowledgments

The authors thank Dr. Jiří Houška for ellipsometry measurements, Dr. Šimon Kos for a helpful discussion and Radomír Čerstvý for the XRD measurements. This work was supported by the Czech Science Foundation under Project No. GA16-18183S.

References

[1] J. Schroers, G. Kumar, T.M. Hodges, S. Chan, T.R. Kyriakides, Bulk metallic glasses for biomedical applications, JOM 61 (2009) 21–29, https://doi.org/10.1007/s11837-009-0128-1.
[2] A.L. Greer, Metallic glasses…on the threshold, Mater. Today 12 (2009) 14–22, https://doi.org/10.1016/S1369-7021(09)70037-9.
[3] M.F. Ashby, A.L. Greer, Metallic glasses as structural materials, Scr. Mater. 54 (2006) 321–326, https://doi.org/10.1016/J.SCRIPTAMAT.2005.09.051.
[4] J.P. Chu, J.C. Huang, J.S.C. Jang, Y.C. Wang, P.K. Liaw, Thin film metallic glasses: preparations, properties, and applications, JOM 62 (2010) 19–24, https://doi.org/10.1007/s11837-010-0053-3.
[5] J.P. Chu, J.S.C. Jang, J.C. Huang, H.S. Chou, Y. Yang, J.C. Ye, Y.C. Wang, J.W. Lee, F.X. Liu, P.K. Liaw, Y.C. Chen, C.M. Lee, C.L. Li, C. Rullyani, Thin film metallic glasses: unique properties and potential applications, Thin Solid Films 520 (2012) 5097–5122, https://doi.org/10.1016/J.TSF.2012.03.092.
[6] M. Apreutesei, P. Steyer, L. Joly-Pottuz, A. Billard, J. Qiao, S. Cardinal, F. Sanchette, J.M. Pelletier, C. Esnouf, Microstructural, thermal and mechanical behavior of co-sputtered binary Zr–Cu thin film metallic glasses, Thin Solid Films 561 (2014) 53–59, https://doi.org/10.1016/j.tsf.2013.05.177.
[7] O. Lozada-Flores, I.A. Figueroa, G. Gonzalez, A.E. Salas-Reyes, Influence of minor additions of Si on the crystallization kinetics of Cu55Hf45 metallic glasses, Thermochim. Acta 662 (2018) 116–125, https://doi.org/10.1016/J.TCA.2018.02.006.
[8] M. Paljević, M. Tudja, Unusual oxidation behaviour of Zr50Cu50 alloy at high temperatures, Corros. Sci. 50 (2008) 818–822, https://doi.org/10.1016/J.CORSCI.2007.11.003.
[9] K. Weller, Z.M. Wang, L.P.H. Jeurgens, E.J. Mittemeijer, Oxidation kinetics of amorphous AlxZr1 – x alloys, Acta Mater. 103 (2016) 311–321, https://doi.org/10.1016/J.ACTAMAT.2015.09.039.
[10] W. Kai, Y.R. Chen, T.H. Ho, H.H. Hsieh, D.C. Qiao, F. Jiang, G. Fan, P.K. Liaw, Air oxidation of a Zr58Cu22Al12Fe8 bulk metallic glass at 350-550 degrees C, J. Alloys Compd. 483 (2009) 519–525.
[11] U. Köster, L. Jastrow, M. Meuris, Oxidation of Cu60Zr30Ti10 metallic glasses, Mater. Sci. Eng. A 449–451 (2007) 165–168, https://doi.org/10.1016/J.MSEA.2006.02.291.
[12] Z. Xu, Y. Xu, A. Zhang, J. Wang, Z. Wang, Oxidation of amorphous alloys, J. Mater. Sci. Technol. 34 (2018) 1977–2005, https://doi.org/10.1016/J.JMST.2018.02.015.
[13] I. Kalay, M.J. Kramer, R.E. Napolitano, Crystallization kinetics and phase transformation mechanisms in Cu56Zr44 glassy alloy, Metall. Mater. Trans. A 46 (2015) 3356–3364, https://doi.org/10.1007/s11661-015-2921-5.
[14] T. Cullinan, I. Kalay, Y.E. Kalay, M. Kramer, R. Napolitano, Kinetics and mechanisms of isothermal devitrification in amorphous Cu50Zr50, Metall. Mater. Trans. A Phys. Metall. Mater. Sci. 46 (2015) 600–613, https://doi.org/10.1007/s11661-014-2661-y.
[15] Q. Gao, Z. Jian, J. Xu, M. Zhu, F. Chang, A. Han, Crystallization kinetics of the Cu50Zr50 metallic glass under isothermal conditions, J. Solid State Chem. 244 (2016) 116–119, https://doi.org/10.1016/j.jssc.2016.09.023.
[16] R. Rashidi, M. Malekan, R. Gholamipour, Crystallization kinetics of Cu47Zr47Al6 and (Cu47Zr47Al6)99Sn1 bulk metallic glasses, J. Non-Cryst. Solids 498 (2018) 272–280, https://doi.org/10.1016/J.JNONCRYSOL.2018.06.042.
[17] C. Peng, Z.H. Chen, X.Y. Zhao, A.L. Zhang, L.K. Zhang, D. Chen, Crystallization kinetics of Zr60Cu25Fe5Al10 bulk metallic glass, J. Non-Cryst. Solids 405 (2014) 7–11, https://doi.org/10.1016/J.JNONCRYSOL.2014.08.030.
[18] M. Mohammadi Rahvard, M. Tamizifar, S.M.A. Boutorabi, The effect of Ag addition on the non-isothermal crystallization kinetics and fragility of Zr56Co28Al16 bulk metallic glass, J. Non-Cryst. Solids 481 (2018) 74–84, https://doi.org/10.1016/J.JNONCRYSOL.2017.10.026.
[19] L. Bing, L. Yanhong, Y. Ke, L. Jinshan, F. Xinhui, Effect of yttrium addition on the non-isothermal crystallization kinetics and fragility of Cu-Zr-Al bulk metallic glass, Thermochim. Acta 642 (2016) 105–110, https://doi.org/10.1016/j.tca.2016.08.001.
[20] R. Fernández, W. Carrasco, A. Zúñiga, Structure and crystallization of amorphous Cu–Zr–Al powders, J. Non-Cryst. Solids 356 (2010) 1665–1669, https://doi.org/10.1016/J.JNONCRYSOL.2010.06.016.
[21] P. Zeman, M. Zítek, S. Zuzjaková, R. Čerstvý, Amorphous Zr-Cu thin-film alloys with metallic glass behavior, J. Alloys Compd. (2017), https://doi.org/10.1016/j.jallcom.2016.12.098.
[22] M. Zítek, P. Zeman, Š. Zuzjaková, M. Kotrlová, R. Čerstvý, Tuning properties and behavior of magnetron sputtered Zr-Hf-Cu metallic glasses, J. Alloys Compd. 739 (2018) 848–855, https://doi.org/10.1016/J.JALLCOM.2017.12.301.
[23] A. Perejón, P.E. Sánchez-Jiménez, J.M. Criado, L.A. Pérez-Maqueda, Kinetic analysis of complex solid-state reactions. a new deconvolution procedure, J. Phys. Chem. B 115 (2011) 1780–1791, https://doi.org/10.1021/jp110895z.
[24] R. Svoboda, J. Málek, Applicability of Fraser-Suzuki function in kinetic analysis of complex crystallization processes, J. Therm. Anal. Calorim. 111 (2013) 1045–1056, https://doi.org/10.1007/s10973-012-2445-9.
[25] O. Lozada-Flores, I.A. Figueroa, G.A. Lara, G. Gonzalez, C. Borja-Soto, J.A. Verduzco, Crystallization kinetics of Cu55Hf45 glassy alloy, J. Non-Cryst. Solids 460 (2017) 1–5, https://doi.org/10.1016/j.jnoncrysol.2017.01.021.
[26] H.E. Kissinger, Reaction kinetics in differential thermal analysis, Anal. Chem. 29 (1957) 1702–1706, https://doi.org/10.1021/ac60131a045.
[27] T. Akahira, T. Sunose, Method of determinig activation deterrioration constant of electrical insulating materials, Res. Rep. Chiba. Inst. Technol. (Sci Technol). 16 (1971) 22–23.
[28] Y.H. Li, C. Yang, L.M. Kang, H.D. Zhao, S.G. Qu, X.Q. Li, W.W. Zhang, Y.Y. Li, Non-isothermal and isothermal crystallization kinetics and their effect on microstructure of sintered and crystallized TiNbZrTaSi bulk alloys, J. Non-Cryst. Solids 432 ((2016) 440–452, https://doi.org/10.1016/J.JNONCRYSOL.2015.11.005.
[29] S. Bose, High Temperature Coatings, 1st ed., Elsevier Inc, 2007, https://doi.org/10.1016/B978-075068252-7/50008-1.
[30] E. Opila, E. Opila, S. Levine, S. Levine, J. Lorincz, Oxidation of ZrB 2 - and HfB 2 -based ultra-high temperature ceramics: effect of Ta additions, J. Mater. Sci. 39 (2004) 5969–5977, https://doi.org/10.1023/B:JMSC.0000041693.32531.d1.
[31] J.X. Zheng, G. Ceder, T. Maxisch, W.K. Chim, W.K. Choi, First-principles study of native point defects in hafnia and zirconia, Phys. Rev. B 75 (2007) 104112, , https://doi.org/10.1103/PhysRevB.75.104112.
[32] J.H. van't Hoff, Etudes de dynamique chimique, Muller, 1884.

B

Impact of Al or Si addition on properties and oxidation resistance of magnetron sputtered Zr–Hf–Al/Si–Cu metallic glasses

M. Zítek, P. Zeman, M. Kotrlová, R. Čerstvý

Journal of Alloys and Compounds 772 (2019) 409–417

Journal of Alloys and Compounds 772 (2019) 409–417

Contents lists available at ScienceDirect

Journal of Alloys and Compounds

journal homepage: http://www.elsevier.com/locate/jalcom

Impact of Al or Si addition on properties and oxidation resistance of magnetron sputtered Zr–Hf–Al/Si–Cu metallic glasses

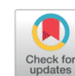

M. Zítek, P. Zeman*, M. Kotrlová, R. Čerstvý

Department of Physics and NTIS - European Centre of Excellence, University of West Bohemia, Univerzitní 8, 306 14, Plzeň, Czech Republic

ARTICLE INFO

Article history:
Received 15 July 2018
Received in revised form
4 September 2018
Accepted 7 September 2018
Available online 8 September 2018

Keywords:
Zr–Hf–Al/Si–Cu
Amorphous material
Metallic glass
Thin film
Magnetron sputtering

ABSTRACT

Amorphous quaternary Zr–Hf–Al/Si–Cu thin-film metallic alloys were prepared by non-reactive magnetron co-sputtering using four unbalanced magnetrons equipped with Zr, Hf, Al or Si, and Cu targets. The Zr, Hf and Al or Si targets were sputtered in dc regimes while the Cu target in a high-power impulse regime. Two series of films with either Al (up to 17 at.%) or Si (up to 12 at.%) addition were deposited. The effect of the elemental composition on the structure, thermal behavior, mechanical and surface properties, electrical resistivity and oxidation resistance was systematically investigated. All Zr–Hf–Al/Si–Cu films were deposited with an X-ray amorphous structure. The glass transition was, however, recognized only up to 12 at.% Al or 6 at.% Si. The addition of Al or Si enhances mechanical properties of the films and the thermal stability of their amorphous state. This may be explained by an increase of a covalent component of the mixed metallic-covalent bonds with increasing the Al and Si content. Moreover, the Zr–Hf–Al–Cu metallic glasses exhibit a wider super-cooled liquid region, while the Zr–Hf–Si–Cu metallic glasses are more oxidation resistant.

© 2018 Elsevier B.V. All rights reserved.

1. Introduction

Metallic glasses as a promising new type of materials have been widely studied during past years. It is well known that they exhibit many exceptional properties including for instance high yield strength, high elastic strain and hardness, temperature-independent electrical resistivity, excellent surface finishing, and biocompatibility [1–5]. Their unique properties originate from the disordered atomic structure without grain boundaries that contrasts with the well-defined atomic lattice arrangement in crystalline alloys [6–8].

Zr- and Cu-based metallic glasses have been extensively studied both as bulk metallic glasses (BMGs) [9–16] and as thin film metallic glasses (TFMGs) [17–24]. In recent years, several investigations have confirmed that selecting a proper alloying element in an appropriate amount has beneficial effects on the properties of the Zr- and Cu-based metallic glasses. For instance, Choi-Yim et al. [10] reported that the addition of Si up to 2 at.% into $Cu_{47}Ti_{34}Zr_{11}Ni_8$ improves the thermal stability and expands the supercooled liquid region. A similar effect was observed also for $Zr_{47}Cu_{44}Al_{19}$ metallic glasses alloyed with Si [15]. However, it has also been reported that addition of more than approximately 2 at.% Si into the melt often leads to a rapid crystallization during the fabrication process of BMGs [11]. On the other hand, Zr–Ti–B–Si and Zr–Ti–Si–W thin-film alloys were prepared by magnetron sputtering with an amorphous structure up to 20 at.% Si [21,22]. Unfortunately, it has not been reported if these amorphous alloys exhibit the glass transition. Contrary to Si-containing BMGs, alloying with Al preserves amorphous structure to at least 10 at.% of Al [9,12–14]. An optimized addition of Al into BMGs improves thermal stability [12,14], enhances hardness [14], extends the supercooled liquid region [9,12,14] and increases the critical diameter of BMGs [16]. One may see that alloying with either Al or Si may lead in certain material systems to enhanced properties. We have recently shown that the ternary Zr–Hf–Cu thin-film metallic glasses exhibit enhanced hardness, thermal stability and oxidation resistance, and very smooth and hydrophobic surface [24]. However, the effect of an addition of either Al or Si into the Zr–Hf–Cu system has not been studied yet.

The present study is, therefore, focused on the Zr–Hf–Al/Si–Cu thin-film alloys prepared by magnetron co-sputtering, which was proved to be a suitable technique for deposition of the Zr–Cu based metallic glasses [17–20,23,24]. We utilize four independent magnetrons (each of them equipped with a different material) to

* Corresponding author.
E-mail address: zemanp@kfy.zcu.cz (P. Zeman).

https://doi.org/10.1016/j.jallcom.2018.09.069
0925-8388/© 2018 Elsevier B.V. All rights reserved.

precisely control the elemental composition of the Zr–Hf–Al/Si–Cu thin-film alloys. The main aim of this study lies in a systematic investigation of the effect of an addition of Al or Si into the Zr–Hf–Cu thin-film alloys on their properties and behavior. In particular, we focus on the correlation between elemental composition and structure, thermal behavior, mechanical and surface properties, electrical resistivity and oxidation resistance of the Zr–Hf–Al/Si–Cu thin-film alloys. Since Zr–Hf–Al/Si–Cu thin-film alloys have not been synthesized yet, we systematically investigate different properties and behavior in detail.

2. Experimental details

Quaternary Zr–Hf–Al/Si–Cu thin-film alloys were deposited by magnetron co-sputtering using an AJA International ATC 2200-V sputter system which was pumped by a turbomolecular pump (1200 l/s) backed up with a multi-stage roots pump (27 m^3/hr). The base pressure before each deposition was lower than 5×10^{-5} Pa. Depositions were carried out in argon at a pressure of 0.533 Pa (4 mTorr) using four independent unbalanced magnetrons equipped with circular, indirectly cooled targets (50.8 mm in diameter, 6.35 mm in thickness). The magnetrons with the Zr target (99.5% purity, Matsurf Technologies Inc.) and the Hf target (99.9% purity, Plasmaterials Inc.) were powered by a dual power supply (Pinnacle Plus+ 5/5 kW, Advanced Energy) working independently in two dc regimes. The magnetron with the Al target (99.99% purity, Matsurf Technologies Inc.) or the Si target (99.99% purity, Matsurf Technologies Inc.) was powered by a dc power supply (DCXS-750-4, AJA International Inc.) and the magnetron with the Cu target (99.99% purity, Matsurf Technologies Inc.) was powered by a pulsed dc power supply (TruPlasma Highpulse 4002, Hüttinger Elektronik) working in a high-power impulse regime. The average target power density in a pulse was fixed at 1000 W/cm^2. The negative voltage pulse length was set to a constant value of 200 μs and the repetition frequency was set to either 36 Hz or 46 Hz. All films were deposited onto polished and ultrasonically pre-cleaned single-crystalline Si(100), soda-lime glass and molybdenum substrates held at a floating potential without any external heating. The substrates were rotated above the targets at a speed of 40 rpm and located at a target-to-substrate distance of 150 mm.

The elemental composition of the Zr–Hf–Al/Si–Cu films was controlled by adjusting the deposition rates from the Zr, Hf, (Al,Si) and Cu targets independently, particularly by the dc target powers (Zr, Hf, and (Al,Si)) and the average target power in a period (Cu). The deposition rates were measured before each deposition using a quartz crystal deposition rate monitor (SQM-160, Inficon).

The elemental composition of the as-deposited films on the Si substrate was analyzed by a scanning electron microscope (SU-70, Hitachi) operated at a primary electron energy of 20 keV using an energy dispersive spectroscopy (UltraDry, Thermo Scientific) to quantify the Zr, Hf, Al and Cu content and wavelength dispersive spectroscopy (MagnaRay WDS, Thermo Scientific) to quantify the Si content. Bulk standards of all elements were used for the quantitative analysis. The error of the elemental analysis was established to be 1 at.%.

The thermal behavior of the films was investigated by differential scanning calorimetry (DSC). Approximately 2-μm thick films deposited onto the molybdenum thin foils (0.1 mm in thickness) were relatively easily delaminated from this kind of the substrate by its bending. Obtained freestanding film fragments (~3×3 mm^2 each) of a total mass of 5 mg were then inserted into a 100 μl alumina crucible covered with a lid. An identical uncharged crucible was used as a reference. The measurements were carried out at the same heating and cooling rate of 30 °C/min in flowing argon (1 l/h) in the temperature range from room temperature to 600 °C using a DSC system (Labsys DSC 1600, Setaram). The calorimeter was calibrated by melting of Pb, Zn and Al standards with purity of 99.998 ± 0.001%.

X-ray diffraction (XRD) measurements of the structure of the as-deposited films on the Si substrates and of the powdered film fragments after their annealing were carried out using a diffractometer (X'Pert PRO, PANalytical) with Cu K_α radiation ($\lambda_{Cu} = 0.154187$ nm) working in a slightly asymmetrical Bragg-Brentano geometry with an ω-offset of 1.5° and in the standard Bragg-Brentano geometry, respectively. The ω-offset was used to eliminate a strong reflection of the single-crystalline Si(100) substrate at 2θ angle of 69.17°. The data were collected using an ultrafast detector X'Celerator in the 2θ range of 20°–60°.

The film thickness and the curvature of the Si substrate coated with the film, from which a residual macrostress was determined using the modified Stoney's formula, were measured by a surface profilometer (Dektak 8 Stylus Profiler, Veeco). The hardness, effective Young's modulus and elastic recovery of the films on the Si substrate were evaluated from the load vs. displacement curves [25], which were measured at room temperature and in ambient environment by a nanoindenter (TI 950 Triboindenter, Hysitron) equipped with a Berkovich-type diamond tip. For each film, a number of indents were made at different loads ranging from 1 to 10 mN and the obtained data were averaged. The ratio of the penetration depth and the film thickness was below 10% in all cases.

The electrical resistivity of the films on the glass substrate was measured at room temperature by a standard four-point probe with a spacing of 1.047 mm between the tips (Cylindrical probe, Jandel). The nonconductive glass substrate was used to avoid the effect of an electrically conductive substrate on the data measured. The measurement was also not affected by a very thin surface oxide layer (few nm in thickness) formed on the films as a result of a reaction with an ambient atmosphere because the penetration depth of the probe tips was much higher (approximately 150 nm). The water contact angle of the films on the Si substrate was measured at room temperature by a drop shape analyzer (DSA30, KRÜSS) using the sessile drop method with a droplet of distilled water with volume of 2 μl. Three measurements on each film at various positions were carried out and the obtained values were averaged. A typical error of the measurement was ±1°. The arithmetic average surface roughness of the films on the Si substrate was evaluated from a selected square area of 2×2 μm^2 measured in a non-contact mode of an atomic force microscope (SmartSPM, AIST-NT) equipped with a silicon tip (nominal radius of 10 nm).

The oxidation resistance of the films was investigated by thermogravimetry (TG) using a symmetrical high resolution system (Setaram TAG 2400). The TG analysis was carried out in synthetic atmospheric air (flow rate of 1 l/h) with dynamic heating in the temperature range from room temperature up to 1000 °C and isothermal heating at 550 °C for 3 h. The heating rates were set to 10 °C/min and 50 °C/min for dynamic heating and isothermal heating, respectively. The cooling rates were set in both cases to 30 °C/min. The Si substrates were coated only on one side. After subtracting the thermogravimetric signal corresponding to oxidation of the uncoated sides, the resulting thermogravimetric curve is related to the oxidation resistance of the Zr–Hf–Al/Si–Cu film only.

The thickness of the surface oxide layer was determined by a J.A. Woollam Co. variable angle spectroscopic ellipsometer. The measurements were performed in the wavelength range from 300 to 2000 nm using angles of incidence of 65°, 70° and 75° in reflection.

3. Results and discussion

In this section, the effect of an addition of Al (up to 17 at.%) or Si

(up to 12 at.%) into the Zr–Hf–Cu thin-film alloys on their properties and behavior is investigated. Two film series, labeled as Al-series and Si-series from now on, are systematically studied. The effect of the elemental composition (Fig. 1) on the structure (Figs. 2 and 3), thermal behavior (Figs. 4–7), mechanical (Figs. 8 and 9) and surface properties (Fig. 10), electrical resistivity (Fig. 11) and oxidation behavior (Figs. 12 and 13) is presented and discussed in detail.

3.1. Elemental composition

The elemental composition of the Zr–Hf–Al/Si–Cu thin-film alloys was varied by adjusting the deposition rate from the Zr, Hf, Al or Si and Cu targets as described in Experimental details. The total deposition rate varied from 27 nm/min to 36 nm/min and the thickness of all films was around 2 μm. In both series, we started the experiments with the deposition of the ternary Zr–Hf–Cu thin film with approximately 46 at.% Cu, 27 at.% Zr and 27 at.% Hf. A subsequent addition of Al or Si was done at the expense of Zr and Hf while maintaining the ratio [Zr]:[Hf] ≈ 1 and the content of Cu at approximately 46 at.%. An evolution of the elemental composition of the films of the Si-series as a function of the applied power at the Si target is shown in Fig. 1. A similar evolution was observed also for the Al-series except that the comparable Al content was achieved for a lower applied power at the Al target. This is due to different sputtering yields of Al and Si for a comparable energy of impacting Ar ions [26]. One may notice that by setting appropriate target powers, we were able to precisely control the elemental composition in the whole studied range. The Al and Si content in the films was varied from 0 to 17 at.% and from 0 to 12 at.%, respectively.

3.2. Structure

In order to investigate the effect of the elemental composition on the structure of the as-deposited films, the XRD measurements were carried out. XRD patterns of the films of the Al-series are presented in Fig. 2. As can be seen, all films containing up to 17 at.% Al exhibit a low-intensity broad diffraction peak (hump) indicating that these films are X-ray amorphous. The full width at half maximum of this peak is around 5° 2θ. As for the Si-series, a similar set of XRD patterns were collected (not shown). It implies that these films are also X-ray amorphous in the whole range investigated, i.e. from 0 to 12 at.% Si. Such a high content of Si for the amorphous alloys based on Zr–Cu has not been reported for BMGs so far, as described in Introduction. Our results point out the key importance of using magnetron sputtering with very high cooling rates of the vapor on the substrate for the deposition of amorphous thin-film metallic alloys in a wide composition range.

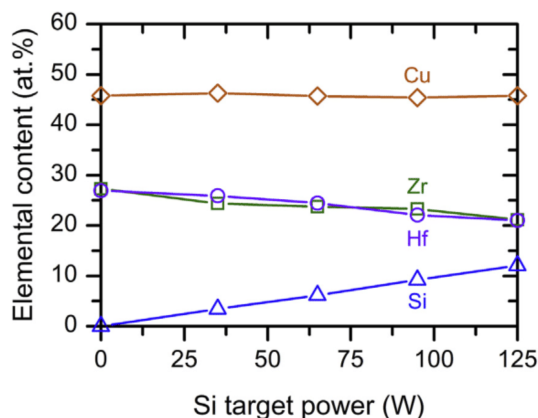

Fig. 1. Elemental composition of the films of the Si-series as a function of the applied power at the Si target.

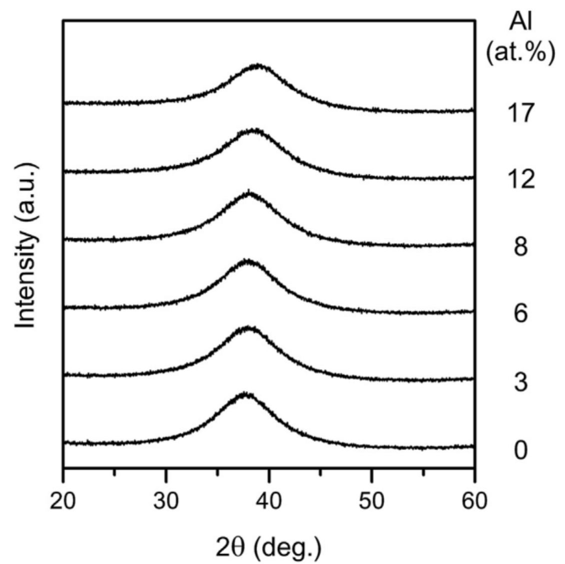

Fig. 2. XRD patterns of the as-deposited films of the Al-series.

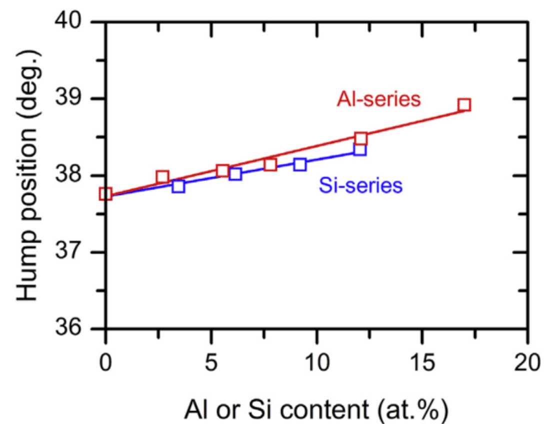

Fig. 3. Position of the broad diffraction peak (hump) of the films of the Al- and Si-series as a function of the Al or Si content.

A closer look at the XRD patterns reveals that the maximum of the broad peak shifts to higher 2θ angles with increasing Al and Si content for both film series, see Fig. 3. As mentioned before, either element (Al and Si) is added at the expense of Zr and Hf and both have a lower atomic radius than Zr and Hf. Thus, the average interatomic distance in the material decreases with their addition, which consequently leads to the shift of the hump to higher 2θ angles. As shown in Fig. 3, the shift may be very well fitted by a linear regression. Despite the fact that the radius of Al is larger than that of Si the slope of the straight line fitting the values of the Al-series is steeper indicating more rapid decrease of the interatomic distance with increasing Al content.

3.3. Thermal behavior

The effect of the elemental composition on the thermal behavior of the Zr–Hf–Al/Si–Cu films was studied using differential

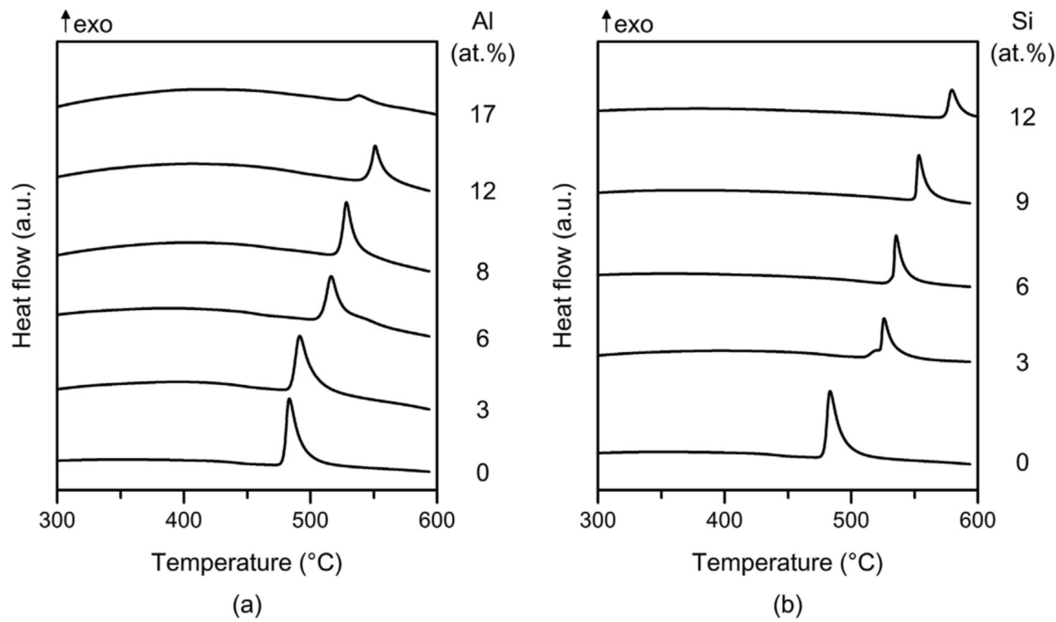

Fig. 4. DSC curves of the films of the (a) Al-series and (b) Si-series acquired at a heating rate of 30 °C/min in Ar.

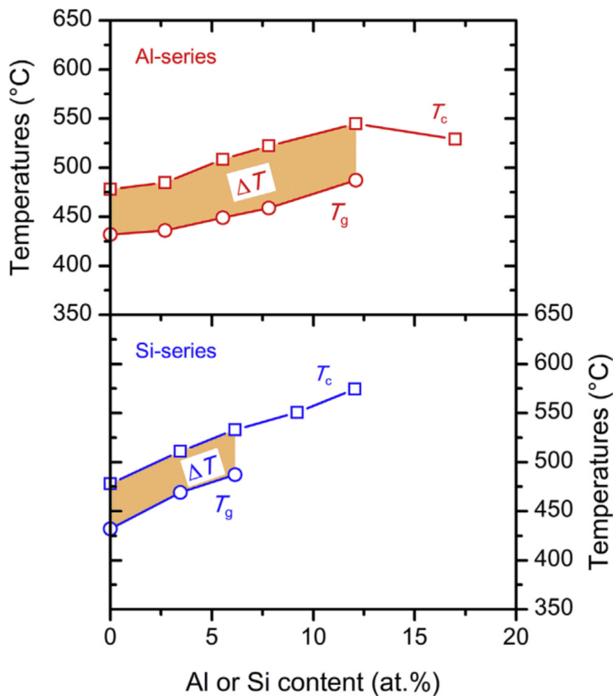

Fig. 5. Crystallization temperature T_c (open squares), glass transition temperature T_g (open circles) and the supercooled liquid region ΔT (orange area) of the films from the Al- and Si-series. (For interpretation of the references to colour in this figure legend, the reader is referred to the Web version of this article.)

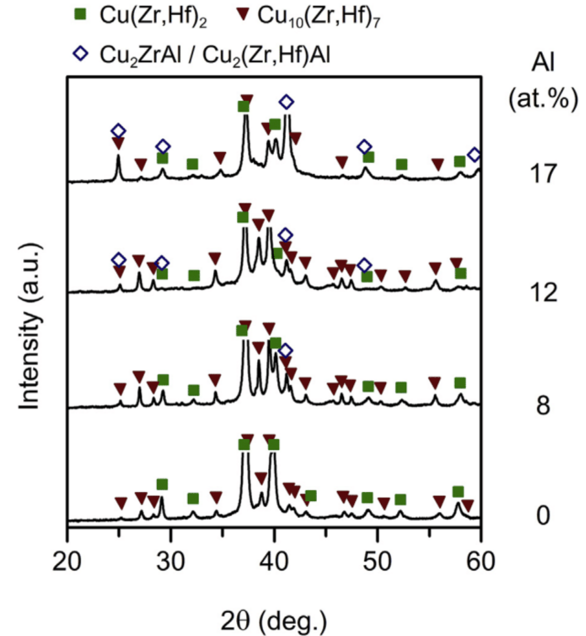

Fig. 6. Selected XRD patterns taken from powdered fragments of the films from the Al-series after their annealing up to 600 °C and cooling down back to room temperature. The main diffraction peaks of the Cu(Zr,Hf)2, Cu10(Zr,Hf)7 and Cu2ZrAl or Cu2(Zr,Hf)Al phases are marked by the symbols.

scanning calorimetry. Freestanding fragments of each film from both series were annealed up to 600 °C in Ar. Fig. 4a gathers DSC curves of the films of the Al-series. As can be seen, one well-defined exothermic peak is detected up to 12 at.% Al. This peak, related to the crystallization of the film, is shifted to higher temperatures with increasing Al content. The onset of the peak defines the crystallization temperature, T_c. The DSC curve of the film with 17 at.% Al is also characterized with one exothermic peak, which is, however, detected at a lower temperature compared to the film with 12 at.% Al and has a significantly lower intensity. A similar set of the DSC curves was also observed for the Si-series except that the film with 3 at.% Si is characterized by a low-intensity exothermic peak followed by a second high intensity exothermic peak, see Fig. 4b. It can be also seen in Fig. 4a and b that the exothermic peak

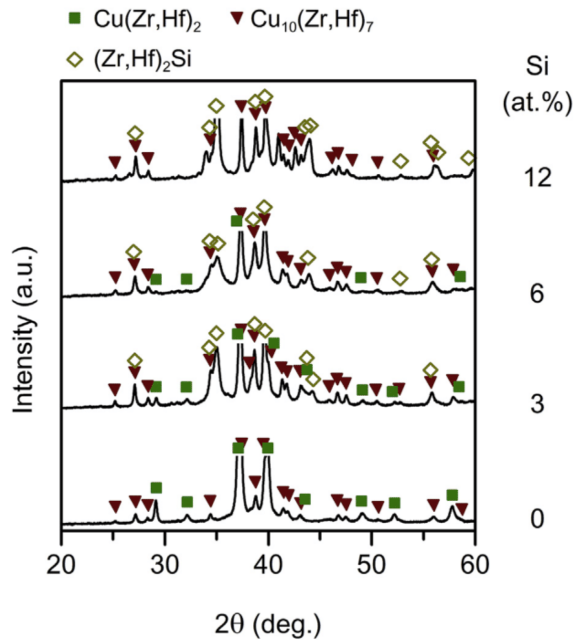

Fig. 7. Selected XRD patterns taken from powdered fragments of the films from the Si-series after their annealing up to 600 °C and cooling down back to room temperature. The main diffraction peaks of the Cu(Zr,Hf)2, Cu10(Zr,Hf)7 and (Zr,Hf)2Si phases are marked by the symbols.

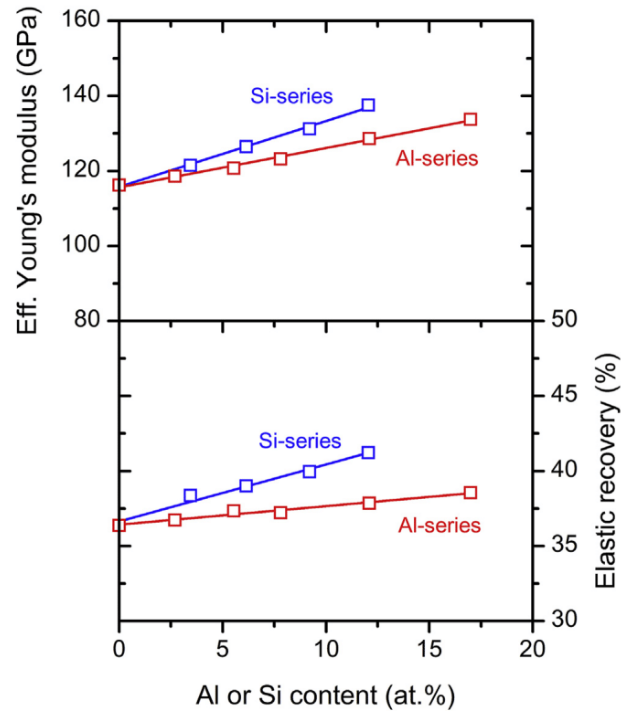

Fig. 9. Effective Young's modulus and elastic recovery of the films of the Al- and Si-series as a function of the Al or Si content.

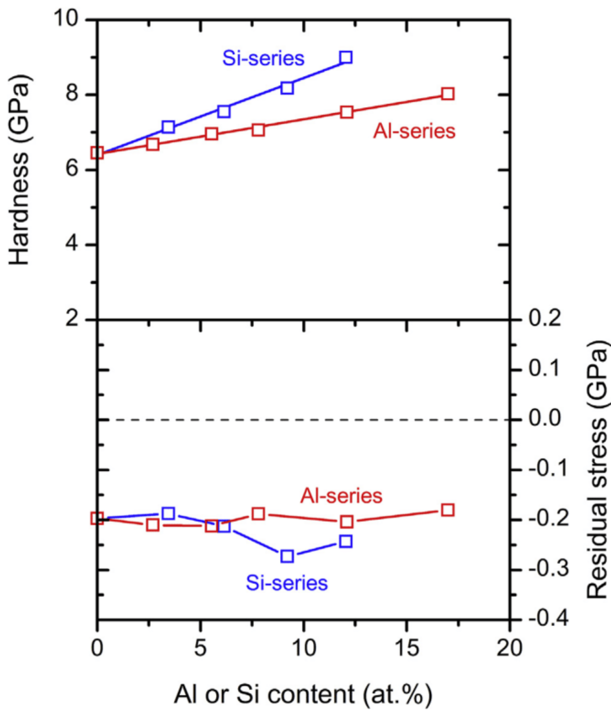

Fig. 8. Hardness and residual stress of the films of the Al- and Si-series as a function of the Al or Si content.

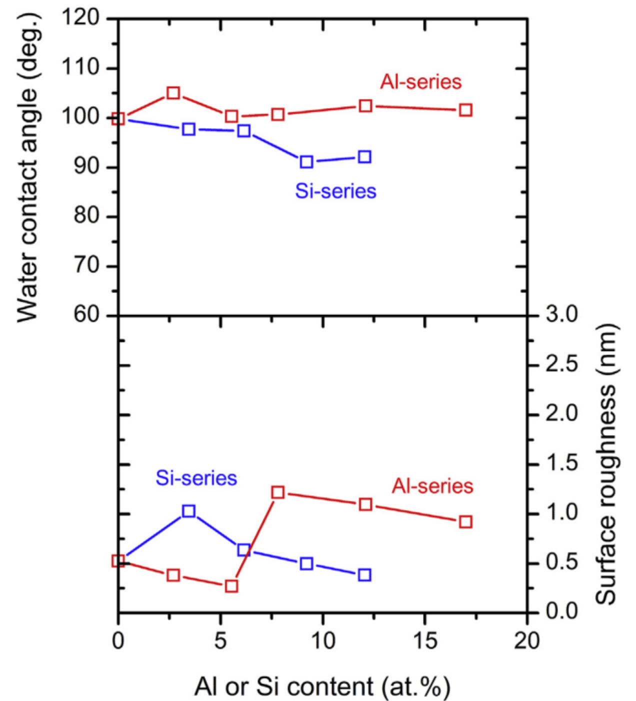

Fig. 10. Water contact angle and surface roughness of the films of the Al- and Si-series as a function of the Al or Si content.

of the films of the Si-series was located at a higher temperature for the comparable amount of Si and Al. The shift of the exothermic peak to higher temperatures with increasing either Al or Si up to 12 at.% indicates an enhanced thermal stability of the amorphous state of the quaternary Zr–Hf–Al/Si–Cu films compared to the ternary Zr–Hf–Cu films. This behavior may be attributed to more difficult diffusion of the atoms in the film upon heating due to the

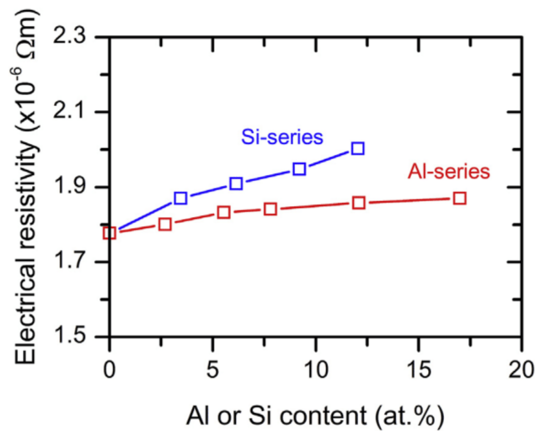

Fig. 11. Electrical resistivity of the films of Al- and Si-series as a function of the Al or Si content.

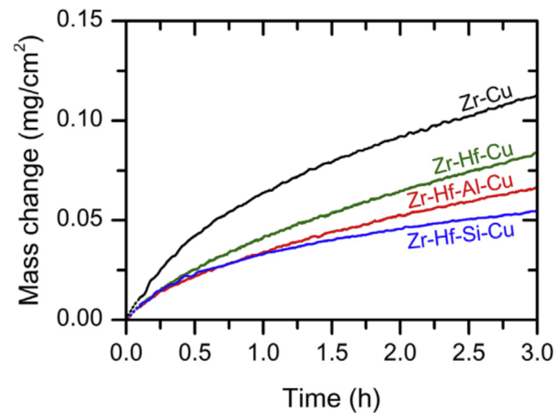

Fig. 13. Isothermal thermogravimetric oxidation curves of the Zr–Cu, Zr–Hf–Cu, Zr–Hf–Al–Cu and Zr–Hf–Si–Cu films with a constant Cu value of 46 at.%, constant ratio [Hf]:[Zr] ≈ 1 and 3 at.% of Al or Si measured at 550 °C in a synthetic air for 3 h.

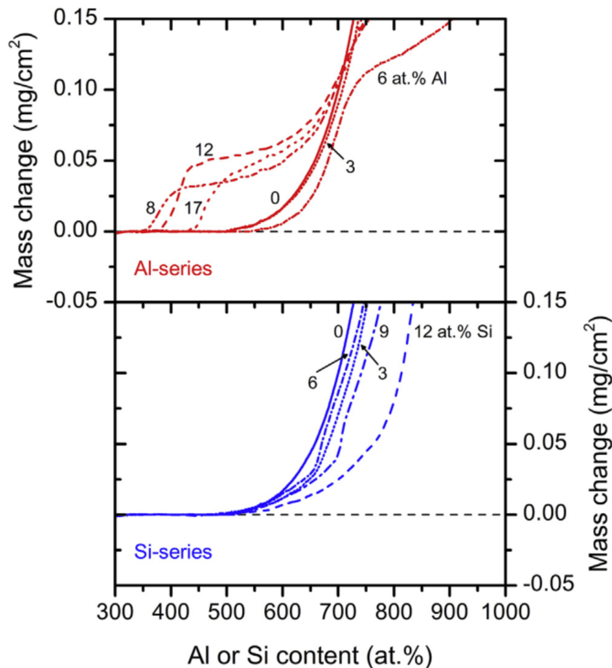

Fig. 12. Dynamical thermogravimetric oxidation curves of the films of the Al- and Si-series acquired at a heating rate of 10 °C/min in a flowing synthetic air.

presence of Al or Si with a stronger covalent bonding (more details given later).

Before the onset of the crystallization peak, we observed a decrease of a heat flow for some Zr–Hf–Al/Si–Cu films. This kind of decrease is a typical behavior of glasses and is known as a glass transition. The glass transition determines the position of the glass transition temperature, T_g (for more details see our previous paper [23]). The supercooled liquid region, ΔT, in which the glass exhibits a viscous flow and thermoplastic behavior, is located between T_g and T_c.

Fig. 5 presents the evolution of T_g and T_c for both series as a function of the Al or Si content. One may notice that we were able to recognize the glass transition only between 0 and 12 at.% Al for the films of the Al-series and between 0 and 6 at.% Si for the films of the Si-series. As can be seen in Fig. 5, the values of T_c increase monotonically up to 12 at.% of Al or Si with increasing the Al or Si content in the films. Further increase of the Al content causes a decrease of T_c. The values of T_g follow the trend of T_c. The supercooled liquid region is marked in Fig. 5 by the orange area between T_g and T_c. An addition of Al into the ternary Zr–Hf–Cu films extends the supercooled liquid region. The maximum $\Delta T = 63$ °C was achieved for the film with 8 at.% Al. On the other hand, addition of 3 at.% Si reduces the width of the supercooled region while addition of 6 at.% Si gives again the value of the ternary Zr–Hf–Cu film. The values of T_g, T_c and ΔT for the films from Al- and Si-series are summarized in Table 1. As for the addition of Al its effect in the Zr–Hf–Al–Cu films is comparable with reported results for the ternary Zr–Al–Cu metallic glasses [9,13,14]. For instance, Cheung and Shek [14] observed glass transition in the range from 0 to 10 at.% Al with a maximum value of $\Delta T = 73$ °C for 8 at.% Al. Regarding the alloying with Si, its effect is also similar with results published in the literature for the Zr-based BMG [11] except that we were able to prepare metallic glasses in a wider composition range up to 6 at.% Si but we did not observe extending of the supercooled liquid region in the investigated region.

In order to identify products of the crystallization of the films of the Al- and Si-series, XRD analysis was carried out after the DSC measurements. Prior the analysis, the film fragments were ground to powder. As expected from the DSC curves, all films crystallized upon the annealing to 600 °C. The XRD patterns of the representative films of the Al-series are shown in Fig. 6. The ternary Zr–Hf–Cu film consists of the tetragonal $Cu(Zr,Hf)_2$ and orthorhombic $Cu_{10}(Zr,Hf)_7$ solid solution phases. This is in accordance with our previous paper [24] where we showed that Hf gradually substitutes Zr with increasing Hf/(Hf+Zr) ratio. The positions of the XRD peaks are just in the middle of the positions corresponding to the tetragonal $CuZr_2$ (PDF Card No. 00-018-0466) and $CuHf_2$ (PDF Card No. 04-004-2396) phases and the orthorhombic $Cu_{10}Zr_7$ (PDF Card No. 01-078-3211) and $Cu_{10}Hf_7$ (PDF Card No. 01-082-6313) phases, which reflects well the equal content of Zr and Hf in the films. An addition of Al into the Zr–Hf–Cu films results in a quite complex structure which in turn complicates the identification of the crystallization products. In spite of this fact, some conclusions can be drawn from the XRD analysis of the patterns. An increasing Al content to 8 at.% results in the appearance of another peak at a 2θ position of about 41.25°. The position of this peak is very close to the positions of the ternary cubic Cu_2ZrAl (PDF Card No. 03-065-6362) and Cu_2HfAl (PDF Card No. 04-008-2257) phases. It cannot be, however, ruled out that it also may correspond to the cubic

Table 1
Glass transition temperature T_g, crystallization temperature T_c and supercooled liquid region $\Delta T = T_c - T_g$ of the films from the Al- and Si-series.

Al-series						
Al (at.%)	0	3	6	8	12	17
T_g (°C)	432	436	449	459	487	–
T_c (°C)	478	485	509	522	545	529
ΔT (°C)	46	49	60	63	58	–
Si-series						
Si (at.%)	0	3	6	9	12	–
T_g (°C)	432	469	487	–	–	–
T_c (°C)	478	511	533	551	574	–
ΔT (°C)	46	42	46	–	–	–

$Cu_2(Zr,Hf)Al$ solid solution phase. With further increase of the Al content, the intensity of the peak increases and also new peaks related to this cubic phase appear. Other peaks in the XRD patterns (≥8 at. % Al) can be ascribed to the tetragonal $Cu(Zr,Hf)_2$ and orthorhombic $Cu_{10}(Zr,Hf)_7$ phases but with a variable content of Zr and Hf. Some peaks are closer to the $CuZr_2$ while other to the $CuHf_2$ diffraction standards. The same is valid for the orthorhombic phase.

The XRD patterns of the representative films of the Si-series are shown in Fig. 7. The results demonstrate much higher reactivity of Si with Zr and Hf than with Cu. A small addition of Si (3 at.%) leads to the crystallization of a silicide phase. Since the positions of the XRD peaks of this phase are in between the positions of the cubic Zr_2Si (PDF Card No. 04-001-0938) and Hf_2Si (PDF Card No. 04-001-0944) diffraction standards, it implies that this phase can be considered to be the cubic $(Zr,Hf)_2Si$ solid solution. Its amount grows with increasing Si content as deduced from increasing intensity of the corresponding XRD peaks. Simultaneously, the crystallization of the tetragonal $Cu(Zr,Hf)_2$ phase is limited due to the consumption of Zr and Hf and this phase gradually vanishes. In contrast, the orthorhombic $Cu_{10}(Zr,Hf)_7$ phase is present for all Si contents investigated. Moreover, the XRD peaks of this phase remain at the same positions independently of the Si content. This is different from the effect of the Al addition.

3.4. Mechanical properties

The effect of the elemental composition on the hardness and the residual stress of the Zr–Hf–Al/Si–Cu films is shown in Fig. 8. It can be seen in the upper panel of Fig. 8 that the hardness of the films of the Al- and Si-series increases monotonically from 6.5 to 8.0 GPa and from 6.5 to 9.0 GPa, respectively. In both series the dependencies can be well fitted by straight lines. It is also clearly seen that the straight line of the Si-series is considerably steeper indicating a more pronounced effect of the Si addition on the hardness enhancement. A maximum value of the hardness of the Zr–Hf–Al/Si–Cu films, which exhibit the metallic glass behavior, is 7.5 GPa and was measured for two films containing either 12 at.% Al or 6 at.% Si. The residual stress for the films of the Al- and Si-series is shown in the bottom panel of Fig. 8. Both film series exhibit a compressive residual stress with the absolute values varying around 0.2 GPa. We have not observed a significant difference in the values of the residual stress with the addition of Al or Si. The compressive residual stress of these films can be attributed to the bombardment of the growing film by energetic Cu ions generated in the discharge in the vicinity of the Cu target sputtered in a high-power impulse regime (for more details see our previous publication [23]). A low or moderate compressive residual stress is generally beneficial in terms of increasing hardness and suppressing crack propagation.

Fig. 9 shows the evolution of the effective Young's modulus and the elastic recovery as a function of the Al or Si content in the films. It is clearly seen that the evolution of both quantities follows the trend of the hardness. The effective Young's modulus increases from 116 to 134 GPa and from 116 to 138 GPa for the Al- and Si-series, respectively. In case of the elastic recovery, the values increase from 36 to 39% and from 36 to 41% for the Al- and Si-series, respectively. The values of the effective Young's modulus as well as the values of the elastic recovery may be also fitted with straight lines with a higher slope for the Si-series. Despite the increase of the elastic recovery from 36% for the ternary Zr–Hf–Cu film, the Zr–Hf–Al/Si–Cu films still deform predominantly plastically via the formation of shear bands.

A clear correlation can be seen when comparing the evolution of T_g and T_c (see Fig. 5) and the evolution of mechanical properties (see Figs. 8 and 9) of the Zr–Hf–Al/Si–Cu metallic glasses. All aforementioned quantities increase with increasing Al or Si content in the films. This behavior may be understood in terms of an average bond energy in the films. Note that the main-group elements, Si and Al, possess p-electrons in their isolated-atom electronic configurations unlike Zr and Hf which are replaced. Thus, a case can be made that the incorporation of Al or Si into the films increases the projection of the resulting hybridized orbitals on odd p-orbitals (contrary to even s- and d-orbitals). The non-zero weight of electrons on odd p-orbitals leads to wavefunctions centered between atoms rather than on an atom, i.e. to a more directional (covalent) bonding [27].

3.5. Surface properties

The surface properties, namely the wettability and surface roughness, of the films of the Al- and Si-series are displayed in Fig. 10 as a function of the Al or Si content. The wettability of the films was characterized by the water contact angle which is shown in the upper panel of Fig. 10. As can be seen, the values of the water contact angle of the films of the Al-series scatter around 100°. On the other hand, the films from the Si-series with Si content up to 6 at.% exhibit a slightly lower water contact angle of about 97°. Further increase of the Si content leads to a more pronounced decrease of the water contact angle to the values slightly below 90°. Thus, only the films with up to 17 at.% Al or 6 at.% Si can be considered as hydrophobic.

The arithmetic average surface roughness of the films of the Al- and Si-series is shown in the bottom panel of Fig. 10. As can be seen, the low addition of Al up to 6 at.% leads to a decrease of the surface roughness from approximately 0.5 nm for the ternary Zr–Hf–Cu film to less than 0.3 nm. An increase of the Al content to 8 at.% causes a rise of the surface roughness to 1.2 nm. Further increase of the Al content leads to a moderate decrease of the surface roughness which, however, does not reach the value of the ternary Zr–Hf–Cu film. In case of the Si-series, the addition of 3 at.% Si induces an increase of the surface roughness to approximately 1 nm followed by a gradual decrease to the values lower than 0.4 nm. Despite the fact that a few films containing either Al or Si exceed the value of the surface roughness of the ternary Zr–Hf–Cu film, the Zr–Hf–Al/Si–Cu films are still very smooth, especially when compared with crystalline alloys [23].

3.6. Electrical resistivity

Fig. 11 summarizes the values of the electrical resistivity of the films of the Al- and Si-series at room temperature. As can be seen the electrical resistivity increases monotonically for both series with increasing Al or Si content. The increase is more pronounced for the films of the Si-series which correlates well with the

evolution of the mechanical properties and characteristic temperatures. Therefore, the increase can be attributed to a more covalent character of the mixed metallic-covalent bonds compared to the ternary Zr–Hf–Cu film leading to less free electrons. Despite the fact that the electrical resistivity increases with increasing Al or Si content all deposited films exhibit very low electrical resistivity lower than $2.0 \times 10^{-6}\,\Omega\,m$.

3.7. Oxidation resistance

Dynamical thermogravimetric oxidation curves of the films of the Al- and Si-series measured from room temperature up to 1000 °C in synthetic flowing air at a heating rate of 10 °C/min are shown in Fig. 12. It can be seen that the onset of the oxidation depends on the content of the additional element. All films of the Si-series, see the bottom panel of Fig. 12, start to oxidize at about 500 °C but as the temperature increases the oxidation rate decreases with increasing Si content. This may be explained by the formation of a Si-containing surface oxide layer that serves as a more efficient barrier against interdiffusion of oxygen and elements of the film.

In case of the Al-series the evolution of the oxidation resistance is more complex. We recognize two main intervals of the Al content which differ in the oxidation behavior, see the upper panel of Fig. 12. Up to 6 at.% Al, the addition of Al has positive effect on the oxidation resistance and the onset of the oxidation shifts to higher temperatures. For instance, the film containing 6 at.% Al starts to oxidize at about 550 °C. However, when the Al content is above 6 at.% Al, the onset of the oxidation of the films is registered at noticeably lower temperatures, e.g. at 350 °C for 8 at.% Al. The films start to rapidly oxidize gaining a mass change up to $0.05\,mg/cm^2$ after which the oxidation slows down. At about 550 °C, it accelerates again and the mass gain follows the trend of the films with 0 and 3 at.% Al. If one compares the onset of the crystallization (Fig. 5 and Table 1) with that of the oxidation (Fig. 12), one may notice that the Zr–Hf–Al–Cu films with the Al content between 0 and 6 at.% and the Zr–Hf–Si–Cu films with the Si content between 0 and 12 at.% exhibit very low mass gain before starting to crystallize.

Since the difference in the oxidation resistance of the Zr–Hf–Cu and Zr–Hf–Al/Si–Cu films with 3 at.% Al or Si was not so pronounced upon the dynamical heating, we carried out in addition isothermal oxidation measurements at 550 °C in a flowing synthetic air for 3 h. Fig. 13 presents the comparison of thermogravimetric curves of binary $Zr_{54}Cu_{46}$, ternary $Zr_{27}Hf_{27}Cu_{46}$, and quaternary $Zr_{25}Hf_{26}Al_3Cu_{46}$ and $Zr_{25}Hf_{26}Si_3Cu_{46}$ films. All films possess the same Cu content of 46 at.% and ternary/quaternary films a fixed ratio of [Hf]:[Zr] ≈ 1. The films were heated up to 550 °C as fast as possible (50 °C/min) to eliminate their oxidation before starting the isothermal measurements. The corresponding mass gain was therefore close to zero for all films. Because the thermogravimetric signal during the first 5 min was strongly affected by oscillations of the temperature signal due to the transition from the dynamical ramp heating to the isothermal steady-state heating, the thermogravimetric data were just extrapolated (see dashed lines) during the settling time.

As can be seen in Fig. 13, the quaternary Zr–Hf–Al/Si–Cu films containing Al or Si exhibit a lower oxidation rate and a lower mass gain after 3 h of the measurement compared to the binary Zr–Cu and ternary Zr–Hf–Cu films. The best oxidation resistance is achieved for the $Zr_{25}Hf_{26}Si_3Cu_{46}$ film. Its mass gain after 3 h is close to $0.055\,mg/cm^2$, which is approximately two times less than for the $Zr_{54}Cu_{46}$ film. This is in agreement with the measurement of the thickness of the surface oxide layer. For the $Zr_{25}Hf_{26}Si_3Cu_{46}$ film, the thickness of the oxide layer was 390 nm while for the $Zr_{54}Cu_{46}$ film was 840 nm. All oxidation curves can be well fitted with square-root functions. Oxidation in such a way indicates that a dense barrier oxide layer is formed on the surface of the films causing the reduction of the oxidation rate with time. The oxidation is then controlled by a diffusion of the species through the oxide layer [28]. From Fig. 13 it is seen that the Si-containing surface oxide layer is even more efficient than the Al-containing one. Let us also note that even if the binary $Zr_{54}Cu_{46}$ thin-film metallic glass exhibits the highest mass gain among the films investigated, it is more oxidation resistant than its crystalline counterpart of the identical composition. This will be, however, reported in detail in our separate paper along with crystallization and oxidation kinetics of the aforementioned films.

4. Conclusions

The effect of an addition of Al (up to 17 at.%) and Si (up to 12 at.%) into the Zr–Hf–Cu thin-film alloys on their properties and behavior was studied in detail. Conventional dc and high-power impulse magnetron co-sputtering of Zr, Hf, Al or Si and Cu in pure Ar was proved to be a suitable deposition technique for a reproducible deposition of quaternary Zr–Hf–Al/Si–Cu films.

The deposited thin-film metallic alloys were found to be amorphous in the whole studied range. The glass transition was, however, recognizable only up to 12 at.% Al and 6 at.% Si by differential scanning calorimetry. The increase of the Al and Si content led to an increase of the crystallization (up to 12 at.% Al and Si) and glass transition (up to 12 at.% Al and 6 at.% Si) temperature, and mechanical properties (up to 17 at.% Al and 12 at.% Si). This increase may be explained based on the increasing effect of a covalent component of the mixed metallic-covalent bonds between Al or Si and other elements of the films. Smooth, hydrophobic and electrically conductive Zr–Hf–Al/Si–Cu thin-film metallic glasses exhibit enhanced hardness, thermal stability and oxidation resistance. A wider super-cooled liquid region was obtained for the Zr–Hf–Al–Cu metallic glasses, while a better oxidation resistance for the Zr–Hf–Si–Cu metallic glasses.

Acknowledgments

The authors thank Dr. Jiří Houška, Dr. Šimon Kos and Dr. Stanislav Haviar for helpful discussions. This work was supported by the Czech Science Foundation under Project No. GA16-18183S.

References

[1] M. Telford, The case for bulk metallic glass, Mater. Today 7 (2004) 36–43, https://doi.org/10.1016/S1369-7021(04)00124-5.
[2] M.F. Ashby, A.L. Greer, Metallic glasses as structural materials, Scr. Mater. 54 (2006) 321–326, https://doi.org/10.1016/j.scriptamat.2005.09.051.
[3] A.L. Greer, Metallic glasses…on the threshold, Mater. Today 12 (2009) 14–22, https://doi.org/10.1016/S1369-7021(09)70037-9.
[4] J. Schroers, G. Kumar, T.M. Hodges, S. Chan, T.R. Kyriakides, Bulk metallic glasses for biomedical applications, JOM 61 (2009) 21–29, https://doi.org/10.1007/s11837-009-0128-1.
[5] J.P. Chu, J.S.C. Jang, J.C. Huang, H.S. Chou, Y. Yang, J.C. Ye, Y.C. Wang, J.W. Lee, F.X. Liu, P.K. Liaw, Y.C. Chen, C.M. Lee, C.L. Li, C. Rullyani, Thin film metallic glasses: unique properties and potential applications, Thin Solid Films 520 (2012) 5097–5122, https://doi.org/10.1016/j.tsf.2012.03.092.
[6] H.W. Sheng, W.K. Luo, F.M. Alamgir, J.M. Bai, E. Ma, Atomic packing and short-to-medium-range order in metallic glasses, Nature 439 (2006) 419–425, https://doi.org/10.1038/nature04421.
[7] A.R. Yavari, Materials science: a new order for metallic glasses, Nature 439 (2006) 405–406, https://doi.org/10.1038/439405a.
[8] D.Z. Chen, C.Y. Shi, Q. An, Q. Zeng, W.L. Mao, W.A. Goddard, J.R. Greer, Fractal atomic-level percolation in metallic glasses, Science 349 (2015) 1306–1310, https://doi.org/10.1126/science.aab1233.
[9] A. Inoue, T. Zhang, T. Masumoto, The structural relaxation and glass transition of La-Al-Ni and Zr-Al-Cu amorphous alloys with a significant supercooled liquid region, J. Non-Cryst. Solids 150 (1992) 396–400, https://doi.org/

10.1016/0022-3093(92)90160-L.
[10] H. Choi-Yim, R. Busch, W.L. Johnson, The effect of silicon on the glass forming ability of the Cu47Ti34Zr11Ni8 bulk metallic glass forming alloy during processing of composites, J. Appl. Phys. 83 (1998) 7993–7997, https://doi.org/10.1063/1.367981.
[11] W.H. Wang, Z. Bian, Ping Wen, Y. Zhang, M.X. Pan, D.Q. Zhao, Role of addition in formation and properties of Zr-based bulk metallic glasses, Intermetallics 10 (2002) 1249–1257, https://doi.org/10.1016/S0966-9795(02)00140-1.
[12] P. Yu, H.Y. Bai, M.B. Tang, W.L. Wang, Excellent Glass-forming Ability in Simple Cu50Zr50-based Alloys, 2005, https://doi.org/10.1016/j.jnoncrysol.2005.03.012.
[13] G. Kumar, T. Ohkubo, T. Mukai, K. Hono, Plasticity and microstructure of Zr–Cu–Al bulk metallic glasses, Scr. Mater. 57 (2007) 173–176, https://doi.org/10.1016/j.scriptamat.2007.02.013.
[14] T.L. Cheung, C.H. Shek, Thermal and mechanical properties of Cu–Zr–Al bulk metallic glasses, J. Alloys Compd. 434 (2007) 71–74, https://doi.org/10.1016/j.jallcom.2006.08.109.
[15] B. Zhang, Y. Jia, S. Wang, G. Li, S. Shan, Z. Zhan, R. Liu, W. Wang, Effect of silicon addition on the glass-forming ability of a Zr–Cu-based alloy, J. Alloys Compd. 468 (2009) 187–190, https://doi.org/10.1016/j.jallcom.2008.01.098.
[16] Y.T. Sun, C.R. Cao, K.Q. Huang, N.J. Zhao, L. Gu, D.N. Zheng, W.H. Wang, Understanding glass-forming ability through sluggish crystallization of atomically thin metallic glassy films, Appl. Phys. Lett. 105 (2014), 051901, https://doi.org/10.1063/1.4892448.
[17] J. Chu, C. Liu, T. Mahalingam, S. Wang, M. O'Keefe, B. Johnson, C. Kuo, Annealing-induced full amorphization in a multicomponent metallic film, Phys. Rev. B 69 (2004), 113410, https://doi.org/10.1103/PhysRevB.69.113410.
[18] P.-T. Chiang, G.-J. Chen, S.-R. Jian, Y.-H. Shih, J.S.-C. Jang, C.-H. Lai, Surface antimicrobial effects of Zr61Al7.5Ni10Cu17.5Si4 thin film metallic glasses on Escherichia coli, Staphylococcus aureus, Pseudomonas aeruginosa, acinetobacter baumannii and Candida albicans, Fooyin J. Heal. Sci. 2 (2010) 12–20, https://doi.org/10.1016/S1877-8607(10)60008-2.
[19] P. Coddet, F. Sanchette, J.C. Rousset, O. Rapaud, C. Coddet, On the elastic modulus and hardness of co-sputtered Zr-Cu-(N) thin metal glass films, Surf. Coating. Technol. 206 (2012) 3567–3571, https://doi.org/10.1016/j.surfcoat.2012.02.036.
[20] M. Apreutesei, P. Steyer, L. Joly-Pottuz, A. Billard, J. Qiao, S. Cardinal, F. Sanchette, J.M. Pelletier, C. Esnouf, Microstructural, thermal and mechanical behavior of co-sputtered binary Zr–Cu thin film metallic glasses, Thin Solid Films 561 (2014) 53–59, https://doi.org/10.1016/j.tsf.2013.05.177.
[21] Y.-L. Deng, J.-W. Lee, B.-S. Lou, J.-G. Duh, J.P. Chu, J.S.-C. Jang, The fabrication and property evaluation of Zr–Ti–B–Si thin film metallic glass materials, Surf. Coating. Technol. 259 (2014) 115–122, https://doi.org/10.1016/j.surfcoat.2014.03.026.
[22] P.C. Wang, J.W. Lee, Y.C. Yang, B.S. Lou, Effects of silicon contents on the characteristics of Zr–Ti–Si–W thin film metallic glasses, Thin Solid Films 618 (2016) 28–35, https://doi.org/10.1016/j.tsf.2016.03.043.
[23] P. Zeman, M. Zítek, Š. Zuzjaková, R. Čerstvý, Amorphous Zr-Cu thin-film alloys with metallic glass behavior, J. Alloys Compd. 696 (2017) 1298–1306, https://doi.org/10.1016/j.jallcom.2016.12.098.
[24] M. Zítek, P. Zeman, Š. Zuzjaková, M. Kotrlová, R. Čerstvý, Tuning properties and behavior of magnetron sputtered Zr-Hf-Cu metallic glasses, J. Alloys Compd. 739 (2018) 848–855, https://doi.org/10.1016/j.jallcom.2017.12.301.
[25] W.C. Oliver, G.M. Pharr, An improved technique for determining hardness and elastic modulus using load and displacement sensing indentation experiments, J. Mater. Res. 7 (1992) 1564–1583, https://doi.org/10.1557/JMR.1992.1564.
[26] W. Eckstein, Sputtering yields, in: Sputtering by Part. Bombard, Springer, Berlin, 2007.
[27] J. Houska, S. Kos, Ab initio modeling of complex amorphous transition-metal-based ceramics, J. Phys. Condens. Matter 23 (2011), https://doi.org/10.1088/0953-8984/23/2/025502.
[28] S. Bose, High Temperature Coatings, first ed., Elsevier Inc., 2007 https://doi.org/10.1016/B978-0-7506-8252-7.X5000-8.

C

Metastable structures in magnetron sputtered W–Zr thin-film alloys

M. Červená, R. Čerstvý, T. Dvořák, J. Rezek, P. Zeman
submitted to Journal of Alloys and Compounds (2021)

Abstract

Binary W–Zr thin-film alloys with different metastable structures were prepared by dc magnetron co-sputtering of W and Zr targets in argon atmosphere on unheated and unbiased substrates. The effect of the elemental composition on the formation of different structures and phases was studied in a very wide range of 3 – 99 at.% Zr. The microstructure and properties of the films were related to the individual metastable structures prepared. We found that W-rich films with an α-W(Zr) solid solution structure can be prepared in much wider range of the elemental composition (up to 24 at.% Zr) than indicated in the equilibrium W–Zr phase diagram. These films exhibited an enhanced hardness (up to 16.1 GPa) and a reduced residual stress (down to -0.05 GPa). Amorphous W–Zr films with a very low surface roughness (down to 0.4 nm) and metallic glass features were prepared with the Zr content between 33 and 83 at.%. The hardness of these films gradually decreased with increasing Zr content due to reducing average bond energy. All films were in the compressive state in contrast to the crystalline ones. The structure of crystalline Zr-rich films with higher than 88 at.% Zr was predominantly dual-phased exhibiting a gradual transition from a metastable β-Zr(W) solid solution (86 – 96 at.% Zr) through a metastable ω-Zr(W) solid solution (94 – 100 at.% Zr) to the thermodynamically stable α-Zr phase (99 – 100 at.% Zr) with increasing Zr (decreasing W) content. We also observed the formation of dual-phase glassy-crystalline structures in the transition zones between fully crystalline and glassy films.

Keywords: W–Zr; Thin film; Metastable structure; Metallic glass; Magnetron sputtering

1. Introduction

Metastable solid materials such as amorphous or nanocrystalline alloys, supersaturated solid solutions or high-temperature or high-pressure phases persisting at normal conditions, are of great interest due to a possibility to explore novel structures with unknown properties. These materials are kinetically determined and can be therefore synthesized only by non-equilibrium processes. Magnetron sputtering is thus a suitable technique for their preparation as thin films.

In the last years, the development of Zr-based alloys in a form of thin films has received much attention due to the unique properties of these films, such as high hardness, low wear and high corrosion resistance, antimicrobial activity and biocompatibility [1–5]. On the other hand, tungsten exhibits even higher hardness, high thermal conductivity and has the highest melting point of all metals (3422 °C) [6–8]. Therefore, its combination with Zr or Zr-based alloys might be an effective way how to further enhance the mechanical, thermal and functional properties.

It is well known that the elemental zirconium crystallizes in a hexagonal close-packed structure (α-Zr phase) with a P63/mmc space group at ambient conditions. This structure transforms to a body-centered cubic structure (β-Zr phase) with an Im3m space group at a temperature of 863 °C at atmospheric pressure. The α phase can be also transformed into another hexagonal structure (ω-Zr phase) with a P6/mmm space group, which is known as the high-pressure phase occurring at pressures of 2.2 – 4.5 GPa at ambient temperature [9–13]. The elemental tungsten crystallizes in a body-centered cubic structure (α-W phase) with an Im3m space group at ambient conditions. This space group is identical to that of the β-Zr phase. Tungsten can also crystallize in a simple cubic structure (β-W phase) with a Pm-3m space group, which is also known as the metastable A-15 cubic phase. It was found that the formation of the β-W phase strongly depends on the concentration of impurities or deposition parameters [14–16]. The mutual solid solubility of Zr in α-W and W in α-Zr is negligible at ambient temperature according to the equilibrium W–Zr phase diagram [17]. The solubilities increase with increasing temperature and reach maxima of 3.56 at.% Zr in α-W at a peritectic temperature of 2160 °C and 3.98 at.% W in β-Zr at a eutectic temperature of 1739 °C. Besides, one intermetallic W_2Zr phase exists in the narrow window of the elemental composition (33 – 35 at.% Zr). This phase decomposes peritectically at 2160 °C [18–20].

As far as we know, only a few studies have focused on investigation of magnetron sputtered W–Zr alloys and mostly examined only a few material properties in a certain range of the elemental composition [21–23]. This paper is, therefore, focused on the W–Zr thin-film alloys

prepared in a very wide composition range (3 – 99 at.% Zr) with the aim to identify structures and phases, including metastable ones, that can be prepared by non-equilibrium process of magnetron sputtering, and to characterize their structure, microstructure, surface morphology, mechanical properties and electrical resistivity in detail.

2. Experimental details

Binary W–Zr films were prepared by non-reactive dc magnetron sputtering in a sputter system (ATC 220-V, AJA International). The vacuum chamber was pumped down to a base pressure lower than 5×10^{-5} Pa before each deposition by a turbomolecular pump (1200 l/s), which was backed up with a multi-stage roots pump (23 m^3/h). The depositions were carried out in argon atmosphere at a pressure of 0.533 Pa. The thickness of all deposited films was around 2 µm.

Two independent unbalanced magnetrons with indirectly cooled circular targets with 50.8 mm in diameter were used for the depositions. One was equipped with the W target (99.95 % purity) and the other one with the Zr target (99.7 % purity). Both magnetrons were powered by dc power supplies (Pinnacle plus+ 5kW, Advanced Energy and DCXS–750–4, AJA). The films were deposited onto Si(100) substrates, which were ultrasonically pre-cleaned in isopropyl alcohol. The substrates were held at a floating potential without any external heating. The target-to-substrate distance was set to 150 mm and the substrates were rotated with a constant speed of 40 rpm.

The deposition rate was measured before each deposition by a quartz crystal deposition rate monitor (SQM-160, Inficon). The ratio of the deposition rates of W and Zr corresponding to a particular elemental composition of the films was then used for the determination of the ratio of the powers delivered to the targets with the effort to keep a maximum value of 260 W at one of the targets to achieve a deposition rate as high as possible.

The elemental composition of the films was measured by energy dispersive spectroscopy (EDS, Thermo Scientific UltraDry) in a scanning electron microscope (Su-70, Hitachi) with the primary electron energy of 15 kV. For the quantitative analysis, Zr and W bulk standards were used. Electron microscopy with the same primary electron energy was also used to take cross-sectional images of the films. For the cross-section imaging, the films on the Si substrate were fractured at ambient conditions.

The structure of the films was characterized by glancing incidence X-ray diffraction (GIXRD) using a diffractometer (X'Pert PRO MPD, PANalytical) working with a CuK_{α} (λ = 0.154187 nm) radiation at a glancing angle of 2°. The tube was operating under an accelerating voltage of 40 kV with a tube current of 40 mA. Continuous scan was done with a scan step size of 0.05° and time per step 3 s in the 2θ range of 20 – 80°. The data evaluation was performed with a PANalytical software package HighScore Plus. The influence of the instrument on diffraction peaks broadening was evaluated using an NIST powder standard LaB_6.

The hardness of the films was determined from load vs. displacement curves measured in air at ambient temperature by a nanoindenter (TI 950 Triboindenter, Hysitron) with the Berkovich diamond tip. The indentation depth was in all measurements lower than 10% of the film thickness with a loading force of 10 mN. A microindenter (H100 microindenter, Fischerscope) with the Vickers diamond tip and a loading force of 300 mN was used in case of an amorphous W–Zr film to create an indentation imprint with easily recognizable shear bands.

To determine the film thickness and its curvature, a profilometer (Dektak 8 Stylus Profiler, Veeco) was used. The measurements were carried out on the Si substrates coated with the film. The residual stress was determined using modified Stoney's formula.

The arithmetic average surface roughness and surface morphology of the W–Zr films were measured by atomic force microscopy (SmartSPM, AIST-NT) on a characteristic 5 × 5 μm^2 area of the film. The microscope was equipped with a silicon tip with a nominal radius of 10 nm and worked in a tapping semi-contact mode. The same configuration was also used for a detailed examination of the indentation imprint.

The electrical resistivity of the films on the Si substrate at room temperature was analyzed by the standard four-point method with a Keithleys system with a spacing between used head's tips of 1.047 mm. The electrical resistivity of all films was much lower than that of the Si(100) substrate (7.3×10^{-3} Ωm) used. The measurement of each sample was performed twice. Before the second measurement, the specimen was 90° rotated to eliminate the possibility of a different electrical resistivity for different directions.

3. Results and discussion

This section is divided into five subsections, where the effect of a gradual substitution of Zr for W on the properties of as-deposited W–Zr films is discussed. The first subsection presents the

elemental composition of the films as a function of the ratio of the deposition rates. The second one focuses on the evolution of the structure and structural characteristics with increasing Zr content. In the third one, the evolution of the microstructure, surface morphology and surface roughness is discussed with respect to the occurrence of individual metastable structures. The fourth subsection presents the hardness and residual stress of the films and the last one focuses on their electrical resistivity.

3.1. Elemental composition

The elemental composition of the W–Zr films, presented in Fig. 1, was gradually varied by controlling the ratio of the deposition rates, a_D^W/a_D^{Zr}, from the W and Zr targets (see Experimental for more details). The total deposition rate in the film series ranged between 13.5 and 28 nm/min depending on the target power conditions. A large number of films were prepared in a very wide range of the composition from 3 to 99 at.% Zr. In addition, pure W and Zr films, which we used as reference samples, were also deposited. From Fig. 1 it can be observed that a W–Zr film with 50 at.% Zr and W (an intersection of the curves) is prepared at a_D^W/a_D^{Zr} = 0.58. This value does not exactly correspond to the ratio of the molar volumes of Zr (14.02 cm^3/mol) and W atoms (9.47 cm^3/mol) as we observed, for instance, for binary Zr–Cu films [24]. This discrepancy is more pronounced for higher a_D^W/a_D^{Zr} ratios and can be attributed to the same effect that we observed in case of ternary Zr–Hf–Cu films with heavy Hf [25]. During sputtering, Ar ions attracted to and impacted on the W target with a high atomic mass are neutralized and backscattered towards the substrate with high energies causing preferential resputtering of lighter Zr atoms from the growing film. Another effect can be also taken into consideration. As the fluxes of sputtered Zr and W atoms from the inclined magnetrons encounter each other in front of the substrate, lighter Zr atoms can be scattered by heavier W atoms away from the substrate. Both effects can contribute to an enriched composition of the films in W than expected from the ratio of the molar volumes.

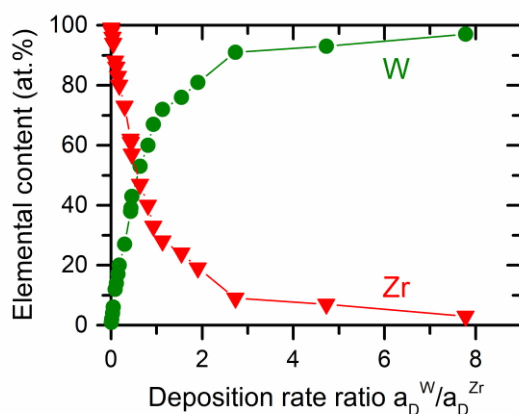

Fig. 1. Dependence of the elemental composition of W–Zr films on the a_D^W/ a_D^{Zr} ratio of the deposition rates.

3.2 Structure

The structure of the as-deposited W–Zr films with a varying Zr content was analyzed by GIXRD (Fig. 2). As can be seen in Fig. 2a, the structure of the pure W film with 0 at.% Zr is crystalline corresponding to the body-centered cubic (bcc) α-W phase (PDF Card No. 00-004-0806). An addition of up to 24 at.% Zr does not change the bcc lattice type, but it leads to the formation of an α-W(Zr) solid solution. A gradual substitution of larger Zr (1.55 Å) for smaller W atoms (1.35 Å) in the bcc lattice of α-W results in a gradual shift of the maxima of the diffraction peaks to lower 2θ angles (see Fig. 2a).

The film with 28 at.% Zr is characterized by the transition between a crystalline and amorphous structure. Its XRD pattern consists of sharp α-W(Zr) diffraction peaks and a broad amorphous hump at a 2θ position of about 39°, which is overlapped by one of the diffraction peaks. An addition of Zr in a wide range of 33 to 83 at.% leads to a fully amorphous structure of the films (Fig. 2b). Then, one can observe that the films with 86 and 88 at.% Zr are no longer fully amorphous and lie in the transition zone between an amorphous and crystalline structure. They contain a crystalline phase corresponding to a β-Zr(W) solid solution with diffraction peaks slightly shifted to higher 2θ angles compared to the pure bcc β-Zr phase (PDF Card No. 00-34-0657). This is caused by an incorporation of W into the β-Zr lattice. Concurrently, they are still characterized by an amorphous hump (light green curves in Fig. 2c) at a 2θ position of about 36°. Its intensity, however, decreases with increasing Zr content.

In case of the film with 94 at.% Zr, the structure is crystalline consisting of β-Zr(W) and ω-Zr(W) solid solutions. Analyzing the XRD pattern, we found that β-Zr(W) appears to be a major

phase in this film and diffraction peaks, especially for the ω-Zr(W) phase, are shifted to higher 2θ angles compared to the pure bcc β-Zr phase and the hexagonal close-packed (hcp) ω-Zr phase (PDF Card No. 04-004-5067). The structure of the film with 96 at.% Zr is of the same phase composition, but with the dominant ω-Zr(W) phase in this case. The film with 98 at.% Zr then exhibits a crystalline structure containing the ω-Zr(W) phase only. Further increase of the Zr content to 99 at.% leads to the formation of the hcp α-Zr phase (PDF Card No. 00-05-0665) in addition to the major ω-Zr(W) phase. Finally, an XRD pattern of the pure Zr film (100 at.% Zr) is characterized by an appearance of diffraction peaks that can be assigned to the α-Zr phase with a trace amount of the ω-Zr phase.

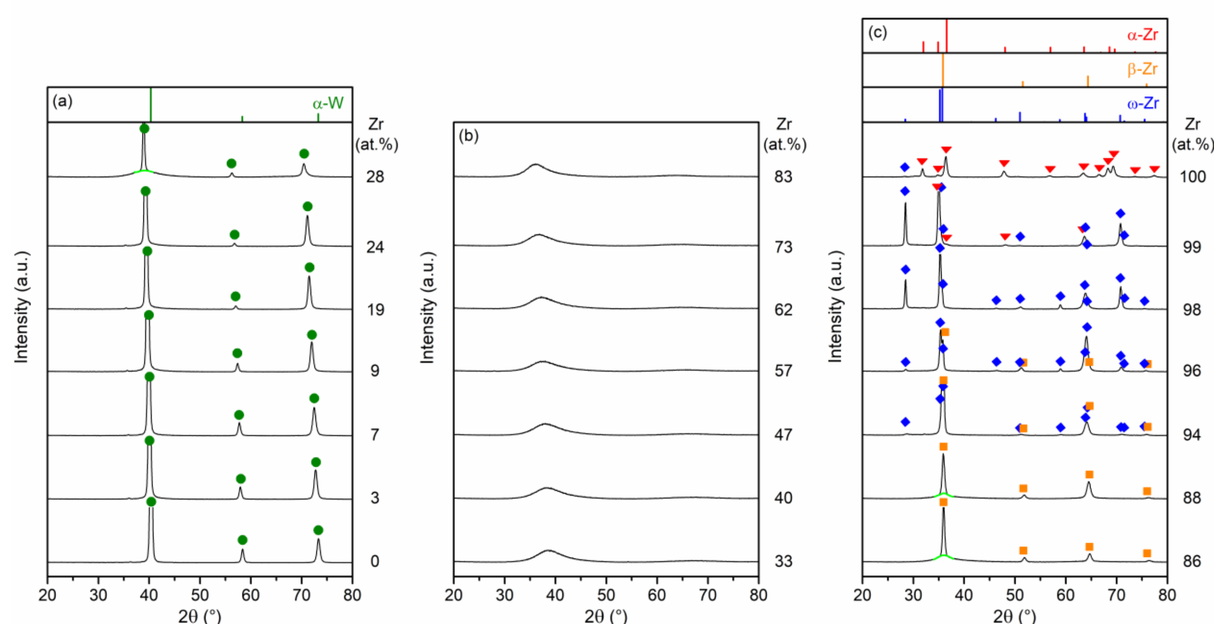

Fig. 2. XRD patterns of as-deposited W–Zr films divided into three groups: (a) crystalline W-rich films with α-W(Zr) solid solution structure, (b) amorphous films, and (c) crystalline Zr-rich films with Zr(W) solid solution structures.

The effect of the elemental composition on the phase composition of the W–Zr films is summarized in Table 1, where the dominant (major) phase is first in the order. Since we were not able to decide which phase is dominant in the case of a crystalline-amorphous structure, so the crystalline phase is always listed first there.

We can conclude that a gradual addition of Zr leads to the formation of several metastable structures in magnetron sputtered W–Zr films. The W-rich films (≤ 24 at.% Zr) are single-phase materials with the supersaturated α-W(Zr) solid solution structure. The composition range of the solid solution is significantly wider than indicated in the equilibrium W–Zr phase diagram

[17]. The W–Zr films are also prepared as single-phase materials with a fully amorphous structure and metallic glass features (shown later) in the very wide range of the Zr content between 33 and 83 at.%. Let us note that all these observations are in a very good agreement with those reported by Horwat et. al [23] for W–Zr films investigated in the range of 19 – 57 at.% Zr.

The Zr-rich films (> 88 at.% Zr) are predominantly dual-phase crystalline materials exhibiting a gradual transition of the structure type from β-Zr through ω-Zr to α-Zr with increasing Zr (decreasing W) content. The high-temperature β-Zr and high-pressure ω-Zr structures are metastable at normal conditions. The formation of the β-Zr(W) and ω-Zr(W) solid solutions in the W–Zr films is thus initiated by the non-equilibrium process of magnetron sputtering that generates high temperatures and high pressures at the atomic scale [26]. In addition, the formation of the β-Zr(W) solid solution at a higher W incorporation is attributed to the same crystal structure of β-Zr and α-W (the Im3m space group). The stabilization of the high-temperature β-Ti phase by a W incorporation has also been reported by Musil et al. [27]. A lower incorporation of smaller W atoms then favors the ω-Zr(W) structure via the generation of compressive lattice stress fields. In addition to these results, we also identified transition zones where the dual-phase crystalline-amorphous structures are evolved, see the phase composition for 28 and 83 – 86 at.% Zr.

Tab. 1. Phase composition of prepared W–Zr films.

Zr content (at. %)	Phase composition
0	α-W
3 – 24	α-W(Zr)
28	α-W(Zr) + amorphous
33 – 83	amorphous
86 – 88	β-Zr(W) + amorphous
94	β-Zr(W) + ω-Zr(W)
96	ω-Zr(W) + β-Zr(W)
98	ω-Zr(W)
99	ω-Zr(W) + α-Zr(W)
100	α-Zr + ω-Zr

In addition to the phase composition identification, we also carried out a more detailed structural analysis of the W–Zr films. The evolution of the strain-free lattice parameter a with increasing Zr content for the films with the bcc lattices is shown in the upper panel of Fig. 3. The lattice parameter was calculated from the positions of diffraction peaks measured by GIXRD, where diffracting planes make angles $\psi = \theta - \gamma$ with the flat film surface (θ is the Bragg angle and γ is the angle of incidence of the primary beam).

In materials with a cubic crystal lattice being under uniaxial residual stress, the lattice parameter a depends linearly on $\sin^2\psi$ [28,29]:

$$a = a_{\perp} + (a_{\parallel} - a_{\perp}) \sin^2 \psi, \tag{1}$$

where $a_{\parallel}$ and $a_{\perp}$ are the in-plane lattice parameter ($\psi = 90°$) and the lattice parameter normal to the sample surface ($\psi = 0°$), respectively. They can be employed for the calculation of the strain-free lattice parameter a_0 if Poisson's ratio ν of the material is known [28]:

$$a_0 = a_{\perp} + \frac{2\nu}{\nu + 1}(a_{\parallel} - a_{\perp}). \tag{2}$$

In our case, $\nu = 0.28$ [30] was used for the evaluation of the W-rich films with the bcc α-W(Zr) structure and $\nu = 0.34$ [31] for the Zr-rich films with the bcc β-Zr(W) structure.

As you can see in Fig. 3, the strain-free lattice parameters gradually increase with increasing Zr content, which results from the shift of diffraction peaks in Fig. 2 and can be explained by the fact that the larger Zr atoms gradually substitute the smaller W atoms in the α-W lattice and vice versa in the β-Zr one. These dependences are linear and can be described by Vegard's law for substitutional solid solutions [32]. The strain-free lattice parameters in Fig. 3 are shown only for the bcc lattices of the α-W(Zr) and β-Zr(W) structures, both with the Im3m space group. In case of the α-Zr(W) and ω-Zr(W) phases with the hcp lattices, the determination of the strain-free lattice parameters is more complicated and have not been done.

From the position of the maximum of the amorphous humps, the evolution of the distance between nearest-neighbor atoms in the amorphous matrix with increasing Zr content can be evaluated [33], see the bottom panel of Fig. 3. Similarly to the evolution of the strain-free lattice parameter, the nearest-neighbor distance linearly increases with increasing Zr content from 33 up to 83 at.% Zr due to the same effect of the gradual substitution of larger Zr atoms for smaller W atoms in the film structure. In addition, the values of the nearest-neighbor distance in the

pure W and Zr films can be obtained by extending the fitted dash line in Fig. 3. It is seen that these values are very close to the distance of the nearest Zr atoms (3.1 Å) and W atoms (2.7 Å) in their crystalline lattices.

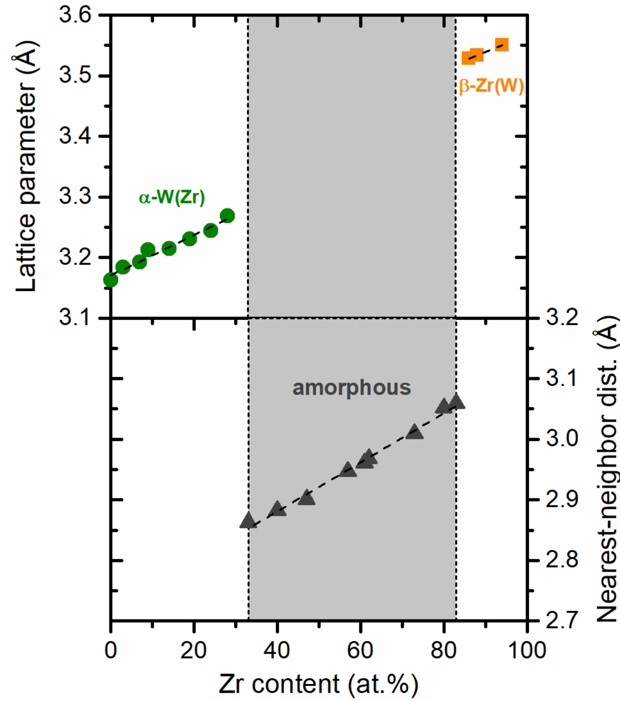

Fig. 3. Evolution of the lattice parameters (upper panel) of W–Zr films with the bcc Im3m lattices and the nearest-neighbor distance (bottom panel) of amorphous W–Zr films with increasing Zr content.

Fig. 4 presents the Williamson-Hall plot of the pure W film and of two representative W-rich films with the α-W(Zr) solid solution structure, which is a classical method to obtain a quantitative information on the average crystallite size and microstrain from the peak broadening. Williamson and Hall [34–35] assumed that both size and strain broadened profiles are Lorentzian so the crystallite size and microstrain contributions to peak broadening are independent of one another and are additive. Based on this assumption, a mathematical relation was established between the peak breadth *B*, average crystallite size *D* and the microstrain ε as follows:

$$\frac{B\cos\theta}{\lambda} = \frac{1}{D} + 2\varepsilon\left(\frac{2\sin\theta}{\lambda}\right). \tag{3}$$

By plotting $\frac{B\cos\theta}{\lambda}$ versus $\frac{2\sin\theta}{\lambda}$ and fitting the data with a linear function, ε can be estimated from the slope of the straight line and *D* from the ordinate intercept.

From Fig. 4 it is seen that all straight lines have high slopes (the scale of the vertical axis is of the order of 10^3) implying that the microstrain has a dominant effect on the broadening of the diffraction peaks. The value of the microstrain ranges between 0.30 – 0.35 % for the films with 0 – 24 at.% Zr and does not show an apparent dependence on the Zr content. Such high values of the microstrain in the as-deposited W-rich films are probably caused by the high melting point of W (3422 °C), which prevents the relaxation of defects during the deposition at ambient temperature.

Since the straight lines intersect the vertical axis close to the origin, the size of the crystallites in the films will be unrealistically high. This is because the broadening of the diffraction peaks caused by the crystallites themselves is much smaller than the broadening caused by the instrument used (determined using the LaB_6 standard). In other words, we can only state that the crystallite size in the films is higher than ≈ 100 nm, which is the upper limit that can be determined using our GIXRD. Hence, the Scherrer formula cannot be used either, because the microstrain cannot be neglected. One should always be careful to use the Scherrer formula if the effect of the microstrain on the peak broadening has not been evaluated.

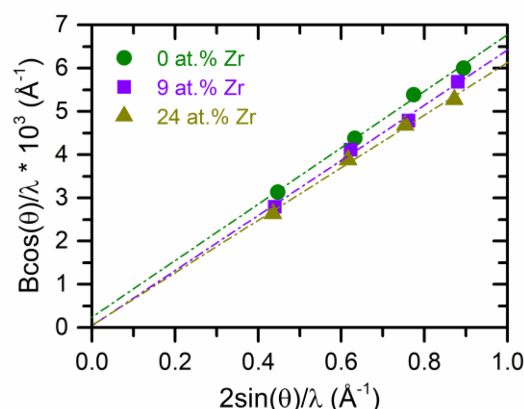

Fig. 4. Williamson-Hall plots of selected W–Zr films with an α-W(Zr) solid solution structure (0, 9 and 24 at.% Zr).

3.3 Microstructure and surface morphology

The microstructure of the W–Zr films in cross-sections was examined by SEM in the mode of secondary electrons. Fig. 5 shows the corresponding micrographs for a varying Zr content. It can be seen that the pure W film and the W-rich films with the α-W(Zr) structure (left column in Fig. 5) exhibit a fully developed columnar microstructure without any distinct voids and with a column height comparable to the film thickness. From the micrograph of the film with 28 at.%

Zr (bottom middle in Fig. 5), it is apparent that its microstructure consists of both an amorphous and crystalline phase. This observation is in good agreement with the results obtained by GIXRD as discussed above (Fig. 2a). An examination of this dual-phase structure revealed that the crystalline part is columnar, without distinguishable voids between the columns, forming conical domains that are surrounded by an amorphous phase with vein-like patterns. The conical domains have their axes perpendicular to the film surface and the apex at or close to the substrate surface. The vein-like features, which are typical for the metallic glasses, are created during the breaking of the sample and are caused by an inhomogeneous distribution of plastic deformation and the formation of shear bands. More detailed investigation of this film with a dual-phase glassy-crystalline structure has been published in our very recent short communication [36]. As you can see in the middle column in Fig. 5, the microstructure of the fully amorphous W–Zr films exhibits in all cases a vein-like pattern and/or striations proving that these films are the metallic glasses. Other features related to the metallic glasses, known as shear bands, will be shown in Fig. 9. The film with 86 at.% Zr (bottom right in Fig. 5), consisting of the crystalline β-Zr(W) solid solution and amorphous structure, is characterized by a combination of a columnar microstructure and vein-like pattern. While the columns are more clearly visible near the surface, the vein-like features are more pronounced in the rest of the film. The films with 94 – 100 at.% Zr in the right column in Fig. 5 then represent materials with a well-developed columnar microstructure and a different amount of ω-Zr(W) phase in their structure. In case of the film with 94 at.% Zr, a small amount of an amorphous phase near the substrate still cannot be ruled out. It is seen that the film with the single-phase ω-Zr(W) structure (98 at.% Zr) exhibits clearly distinguishable V-shaped columns being sticking to each other. The columns width increases with the film thickness and is larger than in the case of the pure Zr film (top right in Fig. 5) with the nearly single-phase α-Zr structure. Note that this observation can be related to approximately opposite dimensions of the lattice parameters of the hcp lattices of α-Zr and ω-Zr.

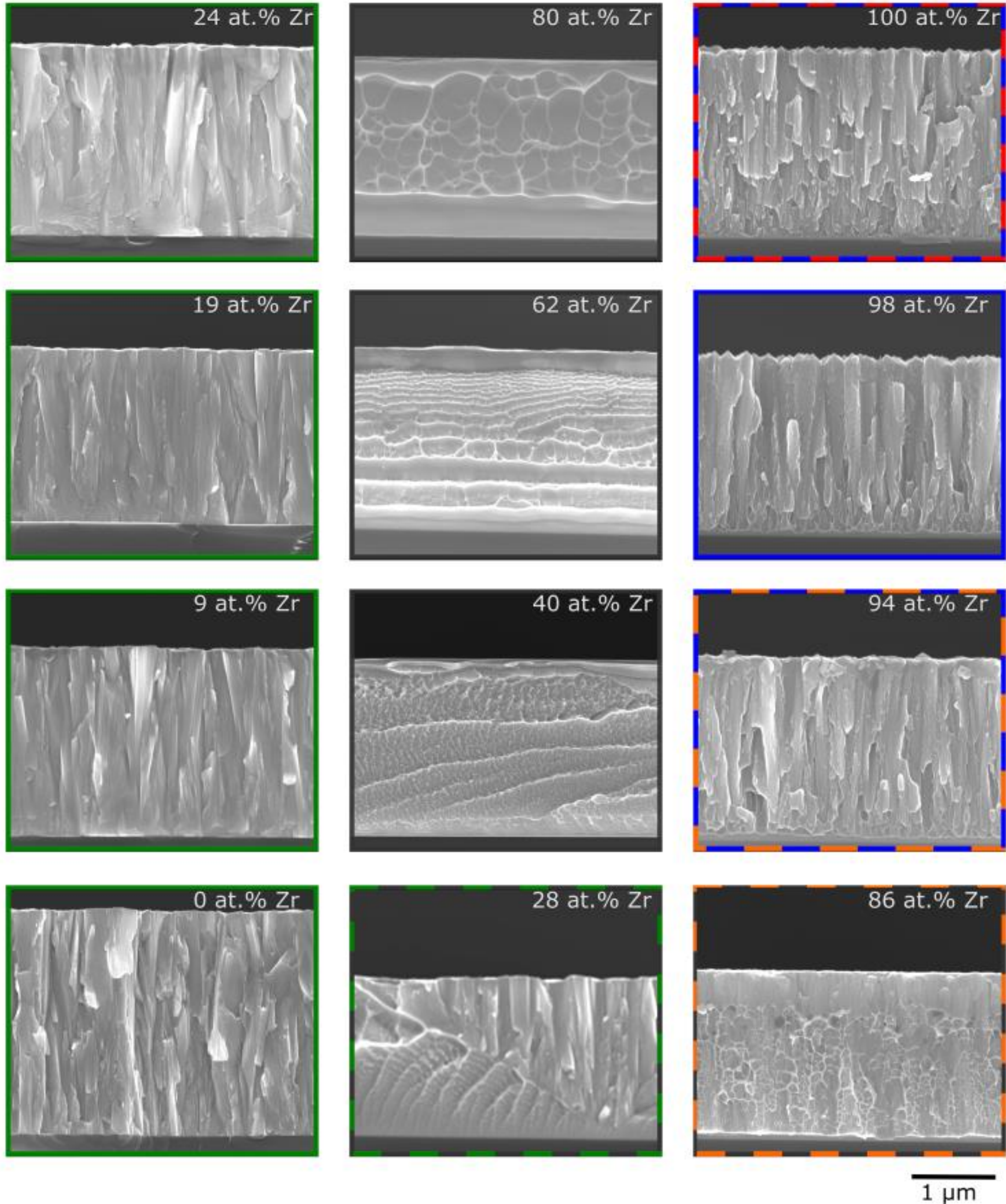

Fig. 5. Microstructure of W-rich films with an α-W(Zr) solid solution structure (green frame), amorphous W–Zr films (dark grey frame) and Zr-rich films with a β-Zr(W) (orange frame), ω-Zr(W) (blue frame) or α-Zr (red frame) solid solution structures or their combinations.

The evolution of the surface morphology and the arithmetic average surface roughness with increasing Zr content in the W–Zr films is shown in Fig. 6 and Fig. 7, respectively. The surface

morphology reflects the microstructure of the films in their cross-section presented in Fig. 5. It is evident that the surface morphology of all W-rich films with the α-W(Zr) structure (left column in Fig. 6) is very similar consisting of rather rounded facets. The surface roughness of these films increases with increasing Zr content from 7.0 to 12.4 nm and is significantly higher than that of the amorphous films (compare left and middle column in Fig. 6). Such a smooth surface with the surface roughness down to 0.4 nm is typical for the metallic glasses, which provides further indication that the amorphous W–Zr films discussed in this paper are the metallic glasses. The film with 28 at.% Zr then represents a film with a dual glassy-crystalline structure with a surface roughness of 0.2 nm for the amorphous and 10.0 nm for the crystalline part. On the other hand, the combination of the amorphous and crystalline β-Zr(W) structure in case of the Zr-rich film with 86 at.% Zr leads to a uniform surface morphology with a surface roughness of 4.7 nm. The surface morphology of the film with 94 at.% Zr is more diverse consisting of a combination of higher and lower sharp peaks, which can be well ascribed to the presence of two different phases, β-Zr(W) and ω-Zr(W). From the surface morphology of the film with the pure ω-Zr(W) phase (98 at.% Zr), it is obvious that the higher peaks originate from the ω-Zr(W) phase. This is proved also by a higher surface roughness of 28.0 nm for the film with 98 at.% Zr compared to 15.2 nm for the film with 94 at.% Zr (see Fig. 7). The surface morphology of the pure Zr film with the nearly single-phase α-Zr structure is similar to that of the film with the single-phase ω-Zr(W) structure, but the surface peaks are smaller and finer. This is in agreement with the narrower columns observed in the microstructure of this film. The surface roughness accordingly decreases to 16.9 nm.

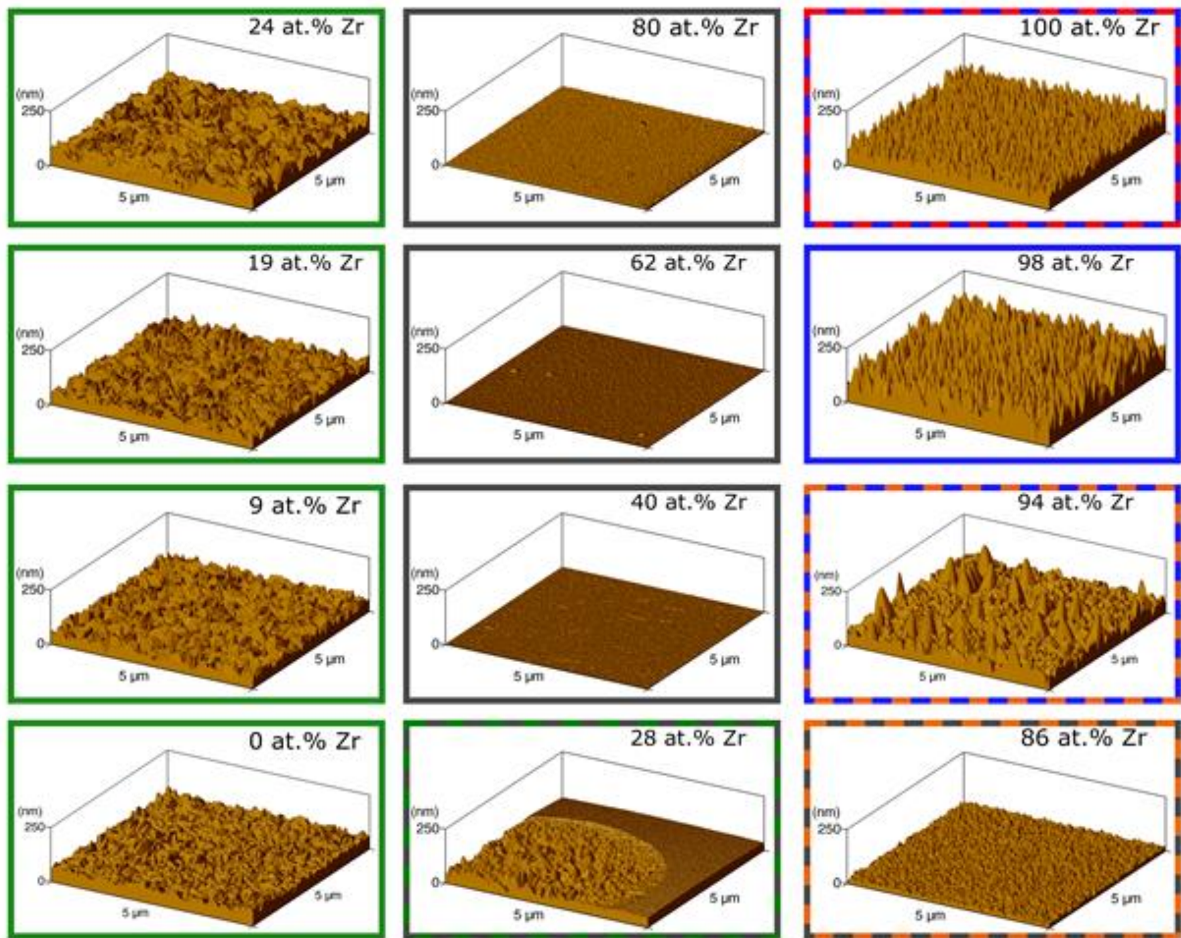

Fig. 6. Surface morphology of W-rich films with an α-W(Zr) solid solution structure (green frame), amorphous W–Zr films (dark grey frame) and Zr-rich films with a β-Zr(W) (orange frame), ω-Zr(W) (blue frame) or α-Zr (red frame) solid solution structures or their combinations.

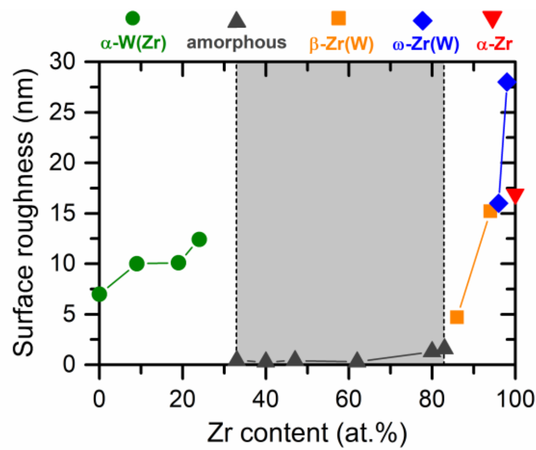

Fig. 7. Surface roughness of W–Zr films. The grey area represents films with an amorphous structure.

3.4 Hardness and residual stress

The effect of Zr content in the W–Zr films on the hardness is displayed in the upper panel of Fig. 8. As can be seen, an addition of Zr leads to an increase of the hardness from 12.7 GPa for the pure W film to an average value of about 15 GPa for the W-rich films with up to 24 at.% Zr and the α-W(Zr) structure (with a maximum value of 16.1 GPa at 7 at.% Zr corresponding to more than 25% hardness enhancement). This phenomenon is known as a solid-solution hardening, where the addition of another soluble element (up to some certain amount) leads to an increase of the strength of the matrix [37]. As the amorphous or glassy phase is formed in the structure of the film, the hardness decreases approximately linearly down to 4.7 GPa. This can be explained by the fact that the substitution of Zr for W leads to a weaker covalent component of the metallic-covalent bonds, because the valence d-orbitals of Zr are less filled and overlap less than in the case of W. The weaker covalent bonds result in a lower bond energy and in turn in a lower hardness. It is, however, worth noting that the amorphous W–Zr films with metallic glass behavior can be formed with a high hardness up to 12.1 GPa (see the value for the film with 33 at.% Zr). An increase of Zr content above 86 at.% leads then to a slight increase in the hardness due to the formation of the crystalline β-Zr(W) phase at the expense of the amorphous one. It can be also seen that the films composed of a mixture of β-Zr(W) and ω-Zr(W) phases (94 at.% and 96 at.% Zr) exhibit the highest hardness (5.4 GPa) among the Zr-rich films. The hardness of the films with ω-Zr(W) or α-Zr phases or their mutual combination is slightly lower, ranging from 4.6 – 4.9 GPa.

The bottom panel of Fig. 8 presents the values of residual stress of the W–Zr films. It is evident that all W-rich films with the α-W(Zr) solid solution structure (0 – 24 at.% Zr) exhibit low tensile or very low compressive stress with the values varying between 0.4 and -0.05 GPa. On the other hand, the films with a combination of the amorphous and crystalline (28 at.% Zr) structure or with the fully amorphous structure (33 – 83 at.% Zr) are in a compressive residual stress, which gradually decreases with increasing Zr content. The maximum value of the compressive residual stress of -0.72 GPa was measured for the film with 40 at.% Zr. A minimum value of -0.16 GPa was then obtained in case of the film with 80 at.% Zr. The crystalline Zr-rich films with the structure consisting of β-Zr(W), ω-Zr(W) or α-Zr phases or a combination thereof (86 – 100 at.% Zr) exhibit a tensile residual stress with a maximum value of 0.41 GPa (99 at.% Zr).

Let us note that all W–Zr films were deposited on unbiased and unheated substrates. Therefore, hardness and residual stress are not optimized, but reflect the microstructure and characteristics

of individual metastable structures.

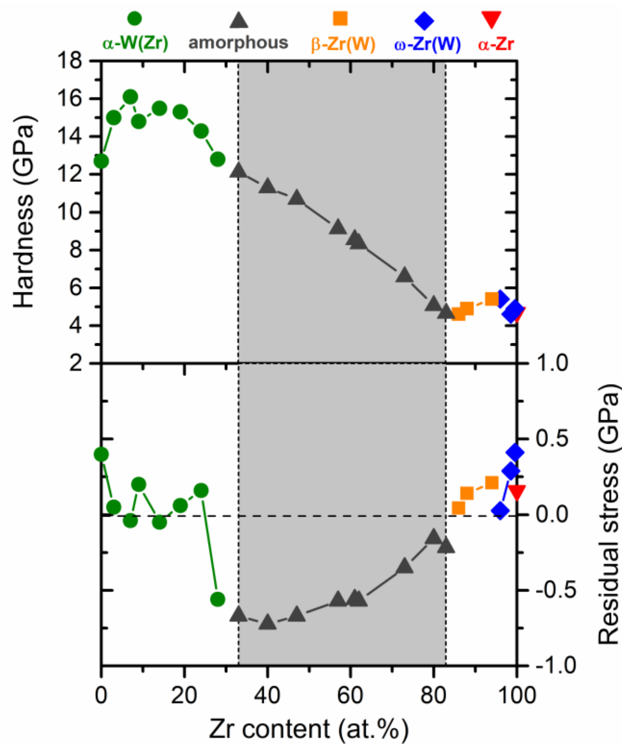

Fig. 8. Hardness and residual stress of W–Zr films. The grey area represents films with an amorphous structure.

A Vickers indent made on the amorphous film with 62 at.% Zr at a load of 300 mN was examined by atomic force microscopy (Fig. 9). As you can see, pile-ups developed around the indent upon the indentation contain shear bands that occur as a consequence of relieving of an accumulated localized plastic stress. This is, along with the aforementioned vein-like patterns, striations and very smooth surface, further indication that the amorphous W–Zr films are certainly the metallic glasses.

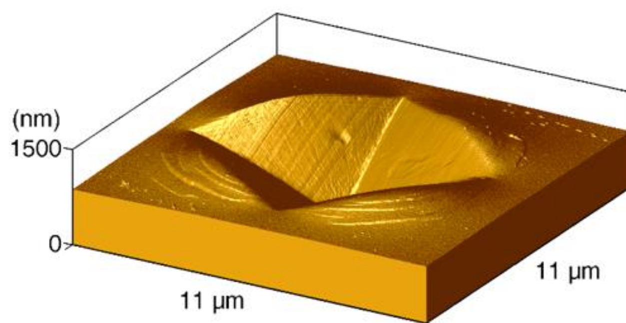

Fig. 9. AFM image of an indent made at a load of 300 mN on an amorphous W–Zr film with 62 at.% Zr.

3.5 Electrical resistivity

Fig. 10 presents the dependence of the electrical resistivity of the W–Zr films (measured at room temperature) on the Zr content. The electrical resistivity of the pure W film is 0.8×10^{-7} Ωm and increases (more steeply than what would correspond to a weighted average of pure W and pure Zr) with increasing Zr content for the W-rich films with the α-W(Zr) structure. It is about 5.6×10^{-7} Ωm for the films with 19 and 24 at.% Zr. Since the lattice microstrain does not show any increasing trend with the substitution of Zr for W (Subsection 3.2), the increase of the electrical resistivity is not related to structural lattice defects but rather to a change in the chemical composition. As Zr gradually substitutes W in the bcc lattice, the mean free path of conductive electrons (sitting in delocalized states with a high weight on *s*-orbitals) gets shorter because the corresponding electronic states get more localized. A further increase in the Zr content to 28 at.% Zr leads to a jump of the electrical resistivity to 13.3×10^{-7} Ωm, which corresponds to the transition of the structure from crystalline to partially or fully amorphous. All amorphous films (up to 80 at.% Zr) exhibit a very similar value of the electrical resistivity. A high disorder of the amorphous structure compared to the crystalline one leads to the free mean path of electrons as short as possible (approaching the interatomic distance), which in turn results in the highest values of the electrical resistivity (approaching the Ioffe-Regel limit) independent of the chemical composition. A slightly lower value (around 10.5×10^{-7} Ωm) is measured for the film with 83 at.% Zr. In case of the crystalline Zr-rich films, we found that the electrical resistivity of the films with the dominant β-Zr(W) phase is slightly higher than that with the dominant ω-Zr(W) phase and that is comparable with that of the film with the dominant α-Zr phase.

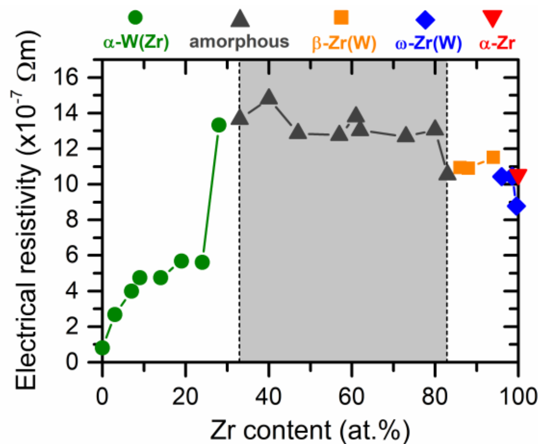

Fig. 10. Electrical resistivity of W–Zr films. The grey area represents films with an amorphous structure.

4. Conclusions

Using the non-equilibrium process of non-reactive dc magnetron co-sputtering of Zr and W targets, we showed that different metastable structures can be prepared in the binary W–Zr system. The W–Zr thin-film alloys were deposited in a very wide composition range (3 – 99 at.% Zr) onto unheated and unbiased substrates and systematically characterized in the as-deposited state.

W-rich films with up to 24 at.% Zr were prepared as single-phase crystalline materials with a supersaturated α-W(Zr) solid solution structure and columnar microstructure. A gradual substitution of Zr for W in the bcc α-W lattice led to an increase of the hardness due to solid-solution hardening (up to 16.1 GPa), decrease of the residual stress (down to -0.05 GPa), and increase of the surface roughness (up to 12.4 nm) and the electrical resistivity (up to 5.6×10^{-7} Ωm) compared to a pure W film. An addition of 28 at.% Zr resulted in the formation of a dual-phase glassy-crystalline structure consisting of columnar conical crystalline domains of the α-W(Zr) structure surrounded by a W–Zr metallic glass. Fully amorphous W–Zr films with metallic glass features were prepared in a wide range of 33 – 83 at.% Zr. These films were characterized by a very low surface roughness (down to 0.4 nm), compressive stress (up to -0.72 GPa), composition-independent electrical resistivity (around 13×10^{-7} Ωm) and gradually decreasing hardness (from 12.1 to 4.7 GPa) due to reducing average bond energy.

Further addition of Zr (≥ 86 at.%) led to a gradual vanishing of the amorphous W–Zr phase (86 – 88 at.% Zr) and to the formation of Zr-rich films with a predominantly dual-phase crystalline structure exhibiting a gradual transition from a metastable β-Zr(W) solid solution (86 – 96 at.% Zr) through a metastable ω-Zr(W) solid solution (94 – 100 at.% Zr) to the thermodynamically stable α-Zr phase (99 – 100 at.% Zr) with increasing Zr (decreasing W) content. The films with the dominant β-Zr(W) phase were observed to possess a slightly higher hardness, a lower surface roughness and a higher electrical resistivity compared to the films with the dominant ω-Zr(W) or α-Zr phases.

The results obtained indicate that supersaturated solid solutions, metallic glasses, high-temperature or high-pressure phases and their mutual mixtures can be prepared in magnetron sputtered W–Zr films. A crucial issue is also their thermal stability and oxidation resistance, which is a subject of our ongoing study.

Acknowledgments

The authors wish to thank Assoc. Prof. Š. Kos and Assoc. Prof. J. Houška for valuable comments and suggestions.

Reference

[1] C.Y. Chuang, J.W. Lee, C.L. Li, J.P. Chu, Mechanical properties study of a magnetron-sputtered Zr-based thin film metallic glass, Surf. Coatings Technol. 215 (2013) 312–321. doi:10.1016/j.surfcoat.2012.04.101.

[2] C.Y. Chuang, Y.C. Liao, J.W. Lee, C.L. Li, J.P. Chu, J.G. Duh, Electrochemical characterization of Zr-based thin film metallic glass in hydrochloric aqueous solution, Thin Solid Films. 529 (2013) 338–341. doi:10.1016/j.tsf.2012.03.065.

[3] Y.L. Deng, J.W. Lee, B.S. Lou, J.G. Duh, J.P. Chu, J.S.C. Jang, The fabrication and property evaluation of Zr-Ti-B-Si thin film metallic glass materials, Surf. Coatings Technol. 259 (2014) 115–122. doi:10.1016/j.surfcoat.2014.03.026.

[4] H. Chen, G. Zhang, J. Chen, X. Yin, Fracture filling fluids identification using azimuthally elastic impedance based on rock physics, J. Appl. Geophys. 110 (2014) 98–105. doi:10.1016/j.jappgeo.2014.09.006.

[5] J.P. Chu, T.Y. Liu, C.L. Li, C.H. Wang, J.S.C. Jang, M.J. Chen, S.H. Chang, W.C. Huang, Fabrication and characterizations of thin film metallic glasses: Antibacterial property and durability study for medical application, Thin Solid Films. 561 (2014) 102–107. doi:10.1016/j.tsf.2013.08.111.

[6] H.L. Sun, Z.X. Song, D.G. Guo, F. Ma, K.W. Xu, Microstructure and mechanical properties of nanocrystalline tungsten thin films, J. Mater. Sci. Technol. 26 (2010) 87–92. doi:10.1016/S1005-0302(10)60014-X.

[7] E. Lassner, W.-D. Schubert, Tungsten: properties, chemistry, technology of the element, alloys and chemical compounds, Springer, Boston, MA, 1999. doi:https://doi.org/10.1007/978-1-4615-4907-9.

[8] V. Philipps, Tungsten as material for plasma-facing components in fusion devices, J. Nucl. Mater. 415 (2011) S2. doi:10.1016/j.jnucmat.2011.01.110.

[9] S.K. Sikka, Y.K. Vohra, R. Chidambaram, Omega phase in materials, Prog. Mater. Sci. 27 (1982) 245–310. doi:10.1016/0079-6425(82)90002-0.

[10] J. Zhang, Y. Zhao, C. Pantea, J. Qian, L.L. Daemen, P.A. Rigg, R.S. Hixson, C.W. Greeff, G.T. Gray, Y. Yang, L. Wang, Y. Wang, T. Uchida, Experimental constraints on the phase diagram of elemental zirconium, J. Phys. Chem. Solids. 66 (2005) 1213–1219. doi:10.1016/j.jpcs.2005.03.004.

[11] B.S. Hickman, The formation of omega phase in titanium and zirconium alloys: A review, J. Mater. Sci. 4 (1969) 554–563. doi:10.1007/BF00550217.

[12] H. Xia, A.L. Ruoff, Y.K. Vohra, Temperature dependence of the -bcc phase transition in zirconium metal, Phys. Rev. B. 44 (1991) 10374–10376.

doi:10.1103/PhysRevB.44.10374.

[13] J.C. Jamieson, C. Olinger., Zirconium: phases and compressibility to 120 kilobars, High Temp. Press. 5 (1973) 123–131. https://htracyhall.org/ocr/HTH-Archives/Cabinet 8/Drawer 4 (MP-OL)/(Olinger, B.) (Oliver, B.G.) (Oliver, M.R.) (linked)/(Olinger, B.) (Oliver, B.G.) (Oliver, M.R.)-133_OCR.pdf.

[14] J. Liu, K. Barmak, Topologically close-packed phases: Deposition and formation mechanism of metastable β-W in thin films, Acta Mater. 104 (2016) 223–227. doi:10.1016/j.actamat.2015.11.049.

[15] F.T.N. Vüllers, R. Spolenak, Alpha- vs. beta-W nanocrystalline thin films: A comprehensive study of sputter parameters and resulting materials' properties, Thin Solid Films. 577 (2015) 26–34. doi:10.1016/j.tsf.2015.01.030.

[16] M.J. O'Keefe, J.T. Grant, Phase transformation of sputter deposited tungsten thin films with A-15 structure, J. Appl. Phys. 79 (1996) 9134–9141. doi:10.1063/1.362584.

[17] H. Okamoto, M.E. Schlesinger, E.. Mueller, eds., ASM Handbook: Alloy Phase Diagrams, ASM International, 2016. doi:10.31399/asm.hb.v03.a0006217.

[18] R.F. Domagala, D.J. McPherson, M. Hansen, Systems Zirconium-Molybdenum and Zirconium-Wolfram, JOM. 5 (1953) 73–79. doi:10.1007/BF03397454.

[19] H. Ren, X. Liu, J. Ning, Microstructure and mechanical properties of W-Zr reactive materials, Mater. Sci. Eng. A. 660 (2016) 205–212. doi:10.1016/j.msea.2016.02.009.

[20] Z. Cui, X. Zhang, Q. Liu, H. Li, Y. Liu, H. Liu, X. Wang, J. Huang, H. Liu, J. Cheng, M. Li, S. Geng, Y. Xu, C. Tang, G. Lei, A first-principles study of the mechanical and thermodynamic properties of WTi, WV, W2Zr, WVTi, WVZr alloys, Fusion Eng. Des. 152 (2020) 111451. doi:10.1016/j.fusengdes.2019.111451.

[21] J. Bhattarai, E. Akiyama, H. Habazaki, A. Kawashima, K. Asami, K. Hashimoto, Electrochemical and xps studies of the corrosion behavior of sputter-deposited amorphous W-Zr alloys in 6 and 12 M HCl solutions, Corros. Sci. 39 (1997) 355–375. doi:10.1016/S0010-938X(97)83351-3.

[22] D. Horwat, E. Jimenez-Pique, J.F. Pierson, S. Migot, M. Dehmas, M. Anglada, High hardness, low Youngs modulus and low friction of nanocrystalline ZrW 2 Laves phase and Zr 1-xW x thin films, J. Phys. Chem. Solids. 73 (2012) 554–558. doi:10.1016/j.jpcs.2011.12.009.

[23] D. Horwat, M. Dehmas, E. Aubry, J. Zollinger, S. Migot, J.F. Pierson, Properties of nanocrystalline and nanocomposite WxZr1-x thin films deposited by co-sputtering, Intermetallics. 17 (2009) 421–426. doi:10.1016/j.intermet.2008.11.020.

[24] P. Zeman, M. Zítek, Zuzjaková, R. Čerstvý, Amorphous Zr-Cu thin-film alloys with metallic glass behavior, J. Alloys Compd. (2017). doi:10.1016/j.jallcom.2016.12.098.

[25] M. Zítek, P. Zeman, Š. Zuzjaková, M. Kotrlová, R. Čerstvý, Tuning properties and behavior of magnetron sputtered Zr-Hf-Cu metallic glasses, J. Alloys Compd. 739 (2018). doi:10.1016/j.jallcom.2017.12.301.

[26] J. Musil, M. Jaroš, Š. Kos, Superhard metallic coatings, Mater. Lett. 247 (2019) 32–35. doi:10.1016/j.matlet.2019.03.086.

[27] J. Musil, Kos, S. Zenkin, Z. Čiperová, D. Javdošňák, R. Čerstvý, β- (Me1, Me2) and

MeNx films deposited by magnetron sputtering: Novel heterostructural alloy and compound films, Surf. Coatings Technol. 337 (2018) 75–81. doi:10.1016/j.surfcoat.2017.12.057.

[28] A.J. Perry, V. Valvoda, D. Rafaja, X-ray residual stress measurement in TiN, ZrN and HfN films using the Seemann-Bohlin method, Thin Solid Films. 214 (1992) 169–174. doi:10.1016/0040-6090(92)90766-5.

[29] D. Rafaja, M. Dopita, M. Růžička, V. Klemm, D. Heger, G. Schreiber, M. Šíma, Microstructure development in Cr-Al-Si-N nanocomposites deposited by cathodic arc evaporation, Surf. Coatings Technol. 201 (2006) 2835–2843. doi:10.1016/j.surfcoat.2006.05.033.

[30] E. Grünwald, R. Nuster, R. Treml, D. Kiener, G. Paltauf, R. Brunner, Young's Modulus and Poisson's Ratio Characterization of Tungsten Thin Films Via Laser Ultrasound, Mater. Today Proc. 2 (2015) 4289–4294. doi:10.1016/j.matpr.2015.09.015.

[31] P.F. Weck, E. Kim, V. Tikare, J.A. Mitchell, Mechanical properties of zirconium alloys and zirconium hydrides predicted from density functional perturbation theory, Dalt. Trans. 44 (2015) 18769–18779. doi:10.1039/c5dt03403e.

[32] A.R. Denton, N.W. Ashcroft, Vegard's law, Phys. Rev. A. 43 (1991) 3161–3164. doi:10.1103/PhysRevA.43.3161.

[33] C.O. Kim, W.L. Johnsin, Amorphous phase separation in the metallic glasses (Pb1−ySby)1−xAux, Phys. Rev. B. 23 (1981) 143–147. doi:10.1103/PhysRevB.23.143.

[34] G.K. Williamson, W.H. Hall, X-ray line broadening from filed aluminium and wolfram, Acta Metall. 1 (1953) 22–31. doi:10.1016/0001-6160(53)90006-6.

[35] W.H. Hall, X-Ray Line Broadening in Metals, Proc. Phys. Soc. A. 62 (1949) 741.

[36] P. Zeman, S. Haviar, M. Cervena, Self-formation of dual glassy-crystalline structure in magnetron sputtered W – Zr films, 187 (2021). doi:10.1016/j.vacuum.2021.110099.

[37] Y.J. Hu, M.R. Fellinger, B.G. Bulter, Y. Wang, K.A. Darling, L.J. Kecskes, D.R. Trinkle, Z.K. Liu, Solute-induced solid-solution softening and hardening in bcc tungsten, Acta Mater. 141 (2017) 304–316. doi:10.1016/j.actamat.2017.09.019.

D

Self-formation of dual glassy-crystalline structure in magnetron sputtered W–Zr films

P. Zeman, S. Haviar, M. Červená

Vacuum 187 (2021) 110099

Vacuum 187 (2021) 110099

Contents lists available at ScienceDirect

Vacuum

journal homepage: http://www.elsevier.com/locate/vacuum

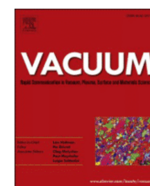

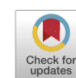

Self-formation of dual glassy-crystalline structure in magnetron sputtered W–Zr films

P. Zeman *, S. Haviar, M. Červená

Department of Physics and NTIS - European Centre of Excellence, University of West Bohemia, Univerzitní 8, 306 14, Plzeň, Czech Republic

ARTICLE INFO

Keywords:
W–Zr
Dual structure
Metallic glass
Thin films
Magnetron sputtering

ABSTRACT

Self-formation of a unique dual glassy-crystalline structure in binary W–Zr system was observed for a film with 28 at.% Zr prepared by magnetron co-sputtering. The film is composed of conical columnar domains of α-W(Zr) solid solution structure surrounded by featureless areas corresponding to a W–Zr metallic glass. The conical domains have their axes perpendicular to the film surface. Most of the domains have the apex at or close to the substrate surface, which corresponds to the point of primary nucleation. The surface ratio of glassy and crystalline phase (bases of the cones) is dependent on the film thickness. The dual structure is prepared in a very narrow window of the elemental composition. We suppose that the specific elemental composition and the diffusivity or mobility of sputtered adatoms are crucial for the self-formation of the dual structure.

In the last decade, physical vapor deposition methods such as magnetron sputtering have been demonstrated to be suitable deposition techniques for preparing metallic glasses with exceptional physical and functional properties in the form of thin films (TFMGs) [1,2]. Thanks to non-equilibrium conditions of the glow discharge plasma and very high cooling rates (higher than 10^6 K/s) on atomic scale at the substrate, TFMGs can be prepared in a much wider composition variety and solubility than bulk metallic glasses (BMGs) that have been most prepared by rapid casting processes based on melt quenching [3,4]. Moreover, TFMGs have showed properties and characteristics that are superior to BMGs, and metallic and ceramic coatings. While BMGs suffer from a lack of plasticity due to shear banding phenomena occurring during deformation [5,6], TFMGs show an improved plasticity and fatigue resistance due to the size effect [7,8]. In contrast to ductile metallic and brittle ceramic coatings, TFMGs have a better balance of ductility and strength [9].

Recently, attention has also been drawn to prepare dual-phase alloys comprising both glassy/amorphous and nanocrystalline metallic phases with aim to overcome drawbacks of each component and further enhance properties of the resultant material such as thermal stability, ductility, and fracture toughness. Commonly used fabrication routes encompass two-step processes of controlled annealing- or deformation-induced nanocrystallization of metallic glasses and controlled solid-state amorphization of crystalline materials. A challenging route is, however, a direct one-step process allowing for a controlled in-situ formation of the dual-phase material. A few successful results have been achieved for magnetron sputtered deposits in Al–Mo [10], Cu–Zr [11], Ni–Zr [12,13] and Mg–Cu–Y [14] systems and electrodeposits in Al–Mn [15] and Ni–W [16] systems. The structure of all these deposited materials consists of homogenously dispersed nanocrystallites in an amorphous matrix.

A very specific heterogenous dual-phase structure has been reported very recently in magnetron sputtered Ti–Al [17], Zr–Mo [18] and Zr–W [19] thin-film alloys. Independently of these works, we observed the same type of the film structure during non-reactive magnetron co-sputtering of W and Zr targets. The present short communication therefore reports on the self-formation of this unique dual glassy-crystalline structure consisting of submicrometer-sized conical columnar crystalline domains of α-W(Zr) solid solution surrounded by a W–Zr metallic glass. The aim of the paper is to provide conditions of the formation and to characterize features of the unique structure in detail. Much more extensive study focusing on systematic investigation of W–Zr thin-film alloys in a very wide composition range is, however, still ongoing.

Approximately 2 μm thick W–Zr films were deposited onto polished and ultrasonically pre-cleaned Si(100) or Si(111) substrate without external heating and voltage biasing in a magnetron sputter system (AJA International ATC 2200-V). The substrates were rotating (40 rpm) at a distance of 150 mm above two circular unbalanced magnetrons equipped with a W target (2" diameter, 99.95% purity) and a Zr target (2"

* Corresponding author.
E-mail address: zemanp@kfy.zcu.cz (P. Zeman).

https://doi.org/10.1016/j.vacuum.2021.110099
Received 18 November 2020; Received in revised form 15 January 2021; Accepted 24 January 2021
Available online 3 February 2021
0042-207X/© 2021 Published by Elsevier Ltd.

diameter, 99.7% purity), each of them connected to a dc power supply. Before introducing argon (99.999% purity) as a sputtering gas (0.53 Pa), a cylindrical stainless steel deposition chamber was pumped down to 5 $\times 10^{-5}$ Pa by a turbomolecular pump. A W/Zr concentration ratio in the films was controlled by setting a ratio of the deposition rates from individual targets according to molar volumes of W and Zr atoms. The rates were measured by a quartz crystal deposition rate monitor and adjusted by controlling the dc target powers. The thickness of the films was controlled by adjusting the deposition time.

The elemental composition of the films was analyzed in a scanning electron microscope (SU-70, Hitachi) operated at a primary electron energy of 20 keV using energy dispersive spectroscopy (EDS, UltraDry, Thermo Scientific). W and Zr standards were used for the quantitative analysis. The accuracy of the elemental analysis was established to be 1 at.%. The same electron microscope was used for imaging of the surface of as-deposited films as well as their cross-sectional views. The cross sections were prepared by simple breaking of the pre-scratched substrate. This was done upon cooling in liquid nitrogen and at ambient temperature.

The structure of the films was measured by X-ray diffraction (XRD) using a diffractometer (X'Pert PRO, PANalytical) working with Cu K_α radiation ($\lambda_{Cu} = 0.154187$ nm) at a glancing incidence of 2°. The film thickness was measured by a surface profilometer (Dektak 8 Stylus Profiler, Veeco). The surface topography and arithmetic average surface roughness of the films was measured in semi-contact mode of an atomic force microscope (AFM, SmartSPM, AIST-NT) equipped with a silicon tip (nominal radius < 10 nm).

Fig. 1 shows XRD patterns of three W–Zr films of a different elemental composition and structure prepared at a different combination of the target powers P_W and P_{Zr}. The most interesting film contains 28 at.% Zr, which corresponds to $P_W = 260$ W and $P_{Zr} = 214$ W. Its XRD pattern (Fig. 1b) is characterized with a superposition of an amorphous hump and a high-intensity diffraction peak at a 2θ position of about 39°, and other diffraction peaks at higher 2θ angles. All diffraction peaks correspond to the bcc structure of α-W but they are shifted to lower 2θ angles compared to a powder diffraction standard (PDF Card No. 004–0806). This is because larger Zr atoms (155 p.m.) substitutes smaller W atoms (135 p.m.) in the bcc lattice and thus an α-W(Zr) solid solution is formed. In addition, the amorphous hump is an indication that the film is not crystalline completely, but it contains an amorphous phase as well. This was corroborated by SEM imaging of the surface morphology as shown also in Fig. 1. It is visible that a large number of microscopic domains of a nearly ideally circular shape are observed on the surface of the film. These are of different size but most of them are approximately 4 μm in diameter. They touch each other in most cases but some of them are separated by featureless areas. That is, a dual structure with a crystalline and amorphous phase is formed in this film in contrast to other two films.

The film prepared at $P_W = 260$ W and $P_{Zr} = 165$ W (Fig. 1a) contains 24 at.% Zr and exhibits a highly crystalline structure corresponding to an α-W(Zr) solid solution. The shift of all diffraction peaks to lower 2θ angles compared to the powder diffraction standard is smaller than for the film with the dual structure due to a lower Zr content in this film. Its surface morphology is uniform without a presence of featureless area. On the other hand, the film prepared at $P_W = 254$ W and $P_{Zr} = 260$ W (Fig. 1c) is X-ray amorphous and contains 33 at.% Zr. Its surface is very smooth without an appearance of any crystalline domains. This is because the single-phase α-W(Zr) solid solution structure becomes thermodynamically unfavorable with gradually increasing Zr content and the self-formation of the dual structure is limited only to a relatively narrow composition window.

The dual structure was further imaged by SEM and analyzed. Surface and cross-sectional micrographs at higher magnifications are shown in Fig. 2. As visible in Fig. 2a and b, the internal structure of the circular crystalline domains consists of submicrometer-sized oval grains resembling hard shell clams. Their size is the largest in the center of the circle domains and gradually decreases towards the edge. The area surface roughness inside the domains measured by AFM has a value of around 12.2 nm, while that of the featureless areas is only around 0.2 nm. Such a low value of the surface roughness is typical for amorphous or glassy surfaces, as we have observed for ZrCu-based TFMGs [20–22]. It corresponds to the value of the film with 33 at.% Zr and the X-ray

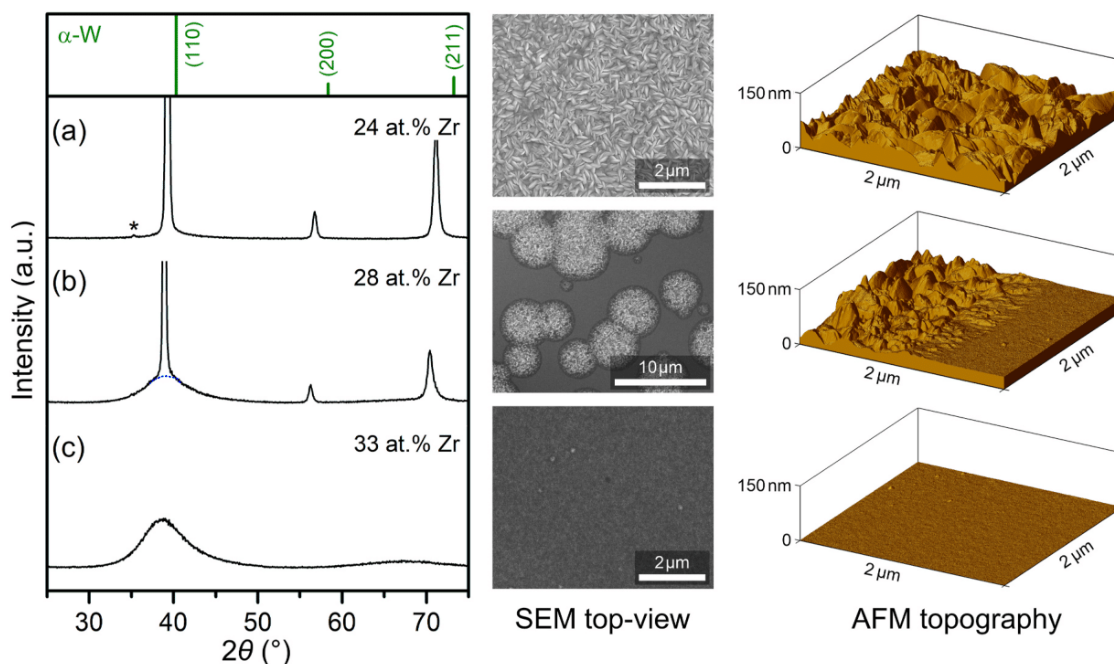

Fig. 1. XRD patterns, SEM top-view micrographs and AFM topography images of W–Zr films with 24, 28 and 33 at.% Zr. The film with 28 at.% Zr is characterized with a dual glassy-crystalline structure. A very low-intensity diffraction peak marked by asterisk in Fig. 1a originates from the diffraction of (110) crystallographic planes for Cu K_β radiation.

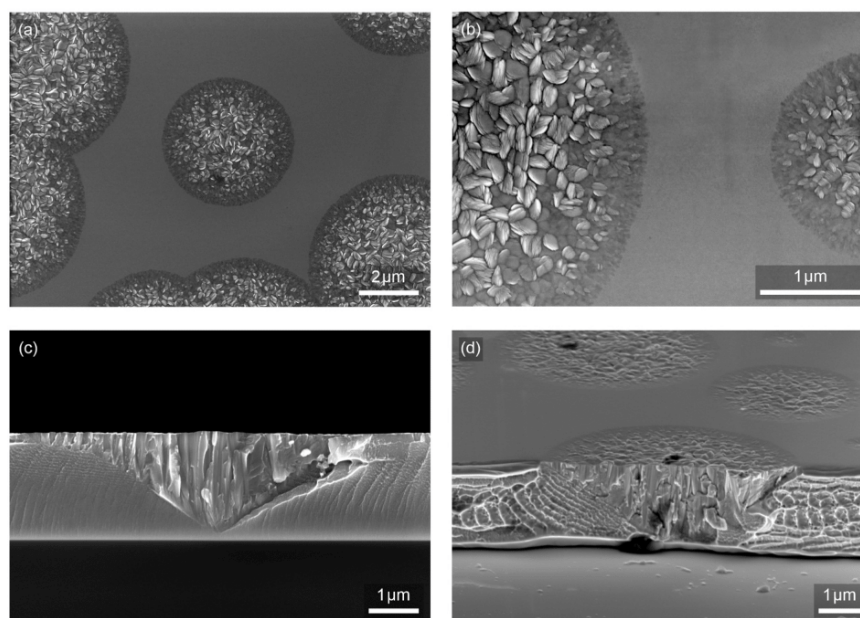

Fig. 2. SEM micrographs of the surface (a)+(b) and cross section (c)+(d) of W–Zr film with 28 at.% Zr and a dual glassy-crystalline structure. The film shown in (c) was broken in liquid nitrogen while the film in (d) at ambinet conditions.

amorphous structure (Fig. 1c). On the other hand, the surface morphology of the circular domains is similar to that corresponding to the fully crystalline film with 24 at.% Zr.

Fig. 2c and d shows cross-sectional micrographs of the film on the Si (100) substrates. It is seen that the circular domains observed on the surface are the bases of cones that come up from the volume of the film, often from the film/substrate interface. The axes of these cones are perpendicular to the substrate surface. The microstructure is columnar without remarkable voids between the columns. Most of the columns are straight from their origin up to the surface but some of them are also of V-shape characteristic for the competitive crystallographic growth. That is, the internal microstructure of the crystalline cones corresponds to the boundary between zone I and T according to the structure zone model [23]. The submicrometer-sized oval grains observed on the surface inside the cone bases are terminations of the columns. The surroundings of the crystalline cones are of a featureless morphology as typical for an amorphous structure. If the film deposited on the Si(100) substrate is not fractured in liquid nitrogen (Fig. 2c) but at ambient conditions (a tilted cross-section image in Fig. 2d), the fracture surface of the amorphous area contains typical rupture characteristics of metallic glasses such as vein-like patterns and micro-scale striations [24,25]. These features are a consequence of inhomogeneous plastic deformation with strain localized in shear bands [26,27]. This observation provides evidence that the amorphous phase is a metallic glass.

The conical shape of the crystalline domains suggests that primary nucleation is initiated at the point corresponding to the apex of the cone. Subsequently, a crystalline cell and then island of the W(Zr) solid solution is evolved from the primary nucleus. As the deposition continues, sputtered adatoms form a new adlayer. When atoms are incident on the underlying crystalline island, they contribute to its columnar growth. The atoms incident on or diffusing to the edge of the crystalline island participate in nucleation and formation of a new column, as visible at the interface between the crystalline and amorphous phase in Fig. 2c. Let us note that the deposition is done without any additional substrate heating and bias, therefore the mobility of adatoms is quite limited and the nucleation and crystal growth are mainly governed by kinetics. Since the crystalline domains grow in diameter evenly and nearly ideal circular discs are formed in each adlayer, the nucleation and crystal growth are considered to be isotropic. As a result, the conical shape of the crystalline columnar domains is evolved in the volume of the film during its growth.

The bases of the cones are projected to circular domains at surface. Therefore, the surface ratio of the glassy-to-crystalline phase is dependent on the film thickness. The larger the thickness is, the higher the ratio is. For a specific thickness, the surface of the film will be completely covered by the crystalline phase. The elemental composition of the crystalline and amorphous phase is the same provided that the arrival flux of deposited W and Zr atoms will be constant during the whole deposition. This was verified by the measurement of the EDS profile on an ion-polished specimen over the interface of both phases (not shown).

The depth, where the primary nucleation occurs, is decisive for the final diameter of the crystalline domains observed at the surface. The deeper the nucleation initiates in the film, the wider the domain is at the surface. This effect can be studied statistically simply by monitoring the diameter of the circular domains at the surface. A histogram in Fig. 3 shows a concentration of the domains in respect to their diameter counted from twenty SEM micrographs (125×88 μm^2 each) covering an area of 0.22 mm^2 in total. The key information is that the histogram has a relatively sharp upper limit (approx. 4.4 μm), which confirms that there cannot be bigger cones than those growing from the substrate surface. It can be also easily recognized that most of the conical domains grow directly from or close to the substrate surface. That is, the probability of the formation of a stable nucleus of the critical size is much higher on the surface of the Si substrates (otherwise the histogram would be rectangular). This can be explained by a higher diffusivity of the deposited adatoms on the clean, nearly atomically flat, surface of the Si substrates contrary to newly formed adlayers of the metallic film with a higher probability of binding.

Fig. 3 also shows a comparison of histograms corresponding to the growth of the film on the Si(100) and Si(111) substrates. Despite both histograms have a similar diameter distribution of the crystalline domains, their concentrations are lower for the Si(111) substrate for all cases. We attribute this behavior to different diffusivities of W and Zr adatoms on the Si(111) surface compared to the Si(100) one. To initiate the nucleation of the crystalline domains, W and Zr adatoms with an

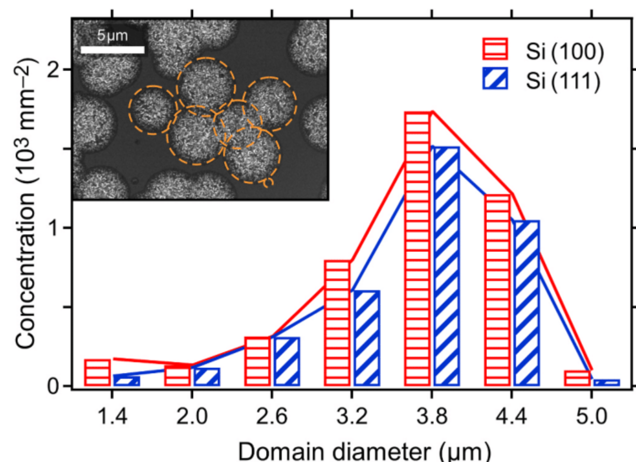

Fig. 3. Histograms representing a concentration of crystalline domains in respect to their diameter counted from twenty SEM micrographs (125 × 88 μm^2 each) covering an area of 0.22 mm^2 in total. A comparison of histograms corresponding to the growth of the film on the Si(100) and Si(111) substrates is shown.

appropriate local composition ratio must encounter in a reasonable time. The probability of the nucleation is then dependent on the diffusivities of single atoms on the surface. It seems that this probability is lower for the Si(111) surface compared to the Si(100) one. For instance, the role of different diffusion coefficients on silicon surfaces was demonstrated for Pb and Ge atoms [28,29].

In summary, we showed that a dual glassy-crystalline structure can be formed in W–Zr films with 28 at.% Zr. The preparation of the dual structure is very reproducible but very sensitive to the elemental composition. The crystalline structure corresponds to α-W(Zr) solid solution growing in columnar domains of a conical shape oriented with the axes perpendicular to the film surface. The amorphous surrounding of the conical domains exhibits features corresponding to a metallic glass. The glassy-to-crystalline structure ratio on the surface can be controlled by both the film thickness and a fine variation of the elemental composition. This may provide a possibility to tune surface-sensitive properties of W–Zr films.

Declaration of competing interest

The authors declare that they have no known competing financial interests or personal relationships that could have appeared to influence the work reported in this paper.

This work was supported by the project LO1506 of the Czech Ministry of Education, Youth and Sports under the program NPU I. The authors thank Assoc. Prof. J. Houška for a valuable discussion, Dr. R. Čerstvý for XRD measurements and Dr. Rezek for AFM measurements.

References

[1] J.P. Chu, J.S.C. Jang, J.C. Huang, H.S. Chou, et al., Thin Solid Films 520 (2012) 5097.
[2] W. Diyatmika, J.P. Chu, B.T. Kacha, et al., Curr. Opin. Solid State Mater. Sci. 19 (2015) 95.
[3] M.F. Ashby, A.L. Greer, Scripta Mater. 54 (2006) 321.
[4] J. Schroers, G. Kumar, T.M. Hodges, S. Chan, T.R. Kyriakides, J. Miner. Met. Mater. 61 (2009) 21.
[5] L.A. Davis, Metall. Trans. A 10A (1979) 235.
[6] A.L. Greer, Y.Q. Cheng, E. Ma, Mater. Sci. Eng. R Rep. 74 (2013) 71.
[7] J.C. Ye, J.P. Chu, Y.C. Chen, Q. Wang, Y. Yang, J. Appl. Phys. 112 (2012), 053516.
[8] M. Ghidelli, H. Idrissi, S. Gravier, J.-J. Blandin, J.-P. Raskin, et al., Acta Mater. 131 (2017) 246.
[9] H.L. Jia, F.X. Liu, Z. An, W.D. Li, G.Y. Wang, J.P. Chu, et al., Thin Solid Films 561 (2014) 2.
[10] C. Ophus, E. Luber, M. Edelen, Z. Lee, L. Fischer, S. Evoy, D. Lewis, U. Dahmen, V. Radmilovic, D. Mitlin, Acta Mater. 57 (2009) 4296.
[11] P. Zhang, J.Y. Zhang, J. Li, G. Liu, K. Wu, Y.Q. Wang, J. Sun, Acta Mater. 76 (2014) 221.
[12] B. Prasad Sahu, C. Kumar Sarangi, R. Mitra, Thin Solid Films 660 (2018) 31.
[13] B. Prasad Sahu, A. Dutta, R. Mitra, J. Mater. Res. 35 (2020) 1543.
[14] G. Wu, K.-C. Chan, L. Zhu, L. Sun, J. Lu, Nature 545 (2017) 80.
[15] S. Ruan, C.A. Schuh, Acta Mater. 57 (2009) 3810.
[16] H. Cesiulis, A. Baltutiene, M. Donten, Z. Stojek, J. Solid State Electrochem. 6 (2002) 237.
[17] Vl Kolkovsky, J.-U. Schnidt, S. Doering, Thin Solid Films 669 (2020) 169.
[18] A. Borroto, S. Bruyere, S. Migot, J.-F. Pierson, T. Gries, F. Muecklich, D. Horwat, Acta Mater. 181 (2019) 78.
[19] A. Borroto, A.C. García-Wong, S. Bruyere, S. Migot, D. Pilloud, J.-F. Pierson, F. Muecklich, D. Horwat, Appl. Surf. Sci. 538 (2021) 148133.
[20] P. Zeman, M. Zítek, Š. Zuzjaková, R. Čerstvý, J. Alloys Compd. 696 (2017) 1298–1306.
[21] M. Zítek, P. Zeman, Š. Zuzjaková, M. Kotrlová, R. Čerstvý, J. Alloys Compd. 739 (2018) 848–855.
[22] M. Zítek, P. Zeman, M. Kotrlová, R. Čerstvý, J. Alloys Compd. 772 (2019) 409–417.
[23] S. Mahieu, P. Ghekiere, D. Depla, R. De Gryse, Thin Solid Films 515 (2006) 1229.
[24] F.H. Dalla Torre, A. Dubach, J. Schällibaum, J.F. Löffler, Acta Mater. 56 (2008) 4635.
[25] B.A. Sun, W.H. Wang, Prog. Mater. Sci. 74 (2015) 211.
[26] C.A. Schuh, T.C. Hufnagel, U. Ramamurty, Acta Mater. 55 (2007) 4067.
[27] S.X. Song, T.G. Nieh, Intermetallics 19 (2011) 1968.
[28] A.E. Dolbak, R.A. Zhachuk, B.Z. Olshanetsky, Cent. Eur. J. Phys. 2 (2004) 254.
[29] A.E. Dolbak, B.Z. Olshanetsky, Cent. Eur. J. Phys. 4 (2006) 310.

E

Enhancement of high-temperature oxidation resistance and thermal stability of hard and optically transparent Hf–B–Si–C–N films by Y or Ho addition

M. Kotrlová, P. Zeman, J. Houška, V. Šímová, M. Procházka, R. Čerstvý, S. Haviar, J. Vlček

Journal of Non-Crystalline solids 553 (2021) 120470

Journal of Non-Crystalline Solids 553 (2021) 120470

Contents lists available at ScienceDirect

Journal of Non-Crystalline Solids

journal homepage: www.elsevier.com/locate/jnoncrysol

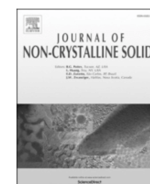

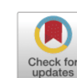

Enhancement of high-temperature oxidation resistance and thermal stability of hard and optically transparent Hf–B–Si–C–N films by Y or Ho addition

M. Kotrlová, P. Zeman *, J. Houška, V. Šímová, M. Procházka, R. Čerstvý, S. Haviar, J. Vlček

Department of Physics and NTIS - European Centre of Excellence, University of West Bohemia, Univerzitní 8, 306 14 Plzeň, Czech Republic

A R T I C L E I N F O

Keywords:
Hf–B–Si(–Y/Ho)–C–N
Oxidation resistance
Thermal stability
Hardness
Optical properties

A B S T R A C T

Hard and optically transparent amorphous $Hf_7B_{10}Si_{32}C_2N_{44}$, $Hf_6B_{12}Si_{29}Y_2C_2N_{45}$ and $Hf_5B_{13}Si_{25}Ho_3C_2N_{48}$ films were prepared and examined for the oxidation resistance in air and thermal stability in inert gasses up to 1600 °C. A thermal evolution of their structure, hardness and optical properties was also studied. An addition of Y or Ho (2–3 at.%) into Hf–B–Si–C–N films leads to a stabilization of tetragonal HfO_2 in a surface oxide layer upon oxidation. The thickness of this layer is the lowest for the Y addition. Upon annealing in He, no mass changes are detected up to 1315 °C and this temperature is shifted even to 1350 °C for the $Hf_6B_{12}Si_{29}Y_2C_2N_{45}$ film. The hardness of this film is enhanced from 22.2 GPa in the as-deposited state to 25.9 GPa after annealing to 1300 °C and the film retains its optical transparency up to 1400 °C. The crystallization of the amorphous structure occurs at around 1400 °C.

1. Introduction

In the last decade, HfB_2-based ultra-high temperature ceramics have been in the center of attention due to an interesting combination of properties such as high melting point, high hardness, high thermal stability and high oxidation resistance [1–8]. These properties make them appropriate candidates for high-temperature applications at temperatures significantly exceeding 1000 °C [9]. Recently, we have also shown that non-oxide ceramic coatings from the quinary Hf–B–Si–C–N system can be promising candidates for high-temperature protection of optical and optoelectronic devices or for applications in the field of capacitive sensors used in severe oxidation environment [10–12].

In our previous paper [13], we specifically investigated the high-temperature behavior of an electrically conductive $Hf_7B_{23}Si_{22}C_6N_{40}$ and an optically transparent $Hf_6B_{21}Si_{19}C_4N_{47}$ film annealed in synthetic air up to 1500 °C. We focused especially on the evolution of the microstructure upon annealing, oxidation resistance and the effect of nitrogen incorporation. Both of these films exhibited exceptional oxidation resistance with very small mass changes up to 1500 °C, which was caused by a formation of a nanocomposite oxide surface layer upon annealing serving as an efficient protective diffusion barrier. This layer consisted of m-HfO_2 and o-HfO_2 or t-HfO_2 nanocrystallites surrounded by a SiO_2-based amorphous matrix. While the film with the higher nitrogen content remained amorphous underneath the oxide layer upon annealing to 1500 °C, the film with the lower content of nitrogen was partially crystallized. Both films, however, exhibited very high thermal stability of the elemental composition up to 1600 °C.

Recently, it has been also reported that mono- and disilicates of rare-earth elements, such as Y, Yb, Ho etc., can form a more stable protective barrier layer than pure silica in hot sections of gas turbine engines [14–19]. While silica undergoes recession when reacting with high-temperature steam, the silicates limit this reaction. In addition, the monosilicates were revealed to be more stable in such a high-temperature, high-pressure harsh environment than the corresponding disilicates.

In the present paper, we investigate the effect of an addition of small amount (2 – 3 at.%) of Y or Ho into Hf–B–Si–C–N films in order to prepare hard and optically transparent protective films with the thermal stability significantly exceeding 1000 °C. The films were prepared by reactive dc pulsed magnetron co-sputtering of Hf, Si, B, C and Y or Ho from a single target in an argon-nitrogen mixture.

We examine in detail the high-temperature oxidation resistance and the thermal stability of the structure, hardness and optical properties of

* Corresponding author.
E-mail address: zemanp@kfy.zcu.cz (P. Zeman).

https://doi.org/10.1016/j.jnoncrysol.2020.120470
Received 29 May 2020; Received in revised form 25 September 2020; Accepted 8 October 2020
Available online 21 October 2020
0022-3093/© 2020 Elsevier B.V. All rights reserved.

the films upon annealing in air and inert gasses (argon or helium) up to 1500 °C and 1600 °C, respectively. We pay particular attention to the evolution of the structure, hardness, extinction coefficient and refractive index of the films with increasing annealing temperature.

2. Experimental

Hf–B–Si(–Y/Ho)–C–N films were deposited by reactive pulsed dc magnetron co-sputtering of a target (127 × 254 mm^2) consisting of a B_4C plate overlapped by Hf, Si and Y or Ho stripes with the fixed 15% Hf + 50% Si + 5% Hf/Y/Ho fractions in the target erosion area. The magnetron was driven by a pulsed dc Rübig MP 120 power supply operating at a repetition frequency of 10 kHz and an average target power of 500 W in a period with a fixed 50 μs negative-voltage pulse length and short-lived high positive voltage overshoots (higher than 200 V, as shown and discussed in [10]). The base pressure before each deposition was lower than 1×10^{-3} Pa. The total pressure of an argon-nitrogen mixture used for the depositions was 0.5 Pa with a nitrogen fraction of 25%. The films were deposited onto Si(100), 6H-SiC and Cu substrates. The SiC substrate was used for annealing experiments above 1300 °C (to avoid melting of the Si substrate) and the Cu substrate for DSC analysis. No significant effect of the substrate type on the structure and the properties of the films was observed. The target-to-substrate distance was set to 100 mm. The substrates were held at a floating potential and the substrate temperature was 450 °C.

The thickness of the films was measured by a Veeco Dektak 8 Stylus profilometer with a vertical resolution of 0.75 nm. The hardness of the as-deposited and annealed films was measured by an ultramicroindenter Fischerscope H100 with a maximum load of 20 mN. The measurement error was calculated by using the WIN—HCU software using the Student's distribution with 95% probability.

The electrical resistivity of the films was measured at room temperature by a standard four-point technique with a 1.047 mm spacing between tips.

The structure of the as-deposited and annealed films on Si and SiC substrates, was measured by X-ray diffraction (XRD) using a PANalytical X'Pert PRO MPD diffractometer working in the modified Bragg–-Brentano geometry with an ω-offset of 1.5° and a CuK_α radiation. The samples were scanned by an ultrafast semiconductor detector X'Celerator over the 2θ-range from 8° to 60° with a scanning speed of 0.036°/s. The structure of the powdered films (mechanically ground) was measured in the standard Bragg–Brentano geometry over the 2θ-range from 8° to 108° with a scanning speed of 0.071°/s.

The elemental composition of the films was determined by the Rutherford backscattering spectrometry (RBS) and the elastic recoil detection (ERD) methods. The contents of Hf, B, Si, Y, Ho, C, N, Zr, O and Ar were measured by RBS, while the content of H by ERD. Regarding the constitutive elements (Hf, B, Si, Y/Ho, C, N), the maximum measurement error is 3 at.%. Regarding other elements detected in the film (Zr as an impurity of the Hf stripes, H, O and Ar), their total content does not exceed 4 at.%.

The mass changes of the Hf–B–Si(–Y/Ho)–C–N films on the SiC substrates during dynamical annealing were measured by thermogravimetry (TG) using a symmetrical high-resolution Setaram TAG 2400 system with an accuracy of ±1 μg. The films with a size of 1 × 1 cm^2 were annealed in air or helium at a flow rate of 1 l/h from room temperature up to 1500 °C or 1400 °C, respectively, at a heating rate of 10 °C/min and cooling rate of 30 °C/min. After annealing in air, the thermogravimetric signal corresponding to oxidation of the uncoated SiC substrate side was subtracted to get the thermogravimetric curves corresponding to the oxidation resistance of Hf–B–Si(–Y/Ho)–C–N films only.

The thermal stability of the structure and its crystallization was also investigated by differential scanning calorimetry (DSC) using a Setaram Labsys DSC 1600 system. For this purpose, Hf–B–Si(–Y/Ho)–C–N films were deposited onto Cu substrates, which were chemically removed after the deposition by using nitric acid. Obtained fragments were then mechanically ground in an agate mortar to provide a fine powder used for the measurements. The powder with the total mass of 5 mg was inserted into a 100 μl alumina crucible covered with a lid. An identical uncharged crucible was used as a reference. The DSC measurements were realized at the same heating and cooling rate of 40 °C/min in argon at a flow rate of 1 l/h in the temperature range from room temperature up to 1600 °C. Each measurement was immediately followed by a second one under the same conditions to obtain a baseline. The calorimeter was calibrated by melting of Pb, Zn and Al standards with purity of 99.998 ± 0.001%.

The refractive index and the extinction coefficient of as-deposited and annealed films and the thickness of the oxide layer formed on the surface of the film after annealing were determined by using a J.A. Woollam Co. variable angle spectroscopic ellipsometer (VASE). The measurements were performed in the wavelength range from 300 to 2000 nm using angles of incidence of 65°, 70° and 75° in reflection. In this paper we discuss values of refractive index and extinction coefficient at a wavelength of 550 nm. The optical data were fitted using the WVASE software. The measurement errors of both optical constants are safely below the presented differences resulting from annealing in He.

The microstructure of the as-deposited and annealed film in cross-section was investigated by a Hitachi SU-70 scanning electron microscope (SEM) using primary energy of electrons of 5 kV. The samples for cross-sectional imaging were produced by breaking the substrate with the as-deposited or annealed film after its cooling down to room temperature.

3. Results and discussion

This section is divided into five subsections. In the first one, the structure and properties of the as-deposited Hf–B–Si(–Y/Ho)–C–N films are introduced. In the second one, results obtained by thermogravimetric measurements in air up to 1500 °C and helium up to 1400 °C are shown in Figs. 1 and 3, respectively. The structure of the films after their annealing in air to 1300 °C and 1500 °C is shown in Fig. 2. In the third subsection, the evolution of hardness and optical properties of the films annealed in helium is presented in Figs. 4 and 5, respectively. The fourth subsection deals with DSC measurements in argon up to 1600 °C. The corresponding DSC curves are depicted in Fig. 6 and the evolution of the structure of the films annealed to 1350–1600 °C is shown in Fig. 7. Finally, cross-sectional SEM micrographs of the as-deposited and annealed films in helium are presented in Fig. 8.

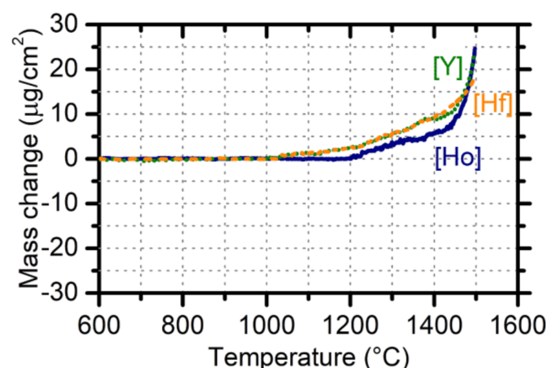

Fig. 1. Thermogravimetric curves of the $Hf_7B_{10}Si_{32}C_2N_{44}$ (orange dashed line), $Hf_6B_{12}Si_{29}Y_2C_2N_{45}$ (green dotted line) and $Hf_5B_{13}Si_{25}Ho_3C_2N_{48}$ (blue solid line) films measured in air at a heating rate of 10 °C/min. (For interpretation of the references to color in this figure legend, the reader is referred to the web version of this article.)

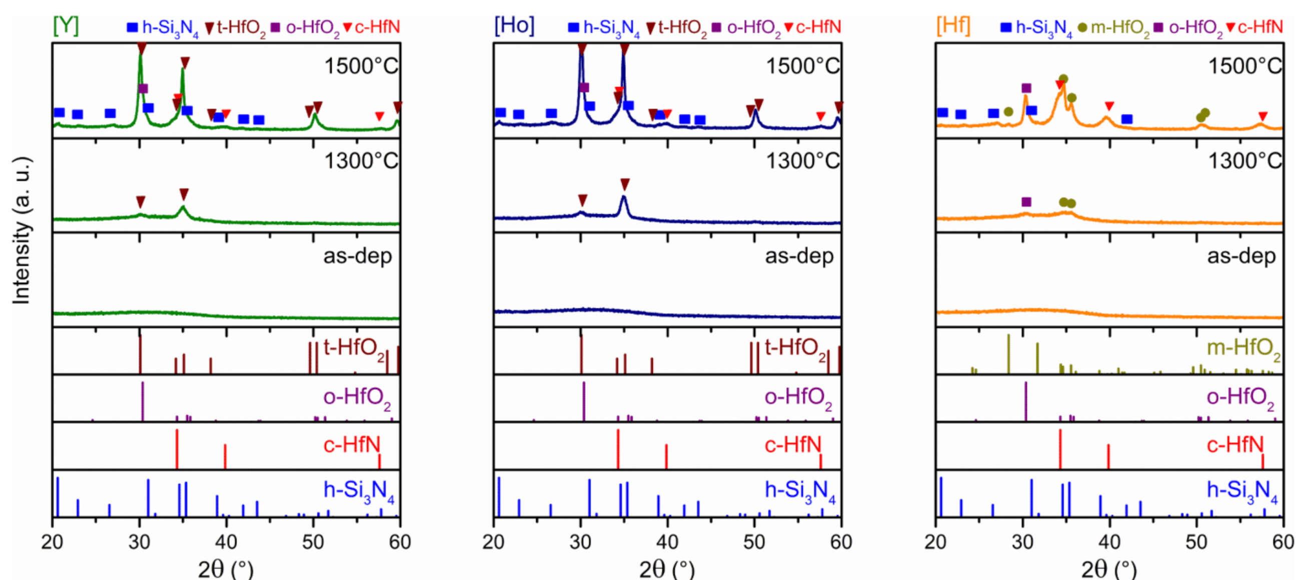

Fig. 2. XRD patterns of the $Hf_6B_{12}Si_{29}Y_2C_2N_{45}$ (green lines on the left side), $Hf_5B_{13}Si_{25}Ho_3C_2N_{48}$ (blue lines in the middle) and $Hf_7B_{10}Si_{32}C_2N_{44}$ (orange lines on the right side) films in as-deposited state and after their annealing in air to 1300 °C and 1500 °C. (For interpretation of the references to color in this figure legend, the reader is referred to the web version of this article.)

3.1. Structure and properties of as-deposited films

The Hf–B–Si(–Y/Ho)–C–N films discussed in this paper were sputter deposited in the argon-nitrogen gas mixture with the fixed 25% N_2 fraction using the target with the fixed 15% Hf, 50% Si, 30% B_4C and 5% Hf/Y/Ho fractions in the target erosion area. Primarily these process parameters determined the elemental composition (in at.%) of the films to be $Hf_7B_{10}Si_{32}C_2N_{44}$, $Hf_6B_{12}Si_{29}Y_2C_2N_{45}$ and $Hf_5B_{13}Si_{25}Ho_3C_2N_{48}$; let us denote the films from now on as [Hf], [Y] and [Ho], respectively. The [Hf] film was prepared as a reference sample in order to be able to investigate the effect of an Y and Ho addition.

All films exhibit an X-ray amorphous structure in the as-deposited state, having a thickness of 1.5 μm and a relatively high hardness of about 22 GPa. The films are electrically non-conductive (the electrical resistivity $\geq 10^8$ Ωm) and optically transparent with a very low value of the extinction coefficient (measured at 550 nm). The refractive index of all films is in the range 2.22−2.25. All these properties of the as-deposited films are summarized in Table 1.

3.2. Thermogravimetric measurements

Using thermogravimetric analysis, we investigated the oxidation resistance of the [Hf], [Y] and [Ho] films in synthetic air up to 1500 °C and their thermal stability in helium up to 1400 °C. Two temperatures of 1300 °C and 1500 °C were selected to characterize changes in the structure of the films after annealing in air.

Thermogravimetric curves of the films annealed in air are depicted in Fig. 1. Apparently, the [Hf] and [Y] films start to oxidize at temperature about 1000 °C as opposed to the [Ho] film with an onset of oxidation at 1200 °C. Above these temperatures, the mass of all films increases continuously, indicating that the formation of solid oxides in the films

Table 1
Properties of the as-deposited Hf–B–Si(–Y/Ho)–C–N films.

Sample	Composition(at.%)	Hardness (GPa)	Refractive index (-)	Extinction coefficient (-)
[Hf]	$Hf_7B_{10}Si_{32}C_2N_{44}$	22.5 ± 0.3	2.23	5×10^{-4}
[Y]	$Hf_6B_{12}Si_{29}Y_2C_2N_{45}$	22.2 ± 0.4	2.22	5×10^{-4}
[Ho]	$Hf_5B_{13}Si_{25}Ho_3C_2N_{48}$	22.0 ± 0.2	2.25	2×10^{-3}

prevails over the release of volatile oxides from the film upon annealing. Simultaneously with oxidation, nitrogen molecules are released from the films. Note that the mass change measured at a final annealing temperature of 1500 °C was in all three cases lower than 25 μg/cm^2.

Fig. 2 shows XRD patterns of the [Hf], [Y] and [Ho] films in the as-deposited state and after annealing in air to 1300 °C and 1500 °C. It confirms the X-ray amorphous structure of all films in the as-deposited state as mentioned above. Furthermore, it is evident that annealing of the films to 1300 °C leads to the formation of HfO_2 nanocrystallites, which are probably located in the oxide surface layer, similarly as reported in our previous paper on Hf–B–Si–C–N films of different compositions [20]. In case of the [Hf] film, the monoclinic HfO_2 (m-HfO_2; PDF Card No. 34–0104) and orthorhombic HfO_2 (o-HfO_2; PDF Card No. 04–003–6960) phases are detected. On the other hand, the addition of yttrium or holmium into the films results in a stabilization of the tetragonal HfO_2 (t-HfO_2; PDF Card No. 08–0342) phase, the only crystalline phase detected in case of [Y] and [Ho] films after annealing to 1300 °C in air. Further annealing of [Hf], [Y] and [Ho] films to 1500 °C leads to the growth of the HfO_2 nanocrystallites and crystallization of the cubic HfN (c-HfN; PDF Card No. 00–033–0592) and hexagonal Si_3N_4 (h-Si_3N_4; PDF Card No. 04–015–3265) phases. In case of the [Y] and [Ho] films, an asymmetry observed on the right shoulder of the first high-intensity diffraction peak of t-HfO_2 can be due to the presence of a minor amount of o-HfO_2 nanocrystallites. We may speculate that the stabilization of the t-HfO_2 phase is likely due to an incorporation of Y or Ho into its lattice. Similarly, Y and Ho can be incorporated into the lattice of HfN. Because we have, however, no direct evidence at the moment (a subject of very detailed parallel TEM/SAED study), we term these phases as t-HfO_2 and HfN.

Using spectroscopic ellipsometry, we also evaluated the thicknesses of oxide layers formed on the surface after annealing of the films in air to 1500 °C. The lowest thickness was measured for the [Y] film with 194 nm, then for the [Ho] film with 202 nm and the highest one for the [Hf] film with 243 nm. This confirms that the addition of yttrium or holmium into the films has a positive effect on their oxidation resistance.

Thermogravimetric curves of the [Hf], [Y] and [Ho] films measured in helium are shown in Fig. 3. It can be seen that there are no mass changes up to about 1315 °C for all films. Above this temperature, mass losses occur in the [Hf] and [Ho] films. On the contrary, an onset of the

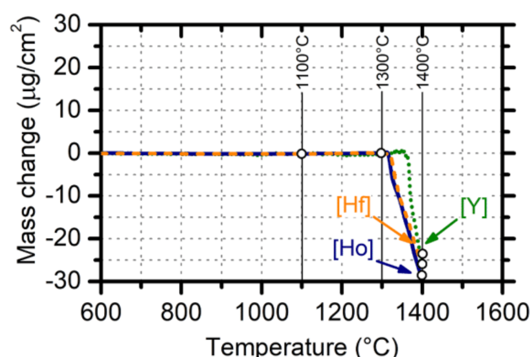

Fig. 3. Thermogravimetric curves of the $Hf_7B_{10}Si_{32}C_2N_{44}$ (orange dashed line), $Hf_6B_{12}Si_{29}Y_2C_2N_{45}$ (green dotted line) and $Hf_5B_{13}Si_{25}Ho_3C_2N_{48}$ (blue solid line) films, measured in helium at a heating rate of 10 °C/min, with highlighted temperatures of 1100 °C, 1300 °C and 1400 °C, where the properties of the films were measured. (For interpretation of the references to color in this figure legend, the reader is referred to the web version of this article.)

mass loss of the [Y] film is shifted to a slightly higher temperature of 1350 °C, most likely due to the most stable amorphous structure of this film. When the amorphous structure, however, becomes unstable, an initiation of diffusion processes promotes segregation and crystallization of different phases on the one hand and the formation and release of N_2 molecules from the film on the other hand. As a consequence, mass losses are detected in the films.

3.3. Evolution of hardness and optical properties

The evolution of the hardness and optical properties of the [Hf], [Y] and [Ho] films after annealing to 1100 °C, 1300 °C and 1400 °C (temperatures highlighted by open circles on the TG curves in Fig. 3) in helium in the thermogravimeter was studied by indentation tests and spectroscopic ellipsometry, respectively.

Fig. 4 shows the hardness of the films as a function of the annealing temperature. It is obvious that annealing to 1100 °C leads to an increase in the hardness of the [Hf], [Y] and [Ho] films to 24.9 ± 0.7 GPa, 25.7 ± 0.6 GPa and 24.6 ± 0.7 GPa, respectively. A similar enhancement of the hardness with increasing annealing temperature was also observed in amorphous Si–B–C—N films prepared in our laboratories [21]. Performing ab-initio calculations, Houška et al. explained it as a result of a thermally activated atomic rearrangement of a homogeneous amorphous structure into a heterogeneous mixture of Si-rich (around incorporated Ar atoms) and Si-poor amorphous nanoscale zones [22]. Since the [Hf], [Y] and [Ho] films contain also about 2 − 4 at.% Ar, we ascribe

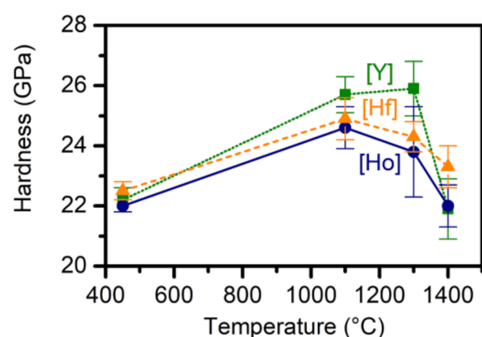

Fig. 4. Evolution of hardness of the $Hf_7B_{10}Si_{32}C_2N_{44}$ (orange dashed line), $Hf_6B_{12}Si_{29}Y_2C_2N_{45}$ (green dotted line) and $Hf_5B_{13}Si_{25}Ho_3C_2N_{48}$ (blue solid line) films with increasing annealing temperature up to 1400 °C in helium. Lines are drawn as guides to the eyes. (For interpretation of the references to color in this figure legend, the reader is referred to the web version of this article.)

the enhancement of the hardness to the same mechanism.

As the annealing temperature is increased to 1300 °C, the hardness of the [Y] film remains nearly the same (25.9 ± 0.9 GPa) but decreases for the [Hf] and [Ho] films. After annealing to 1400 °C, the hardness of all films drops to values that are comparable with those of the as-deposited films. This drop correlates well with the mass losses of the films (Fig. 3) and might be related to structural transformations in the films.

The effect of increasing annealing temperature on the optical properties of the films is presented in Fig. 5. As can be seen from the top panel of Fig. 5, the refractive index of [Hf], [Y] and [Ho] films slightly decreases upon annealing to 1100 °C. With increasing temperature to 1400 °C, the refractive index decreases steeply in all cases to about 1.90 for the [Hf] and [Ho] films, and to 1.97 for the [Y] film. This trend is opposite in case of the extinction coefficient. In the bottom panel of Fig. 5, one can clearly see an increasing tendency with increasing annealing temperature. However, all films investigated are still optically transparent after annealing to 1300 °C with an extinction coefficient equal to or less than 1×10^{-2}. The [Y] film retains its optical transparency even after annealing to 1400 °C with an extinction coefficient of 1×10^{-2}.

3.4. DSC measurements

The thermal stability of the amorphous structure of the films was also investigated by differential scanning calorimetry. For this purpose, the films were annealed in argon up to 1600 °C as powdered samples (for more details about their preparation, see Experimental).

Measured DSC curves of all three films are depicted in Fig. 6. Obviously, there are no exothermic or endothermic peaks detected up to approximately 1400 °C. Above this temperature, a relatively broad exothermic peak is observed on each DSC curve. This peak can be assigned to the transformation of the amorphous structure to a crystalline one. For deeper understanding of the crystallization process and

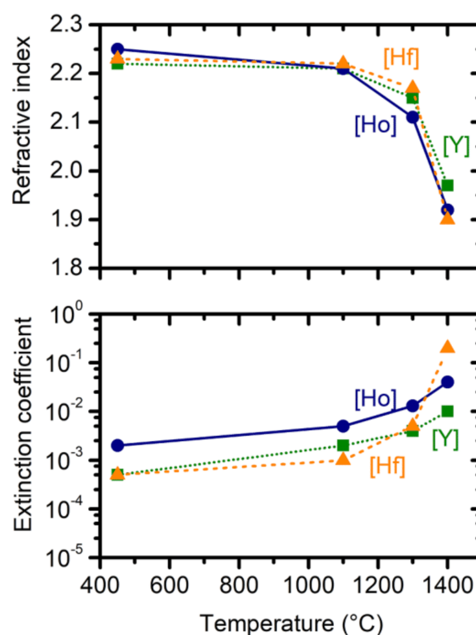

Fig. 5. Evolution of refractive index (top panel) and extinction coefficient (bottom panel), both measured at wavelength of 550 nm, of the $Hf_7B_{10}Si_{32}C_2N_{44}$ (orange dashed line), $Hf_6B_{12}Si_{29}Y_2C_2N_{45}$ (green dotted line) and $Hf_5B_{13}Si_{25}Ho_3C_2N_{48}$ (blue solid line) films with increasing annealing temperature up to 1400 °C in helium. Lines are drawn as guides to the eyes. (For interpretation of the references to color in this figure legend, the reader is referred to the web version of this article.)

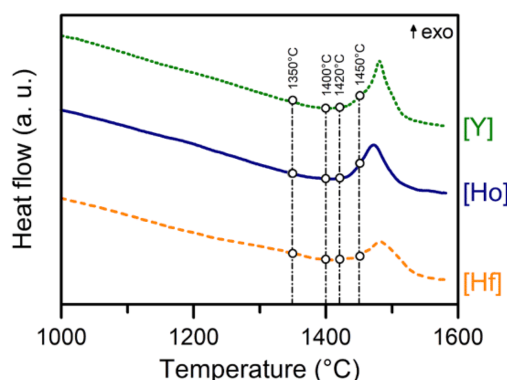

Fig. 6. DSC curves of the $Hf_7B_{10}Si_{32}C_2N_{44}$ (orange dashed line), $Hf_6B_{12}Si_{29}Y_2C_2N_{45}$ (green dotted line) and $Hf_5B_{13}Si_{25}Ho_3C_2N_{48}$ (blue solid line) films annealed in argon from room temperature up to 1600 °C with highlighted temperatures corresponding to XRD patterns shown in Fig. 7. (For interpretation of the references to color in this figure legend, the reader is referred to the web version of this article.)

individual differences among [Hf], [Y] and [Ho] films, the powdered films were annealed to temperatures highlighted on the DSC curves (Fig. 6) and XRD patterns were then taken after cooling down to room temperature (Fig. 7).

It is clearly seen that the thermal stability of the amorphous structure of the as-deposited [Hf], [Y] and [Ho] films is corroborated by XRD up to 1350 °C. At 1400 °C, which is the temperature comparable with that of the onset of the exothermic peaks (see Fig. 6), there is some evidence of the formation of the c-HfN phase in all films. A detailed examination of the XRD patterns revealed, however, a difference between the intensities of the HfN diffraction peaks in the individual films. Since the intensities are lowest in case of the [Y] film, its amorphous structure appears to be the most resistant against crystallization. This is also in agreement with the results obtained by thermogravimetry (Fig. 3). Further increase in the temperature up to 1420 °C leads to a slight increase in intensity of the HfN peaks in all films while maintaining the trend of their lowest intensity in case of the [Y] film. In addition, a very small response from the $h\text{-}Si_3N_4$ phase is also detected in the XRD patterns. Annealing to 1450 °C, which is accompanied by an increase in the intensity of the HfN and Si_3N_4 peaks, still does not result in a fully crystalline film structure. Just annealing to 1600 °C seems to cause a complete crystallization of the structure of the films, consisting of c-HfN and $h\text{-}Si_3N_4$ nanocrystallites.

In summary, the stability of the amorphous structure is the crucial parameter determining the stability of hardness and optical properties of the [Hf], [Y] and [Ho] films.

3.5. SEM imaging

The thermal stability of the microstructure of the films was also investigated by SEM in the mode of secondary electrons. Fig. 8 shows detailed cross-sectional micrographs (near the film/substrate interface) of the [Hf] film in the as-deposited state and after annealing to 1300 °C on the Si substrate, 1400 °C and 1410 °C on the SiC substrate, and the [Y] and [Ho] films on the SiC substrate after annealing to 1410 °C in helium in the thermogravimeter and cooling down to room temperature. It is evident that the [Hf] film is very smooth and dense in the as-deposited state (Fig. 8a). Its annealing to 1300 °C (Fig. 8b) does not cause any visible changes in the microstructure. After annealing to 1400 °C (Fig. 8c), a coarsening of the microstructure of the film near the film/substrate interface is observed, which might be connected with the crystallization of the film (the temperature is namely very close to that observed for the crystallization of the powdered films in Figs. 7 and 8). To confirm this, the [Hf] film was reannealed to 1410 °C and examined in cross-section to see if the coarsening zone had grown in thickness. Fig. 8d brings really evidence of this and the zone is nearly twice (1.8×)

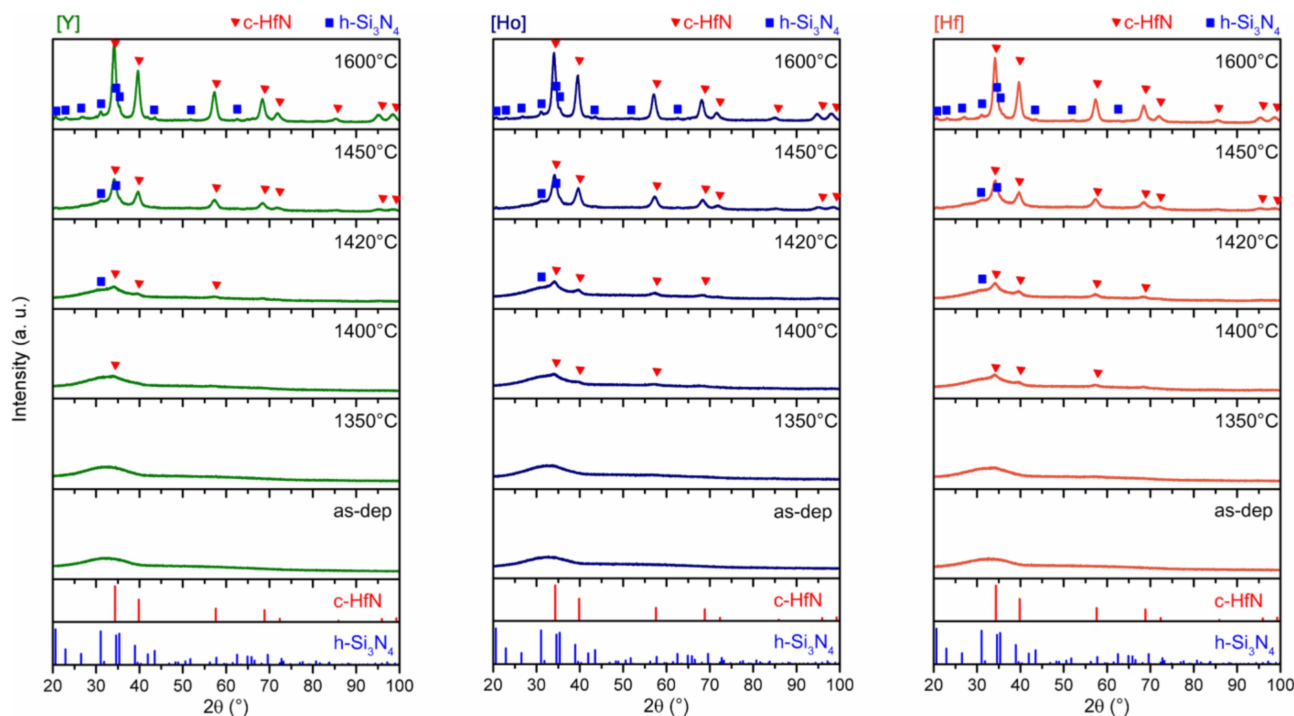

Fig. 7. XRD patterns of the $Hf_6B_{12}Si_{29}Y_2C_2N_{45}$ (green lines on the left side), $Hf_5B_{13}Si_{25}Ho_3C_2N_{48}$ (blue lines in the middle) and $Hf_7B_{10}Si_{32}C_2N_{44}$ (orange lines on the right side) powdered films after their annealing in argon to the temperatures highlighted in Fig. 6. (For interpretation of the references to color in this figure legend, the reader is referred to the web version of this article.)

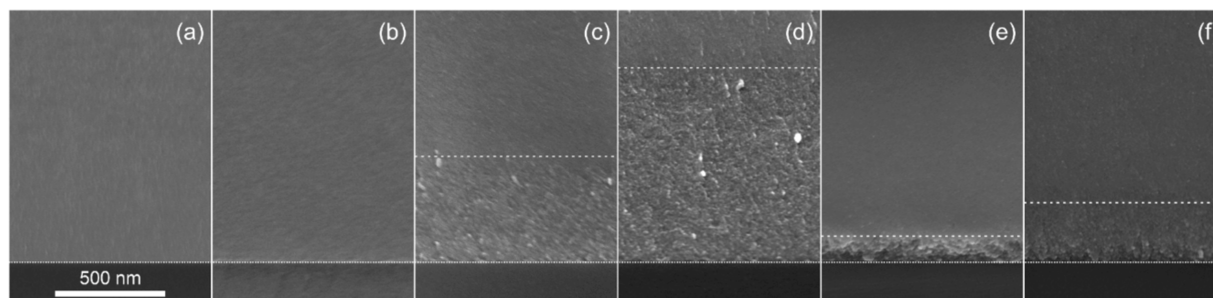

Fig. 8. Cross-sectional SEM micrographs of the $Hf_7B_{10}Si_{32}C_2N_{44}$ film in (a) as-deposited state and after its annealing in helium to (b) 1300 °C, (c) 1400 °C and (d) 1410 °C, and of (e) the $Hf_6B_{12}Si_{29}Y_2C_2N_{45}$ film and (f) the $Hf_5B_{13}Si_{25}Ho_3C_2N_{48}$ film after their annealing in helium to 1410 °C. The crystallizing zones are highlighted by dashed lines and the film/substrate interfaces by dotted lines. (For interpretation of the references to color in this figure legend, the reader is referred to the web version of this article.)

as thick as at 1400 °C. This more than likely suggests that the coarsening of the microstructure is really connected with the crystallization of the [Hf] film. A more detailed study is, of course, necessary and is a subject of our parallel TEM/SAED analyses.

For comparison, the [Y] and [Ho] cross-sectional micrographs after annealing to 1410 °C are also presented (Figs. 8e and 8f). It is evident that the crystallization of both films starts at the film/substrate interface as well. However, the thickness of their crystallizing zones is much smaller compared to the [Hf] film. As seen, the thinnest crystallizing zone is for the [Y] film (≈ 125 nm), then for the [Ho] film (≈ 250 nm) and the thickest for the [Hf] film (≈ 900 nm). This observation confirms the highest resistance to crystallization for the [Y] film, which is in accordance with the results obtained by TG and DSC.

4. Conclusions

Hard and optically transparent $Hf_7B_{10}Si_{32}C_2N_{44}$, $Hf_6B_{12}Si_{29}Y_2C_2N_{45}$ and $Hf_5B_{13}Si_{25}Ho_3C_2N_{48}$ films were prepared by reactive pulsed dc magnetron co-sputtering. It was demonstrated that all of these films are highly oxidation resistant in air at temperatures significantly exceeding 1000 °C and their amorphous structure is thermally stable in inert gasses up to approximately 1400 °C. The effects of an addition of Y and Ho into Hf–B–Si–C–N films were identified.

Using high-resolution thermogravimetric analysis, XRD and ellipsometry, it was found that the addition of 2 − 3 at.% of Y or Ho resulted in a lower thickness of the surface oxide layer and a stabilization of t-HfO_2 phase upon oxidation to 1500 °C. There were no mass changes up to 1300 °C for the $Hf_7B_{10}Si_{32}C_2N_{44}$ and $Hf_5B_{13}Si_{25}Ho_3C_2N_{48}$ films and even up to 1350 °C for the $Hf_6B_{12}Si_{29}Y_2C_2N_{45}$ film upon annealing in helium. The hardness of all films increased with increasing annealing temperature up to 1100 °C and the films were still optically transparent. In case of the $Hf_6B_{12}Si_{29}Y_2C_2N_{45}$ film, the hardness increased even up to 1300 °C and the film remained optically transparent up to 1400 °C.

Differential scanning calorimetry in argon in combination with XRD showed that the transformation of the amorphous structure to the crystalline one starts around 1400 °C. Minute diffraction peaks from c-HfN were observed in all films, but their intensities were the lowest for the $Hf_6B_{12}Si_{29}Y_2C_2N_{45}$ film. Further increase of the annealing temperature resulted in an improvement of the crystallinity of the films with an appearance of other diffraction peaks corresponding to h-Si_3N_4.

SEM imaging revealed that the crystallization of all films was initiated at the film/substrate interface when the films were annealed on the Si or SiC substrate. The lowest thickness of the crystallizing zone was observed for the $Hf_6B_{12}Si_{29}Y_2C_2N_{45}$ film confirming its highest thermal stability among the films investigated.

The results achieved suggest that the addition of Y has the most positive effect on the high-temperature behavior and the $Hf_6B_{12}Si_{29}Y_2C_2N_{45}$ film might be a good candidate for a potential use as high-temperature protective coating of optical or optoelectronic devices.

CRediT authorship contribution statement

M. Kotrlová: Investigation, Data curation, Validation, Visualization, Writing - original draft, Writing - review & editing. **P. Zeman:** Conceptualization, Methodology, Validation, Writing - original draft, Writing - review & editing, Supervision, Funding acquisition. **J. Houška:** Investigation, Data curation, Validation, Writing - review & editing. **V. Šímová:** Investigation, Data curation. **M. Procházka:** Investigation, Data curation, Writing - review & editing. **R. Čerstvý:** Investigation, Data curation. **S. Haviar:** Investigation, Data curation, Visualization, Writing - review & editing. **J. Vlček:** Conceptualization, Methodology, Validation, Writing - review & editing, Supervision.

Declaration of Competing Interest

The authors declare that they have no known competing financial interests or personal relationships that could have appeared to influence the work reported in this paper

Acknowledgments

This work was supported by the project LO1506 of the Czech Ministry of Education, Youth and Sports under the program NPU I. The authors thank Assoc. Prof. Šimon Kos for his valuable and stimulating comments.

References

[1] M.M. Opeka, I.G. Talmy, E.J. Wuchina, J.A. Zaykoski, S.J. Causey, Mechanical, thermal, and oxidation properties of refractory hafnium and zirconium compounds, J. Eur. Ceram. Soc. 19 (1999) 2405–2414, https://doi.org/10.1016/S0955-2219(99)00129-6.

[2] M.M. Opeka, I.G. Talmy, J.A. Zaykoski, Oxidation-based materials selection for 2000°C + hypersonic aerosurfaces: theoretical considerations and historical experience, J. Mater. Sci. 39 (2004) 5887–5904, https://doi.org/10.1023/B:JMSC.0000041686.21788.77.

[3] E. Opila, S. Levine, J. Lorincz, Oxidation of ZrB2- and HfB2-based ultra-high temperature ceramics: effect of Ta additions, J. Mater. Sci. 39 (2004) 5969–5977, https://doi.org/10.1023/B:JMSC.0000041693.32531.d1.

[4] F. Monteverde, A. Bellosi, The resistance to oxidation of an HfB2–SiC composite, J. Eur. Ceram. Soc. 25 (2005) 1025–1031, https://doi.org/10.1016/J.JEURCERAMSOC.2004.05.009.

[5] W.G. Fahrenholtz, G.E. Hilmas, I.G. Talmy, J.A. Zaykoski, Refractory diborides of zirconium and hafnium, J. Am. Ceram. Soc. 90 (2007) 1347–1364, https://doi.org/10.1111/j.1551-2916.2007.01583.x.

[6] C.M. Carney, P. Mogilvesky, T.A. Parthasarathy, Oxidation behavior of zirconium diboride silicon carbide produced by the spark plasma sintering method, J. Am. Ceram. Soc. 92 (2009) 2046–2052, https://doi.org/10.1111/j.1551-2916.2009.03134.x.

[7] C.M. Carney, Oxidation resistance of hafnium diboride—silicon carbide from 1400 to 2000 °C, J. Mater. Sci. 44 (2009) 5673–5681, https://doi.org/10.1007/s10853-009-3799-7.

[8] X. Ren, H. Li, Y. Chu, Q. Fu, K. Li, Ultra-high-temperature ceramic HfB2-SiC coating for oxidation protection of SiC-coated carbon/carbon composites, Int. J. Appl. Ceram. Technol. 12 (2015) 560–567, https://doi.org/10.1111/ijac.12241.
[9] ed. D. Ghosh, G. Subhash, Recent progress in Zr (Hf)B2 based ultrahigh temperature ceramics in Handbook of Advanced Ceramics (2nd edition), Materials, Applications, in: S. Somnya (Ed.), Processing Amd Properties, 2nd editio, Academic Press, 2013. ed.
[10] V. Šímová, J. Vlček, Š. Zuzjaková, J. Houška, Y. Shen, J. Jiang, E.I. Meletis, V. Peřina, Magnetron sputtered Hf–B–Si–C–N films with controlled electrical conductivity and optical transparency, and with ultrahigh oxidation resistance, Thin Solid Films 653 (2018) 333–340, https://doi.org/10.1016/J.TSF.2018.03.064.
[11] P. Zeman, Š. Zuzjaková, P. Mareš, R. Čerstvý, M. Zhang, J. Jiang, E.I. Meletis, J. Vlček, Superior high-temperature oxidation resistance of magnetron sputtered Hf–B–Si–C–N film, Ceram. Int. 42 (2016) 4853–4859, https://doi.org/10.1016/J.CERAMINT.2015.11.171.
[12] P. Zeman, Š. Zuzjaková, R. Čerstvý, J. Houška, Y. Shen, J. Todt, J. Jiang, R. Daniel, J. Keckes, E.I. Meletis, J. Vlček, Extraordinary high-temperature behavior of electrically conductive Hf7B23Si22C6N40 ceramic film, Surf. Coatings Technol. 391 (2020), 125686, https://doi.org/10.1016/J.SURFCOAT.2020.125686.
[13] Y. Shen, J.C. Jiang, P. Zeman, V. Šímová, J. Vlček, E.I. Meletis, Microstructure evolution in amorphous Hf-B-Si-C-N high temperature resistant coatings after annealing to 1500 °C in air, Sci. Rep. 9 (2019) 1–11, https://doi.org/10.1038/s41598-019-40428-6.
[14] K.N. Lee, D.S. Fox, N.P. Bansal, Rare earth silicate environmental barrier coatings for SiC/SiC composites and Si3N4 ceramics, J. Eur. Ceram. Soc. 25 (2005) 1705–1715, https://doi.org/10.1016/j.jeurceramsoc.2004.12.013.
[15] B.K. Jang, F.J. Feng, K.S. Lee, E. García, A. Nistal, N. Nagashima, S. Kim, Y.S. Oh, H.T. Kim, Thermal behavior and mechanical properties of Y2SiO5 environmental barrier coatings after isothermal heat treatment, Surf. Coat. Technol. 308 (2016) 24–30, https://doi.org/10.1016/j.surfcoat.2016.09.088.
[16] M.H. Lu, H.M. Xiang, Z.H. Feng, X.Y. Wang, Y.C. Zhou, Mechanical and thermal properties of Yb2SiO5: a promising material for T/EBCs applications, J. Am. Ceram. Soc. 99 (2016) 1404–1411, https://doi.org/10.1111/jace.14085.
[17] N. Al Nasiri, N. Patra, D. Horlait, D.D. Jayaseelan, W.E. Lee, Thermal properties of rare-earth monosilicates for EBC on Si-based ceramic composites, J. Am. Ceram. Soc. 99 (2016) 589–596, https://doi.org/10.1111/jace.13982.
[18] Z. Tian, L. Zheng, Z. Li, J. Li, J. Wang, Exploration of the low thermal conductivities of γ-Y2Si2O7, β-Y2Si2O7, β-Yb2Si2O7, and β-Lu2Si2O7 as novel environmental barrier coating candidates, J. Eur. Ceram. Soc. 36 (2016) 2813–2823, https://doi.org/10.1016/j.jeurceramsoc.2016.04.022.
[19] Z. Tian, L. Zheng, J. Wang, P. Wan, J. Li, J. Wang, Theoretical and experimental determination of the major thermo-mechanical properties of RE2SiO5 (RE=Tb, Dy, Ho, Er, Tm, Yb, Lu, and Y) for environmental and thermal barrier coating applications, J. Eur. Ceram. Soc. 36 (2016) 189–202, https://doi.org/10.1016/j.jeurceramsoc.2015.09.013.
[20] M. Zhang, J. Jiang, P. Zeman, Š. Zuzjaková, J. Vlček, E. Meletis, Study of the high-temperature oxidation resistance mechanism of magnetron sputtered Hf7B23Si17C4N45 film, J. Vac. Sci. Technol. A Vac. Surf. Film. 36 (2018) 21505, https://doi.org/10.1116/1.5004145.
[21] J. Kalaš, R. Vernhes, S. Hřeben, J. Vlček, J.E. Klemberg-Sapieha, L. Martinu, High-temperature stability of the mechanical and optical properties of Si–B–C–N films prepared by magnetron sputtering, Thin Solid Films. 518 (2009) 174–179, https://doi.org/10.1016/J.TSF.2009.06.017.
[22] J. Houška, J. Kalaš, J. Vlček, M.M.M. Bilek, D.R. McKenzie, Effect of implanted argon on hardness of novel magnetron sputtered Si-B-C-N materials: experiments and ab initio simulations, J. Phys. Condens. Matter. 19 (2007) 1–13, https://doi.org/10.1088/0953-8984/19/19/196228.

IV Conclusions

The Ph.D. thesis is devoted to thin-film alloys and non-oxide ceramics with amorphous or metastable crystalline structure. A systematic investigation of high-temperature behavior of binary Zr–Cu, ternary Zr–Hf–Cu and quaternary Zr–Hf–Al/Si–Cu TFMGs and senary Hf–B–Si–Y/Ho–C–N ceramic films was carried out. Thin-film alloys from the binary W–Zr system were prepared and characterized in detail.

The main results can be summarized as follows:

1) The crystallization and oxidation behavior of binary $Zr_{54}Cu_{46}$ and ternary $Zr_{27}Hf_{27}Cu_{46}$ thin-film metallic glasses were systematically investigated by differential scanning calorimetry and high-resolution thermogravimetry, respectively, and the oxidation behavior was compared with that of a crystalline $Zr_{54}Cu_{46}$ thin-film alloy. It was found that the crystallization of the $Zr_{54}Cu_{46}$ film takes place at a lower temperature and in two successive steps in contrast to the $Zr_{27}Hf_{27}Cu_{46}$ film. The apparent activation energy E_a of the primary crystallization determined by non-isothermal kinetics using the Kissinger–Akahira–Sunose method is higher in the case of the $Zr_{27}Hf_{27}Cu_{46}$ film for all conversion fractions α compared to the $Zr_{54}Cu_{46}$ film (e.g. $E_a = 279$ kJ/mol vs. 230 kJ/mol for $\alpha = 0.5$). This suggests that the crystallization process of the $Zr_{27}Hf_{27}Cu_{46}$ film is more difficult and the film is more thermally stable than the $Zr_{54}Cu_{46}$ film. The onset of the oxidation of the crystalline $Zr_{54}Cu_{46}$ alloy, and the amorphous $Zr_{54}Cu_{46}$ and $Zr_{27}Hf_{27}Cu_{46}$ metallic glasses is 355 °C, 475 °C and 550 °C, respectively, upon the dynamical heating. The poorest oxidation resistance in the case of the crystalline $Zr_{54}Cu_{46}$ film is caused by the presence of grain boundaries that serve as channels for fast interdiffusion of species. Since an amorphous structure is free of grain boundaries, the metallic glasses exhibit an enhanced oxidation resistance. Moreover, the substitution of Hf for Zr further improves the oxidation resistance because of the formation of more protective oxide surface layer. The oxidation behavior upon the isothermal annealing is governed by diffusion-controlled kinetics in the temperature range from 400 to 575 °C. The activation energy of the oxidation process determined from the Arrhenius equation for the parabolic oxidation rate constants is 112, 143 and 208 kJ/mol for the crystalline $Zr_{54}Cu_{46}$ film, and the amorphous $Zr_{54}Cu_{46}$ and $Zr_{27}Hf_{27}Cu_{46}$ films, respectively. These results confirm that the most protective oxide layer is formed on the surface of the $Zr_{27}Hf_{27}Cu_{46}$ film.

2) The effect of an addition of Al (up to 17 at.%) or Si (up to 12 at.%) into ternary Zr–Hf–Cu thin-film alloys on their thermal stability and oxidation resistance was investigated. All films were found to be amorphous in the whole studied range, but the glass transition was, however, recognizable only up to 12 at.% Al and 6 at.% Si. The increase of the Al and Si content led to an increase of the crystallization (up to 12 at.% Al and Si) and glass transition (up to 12 at.% Al and 6 at.% Si) temperature. This can be explained based on the increasing effect of a covalent component of the mixed metallic-covalent bonds between Al or Si and other elements of the films. In addition, a wider super-cooled liquid region was obtained for the Zr–Hf–Al–Cu metallic glasses, while a better oxidation resistance was achieved for the Zr–Hf–Si–Cu metallic glasses.

3) Binary W–Zr thin-film alloys were deposited in a very wide composition range (3 – 99 at.% Zr) onto unheated and unbiased substrates and systematically characterized in the as-deposited state. Using the non-equilibrium process of non-reactive dc magnetron co-sputtering of Zr and W targets led to the formation of different metastable structures in this system. W-rich films with up to 24 at.% Zr were prepared as single-phase crystalline materials with a supersaturated α-W(Zr) solid solution structure and columnar microstructure. A gradual substitution of Zr for W in the bcc α-W lattice led to an increase of the hardness due to solid-solution hardening (up to 16.1 GPa), decrease of the residual stress (down to -0.05 GPa), and increase of the surface roughness (up to 12.4 nm) and the electrical resistivity (up to 5.6×10^{-7} Ωm) compared to a pure W film. An addition of 28 at.% Zr resulted in the formation of a dual-phase glassy-crystalline structure consisting of columnar conical crystalline domains of the α-W(Zr) structure surrounded by a W–Zr metallic glass. Fully amorphous W–Zr films with metallic glass features were prepared in a wide range of 33 – 83 at.% Zr. These films were characterized by a very low surface roughness (down to 0.4 nm), compressive stress (up to -0.72 GPa), composition-independent electrical resistivity (around 13×10^{-7} Ωm) and gradually decreasing hardness (from 12.1 to 4.7 GPa) due to reducing average bond energy. Further addition of Zr (≥ 86 at.%) led to a gradual vanishing of the amorphous W–Zr phase (86 – 88 at.% Zr) and to the formation of Zr-rich films with a predominantly dual-phase crystalline structure exhibiting a gradual transition from a metastable β-Zr(W) solid solution (86 – 96 at.% Zr) through a metastable ω-Zr(W) solid solution (94 – 100 at.% Zr) to the thermodynamically stable α-Zr phase (99 – 100 at.% Zr) with increasing Zr (decreasing W) content. The films with the dominant β-Zr(W) phase

were observed to possess a slightly higher hardness, a lower surface roughness and a higher electrical resistivity compared to the films with the dominant ω-Zr(W) or α-Zr phases. Investigation of the high-temperature behavior of the W–Zr thin-film alloys is now in progress and is beyond the scope of this Ph.D. thesis.

4) Hard and optically transparent $Hf_7B_{10}Si_{32}C_2N_{44}$, $Hf_6B_{12}Si_{29}Y_2C_2N_{45}$ and $Hf_5B_{13}Si_{25}Ho_3C_2N_{48}$ films are highly oxidation resistant in air at temperatures significantly exceeding 1000 °C and their amorphous structure is thermally stable in inert gasses up to approximately 1400 °C. It was found that the addition of 2 − 3 at.% of Y or Ho resulted in a lower thickness of the surface oxide layer and a stabilization of t-HfO_2 phase upon oxidation to 1500 °C. There were no mass changes up to 1300 °C for the $Hf_7B_{10}Si_{32}C_2N_{44}$ and $Hf_5B_{13}Si_{25}Ho_3C_2N_{48}$ films and even up to 1350 °C for the $Hf_6B_{12}Si_{29}Y_2C_2N_{45}$ film upon annealing in helium. The hardness of all films increased with increasing annealing temperature up to 1100 °C and the films were still optically transparent. In case of the $Hf_6B_{12}Si_{29}Y_2C_2N_{45}$ film, the hardness increased even up to 1300 °C and the film remained optically transparent up to 1400 °C. The transformation of the amorphous structure to the crystalline one starts in all cases around 1400 °C. SEM imaging revealed that the crystallization of all films was initiated at the film/substrate interface when the films were annealed on the Si or SiC substrate. The lowest thickness of the crystallizing zone was observed for the $Hf_6B_{12}Si_{29}Y_2C_2N_{45}$ film confirming its highest thermal stability among the films investigated. The results achieved suggest that the addition of Y has the most positive effect on the high-temperature behavior and the $Hf_6B_{12}Si_{29}Y_2C_2N_{45}$ film might be a good candidate for a potential use as high-temperature protective coating of optical or optoelectronic devices.

V Further publications of the candidate

1. Papers in impacted international journals

[1] M. Zítek, P. Zeman, Š. Zuzjaková, M. Kotrlová, R. Čerstvý
"Tuning properties and behavior of magnetron sputtered Zr–Hf–Cu metallic glasses"
Alloys Compd. 739 (2018) 848-855.

[2] Y. Shen, J. Jiang, P. Zeman, M. Kotrlová, V. Šímová, J. Vlček, E. I. Meletis
"Microstructure of High Temperature Oxidation Resistant $Hf_6B_{10}Si_{31}C_2N_{50}$ and $Hf_7B_{10}Si_{32}C_2N_{44}$ Films"
Coatings 10 (2020) 1170.

2. Contributions at international conferences

[1] M. Zítek, P. Zeman, Š. Zuzjaková, R. Čerstvý, S. Haviar, M. Kotrlová
"Mechanical and Thermal Behavior of Magnetron Sputtered Zr–Cu and Zr–Hf–Cu Metallic Glasses
44th International Conference on Metallurgical Coatings and Thin Films (ICMCTF 2017) 24.–28. 4. 2017, San Diego, USA. (co-author of oral presentation).

[2] P. Zeman, M. Zítek, Š. Zuzjaková, R. Čerstvý, S. Haviar, M. Kotrlová
"Properties and thermal behavior of magnetron sputtered Zr–Cu and Zr–Hf–Cu metallic glasses"
E-MRS 2017 Spring Meeting 22.–26. 5. 2017, Strasbourg, France. (co-author of oral presentation).

[3] P. Zeman, M. Zítek, Š. Zuzjaková, R. Čerstvý, S. Haviar, M. Kotrlová
"Tuning mechanical and thermal properties of magnetron sputtered Zr–Hf–Cu metallic glasses"
24th International Symposium on Metastable, Amorphous and Nanostructured Materials (ISMANAM 2017) 18.–23. 6. 2017, Donostia-San Sebastian, Spain. (co-author of oral presentation).

[4] M. Zítek, P. Zeman, Š. Zuzjaková, R. Čerstvý, S. Haviar, M. Kotrlová
"Mechanical properties and thermal behavior of Zr–Hf–Cu thin film metallic

glasses"
European Congress and Exhibition on Advanced Materials and Processes (EUROMAT2017) 17.–22. 9. 2017, Thessaloniki, Greece. (co-author of poster presentation).

[5] M. Zítek, P. Zeman, Š. Zuzjaková, R. Čerstvý, S. Haviar, M. Kotrlová
"Tuning properties and behavior of magnetron sputtered Zr–Hf–Cu metallic glasses"
16th International Conference on Reactive Sputter Deposition (RSD 2017) 4.–6. 12. 2017, Plzeň, Czech Republic. (co-author of poster presentation).

[6] M. Procházka, V. Šímová, J. Vlček, M. Kotrlová, R. Čerstvý, J. Houška
"Magnetron Sputtered High-temperature Hf–B–Si–X–C–N (X = Y, Ho, Mo) Films with Controlled Optical Transparency and Electrical Conductivity"
45th International Conference on Metallurgical Coatings and Thin Films (ICMCTF 2018) 23.–27. 4. 2018, San Diego, USA. (co-author of oral presentation).

[7] V. Šímová, J. Vlček, M. Kotrlová, R. Čerstvý, J. Houška
"Magnetron sputtered high-temperature Hf–B–Si–X–C–N (X = Y, Ho, Mo, Zr, Ta) films with controlled properties"
E-MRS 2018 Spring Meeting 18.–22. 6. 2018, Strasbourg, France. (co-author of oral presentation).

[8] M. Zítek, P. Zeman, M. Kotrlová, R. Čerstvý
"Impact of alloying on properties and oxidation resistance of magnetron sputtered Zr–Hf–Cu based metallic glasses"
25th International Symposium on Metastable, Amorphous and Nanostructured Materials (ISMANAM 2018) 2.–6. 7. 2018, Rome, Italy. (co-author of oral presentation).

[9] M. Kotrlová, M. Zítek, P. Zeman
"Differences in properties and oxidation behavior of amorphous and crystalline magnetron sputtered Zr–Cu alloys"
17th Joint Vacuum Conference (JVC 2018), 10. - 14. 9. 2018, Olomouc, Czech Republic. (poster presentation).

[10] M. Kotrlová, V. Šímová, J. Vlček, R. Čerstvý, J. Houška
"Magnetron sputtered high-temperature Hf–B–Si–X–C–N (X = Y, Ho, Mo, Zr, Ta) films with controlled optical transparency and electrical conductivity"
16th International Conference on Plasma Surface Engineering (PSE 2018), 17.–21. 9. 2018 Garmisch-Partenkirchen, Germany. (poster presentation).

[11] M. Zítek, M. Kotrlová, P. Zeman
“Differences in properties and oxidation behavior of amorphous and crystalline magnetron sputtered Zr–Cu alloys”
16th International Conference on Plasma Surface Engineering (PSE 2018), 17.–21. 9. 2018 Garmisch-Partenkirchen, Germany. (co-author of poster presentation).

[12] P. Zeman, M. Zítek, M. Kotrlová, R. Čerstvý
“Impact of alloying on properties and oxidation resistance of magnetron sputtered Zr–Hf–Cu based metallic glasses”
16th International Conference on Plasma Surface Engineering (PSE 2018), 17.–21. 9. 2018 Garmisch-Partenkirchen, Germany. (co-author of oral presentation).

[13] M. Kotrlová, M. Zítek, P. Zeman
“On crystallization and oxidation behavior of $Zr_{54}Cu_{46}$ and $Zr_{27}Hf_{27}Cu_{46}$ thin-film metallic glasses compared to a crystalline $Zr_{54}Cu_{46}$ thin-film alloy”
46th International Conference on Metallurgical Coatings and Thin Films (ICMCTF 2019) 19.–24. 5. 2019 San Diego, USA. (oral presentation).

[14] M. Kotrlová, Š. Zuzjaková, P. Zeman
“Crystallization and oxidation kinetics of Zr–Cu and Zr–Hf–Cu thin-film metallic glasses”
2nd Journal of Thermal Analysis and Calorimetry Conference and 7th V4 Thermoanalytical Conference (JTACC+V4 2019) 18.–21. 6. 2019, Budapešť, Hungary. (oral presentation).

[15] M. Kotrlová, P. Zeman, J. Houška, R. Čerstvý, M. Procházka, J. Vlček
“High-temperature oxidation resistance and thermal stability of hard and optically transparent Hf–B–Si–(Y/Ho–)C–N coatings”
European Congress and Exhibition on Advanced Materials and Processes 2019 (EUROMAT 2019) 1.–5. 9. 2019, Stockholm, Sweden. (poster presentation).

Abstract

This Ph.D. thesis reports on investigation of the high-temperature behavior of binary Zr–Cu, ternary Zr–Hf–Cu and quaternary Zr–Hf–Al/Si–Cu TFMGs and senary Hf–B–Si–Y/Ho–C–N ceramic films, and on preparation and characterization of thin-film alloys from the binary W–Zr system.

Chapter I is devoted to a general introduction. In Chapter II, the aims of the thesis are defined. Chapter III, which is the main part of the Ph.D. thesis, is devoted to the results achieved during my study. The chapter is composed of four papers published in international journals (Parts A, B, D and E) and one draft of the paper submitted for publication in international journal (Part C).

A The crystallization and oxidation behavior of binary $Zr_{54}Cu_{46}$ and ternary $Zr_{27}Hf_{27}Cu_{46}$ thin-film metallic glasses was investigated by differential scanning calorimetry and high-resolution thermogravimetry, respectively, and the oxidation behavior was compared with that of a crystalline $Zr_{54}Cu_{46}$ thin-film alloy. The activation energy of the crystallization was obtained by the Kissinger–Akahira–Sunose method. The results show that the activation energy of the $Zr_{27}Hf_{27}Cu_{46}$ film was higher for all conversion fractions. This indicates that the substitution of Hf for Zr enhances the thermal stability of the glassy state. Considerable attention was also paid to the isothermal oxidation behavior of the amorphous and crystalline $Zr_{54}Cu_{46}$, and amorphous $Zr_{27}Hf_{27}Cu_{46}$ films. The activation energy of the oxidation process determined by the Arrhenius equation for the oxidation rate constants was found to be the highest for the $Zr_{27}Hf_{27}Cu_{46}$ film, which indicates that its surface oxide layer is a more effective barrier against the diffusion of species.

B The effect of an addition of Al (up to 17 at.%) or Si (up to 12 at.%) into the ternary Zr–Hf–Cu thin-film alloys on their thermal behavior and oxidation resistance was systematically investigated. All Zr–Hf–Al/Si–Cu films exhibited an X-ray amorphous structure, but the glass transition was recognized only in the case of films containing up to 12 at.% Al or 6 at.% Si. The addition of Al or Si enhances the thermal stability of their amorphous state. This may be explained by an increase of a covalent component of the mixed metallic-covalent bonds with increasing the Al and Si content. Moreover, the Zr–Hf–Al–Cu metallic glasses exhibit a wider super-cooled liquid region, while the Zr–Hf–Si–Cu metallic glasses are more oxidation resistant.

C The effect of the elemental composition of binary W–Zr thin-film alloys on the formation of different structures and phases was studied in a very wide range of 3 – 99 at.% Zr. The microstructure and properties of the films were related to the individual metastable structures prepared. We found that W-rich films with an α-W(Zr) solid solution structure can be prepared in much wider range of the elemental composition (up to 24 at.% Zr) than indicated in the equilibrium W–Zr phase diagram. They exhibited an enhanced hardness (up to 16.1 GPa) and a reduced residual stress (down to -0.05 GPa). Amorphous W–Zr films with a very low surface roughness (down to 0.4 nm) and metallic glass features were prepared with the Zr content between 33 and 83 at.%. The hardness of these films gradually decreased with increasing Zr content due to reducing average bond energy. All films were in the compressive state in contrast to the crystalline ones. The structure of crystalline Zr-rich films with higher than 88 at.% Zr was predominantly dual-phased exhibiting a gradual transition from a metastable β-Zr(W) solid solution (86 – 96 at.% Zr) through a metastable ω-Zr(W) solid solution (94 – 100 at.% Zr) to the thermodynamically stable α-Zr phase (99 – 100 at.% Zr) with increasing Zr (decreasing W) content. We also observed the formation of dual-phase glassy-crystalline structures in the transition zones between fully crystalline and glassy films.

D Self-formation of a unique dual glassy-crystalline structure in binary W–Zr system was observed for a film with 28 at.% Zr prepared by magnetron co-sputtering. The film is composed of conical columnar domains of α-W(Zr) solid solution structure surrounded by featureless areas corresponding to a W–Zr metallic glass. The conical domains have their axes perpendicular to the film surface. Most of the domains have the apex at or close to the substrate surface, which corresponds to the point of primary nucleation. The surface ratio of glassy and crystalline phase (bases of the cones) is dependent on the film thickness. The dual structure is prepared in a very narrow window of the elemental composition. We suppose that the specific elemental composition and the diffusivity or mobility of sputtered adatoms are crucial for the self-formation of the dual structure.

E Hard and optically transparent amorphous $Hf_7B_{10}Si_{32}C_2N_{44}$, $Hf_6B_{12}Si_{29}Y_2C_2N_{45}$ and $Hf_5B_{13}Si_{25}Ho_3C_2N_{48}$ films were examined for the oxidation resistance in air and thermal stability in inert gasses up to 1600 °C. A thermal evolution of their structure, hardness and optical properties was also studied. An addition of Y or Ho (2 – 3 at.%) into Hf–B–Si–C–N films leads to a stabilization of tetragonal HfO_2 in a surface oxide layer upon oxidation. The thickness of this layer is the lowest for the Y addition. Upon annealing in He, no mass

changes are detected up to 1315 °C and this temperature is shifted even to 1350 °C for the $Hf_6B_{12}Si_{29}Y_2C_2N_{45}$ film. The hardness of this film is enhanced from 22.2 GPa in the as-deposited state to 25.9 GPa after annealing to 1300 °C and the film retains its optical transparency up to 1400 °C. The crystallization of the amorphous structure occurs at around 1400 °C.

Chapter IV consists of the conclusions of the Ph.D. thesis. Chapter V lists further publications of the candidate.

Resumé

Disertační práce se zabývá vyšetřováním vysokoteplotního chování binárních Zr–Cu, ternárních Zr–Hf–Cu a kvaternárních Zr–Hf–Al/Si–Cu tenkovrstvých kovových skel a víceprvkových keramických vrstev Hf–B–Si–Y/Ho–C–N a také přípravou a charakterizací tenkovrstvých slitin W–Zr.

Kapitola I je věnována obecnému úvodu. V kapitole II jsou definovány cíle disertační práce. Kapitola III, která je hlavní částí této práce, je věnována výsledkům získaným během doktorského studia. Kapitola se skládá ze čtyř článků publikovaných v mezinárodních časopisech (části A, B, D a E) a jednoho konceptu vědeckého článku připraveného k publikaci (část C).

A Krystalizační a oxidační chováni binárních $Zr_{54}Cu_{46}$ a ternárních $Zr_{27}Hf_{27}Cu_{46}$ tenkovrstvých kovových skel bylo vyšetřováno pomocí diferenciální skenovací kalorimetrie a termogravimetrie. Oxidační chování těchto vrstev bylo dále porovnáno s oxidačním chováním krystalických tenkovrstvých slitin $Zr_{54}Cu_{46}$. Pro výpočet aktivační energie krystalizace byla použita metoda Kissinger–Akahira–Sunose. Bylo zjištěno, že aktivační energie vrstvy $Zr_{27}Hf_{27}Cu_{46}$ je vyšší pro všechny stupně konverze, což naznačuje, že substituce Hf za Zr vede ke zvýšení teplotní stability skelného stavu. Značná pozornost byla věnována také izotermickému oxidačnímu chování amorfní a krystalické vrstvy $Zr_{54}Cu_{46}$ a amorfní vrstvy $Zr_{27}Hf_{27}Cu_{46}$. Aktivační energie oxidace, která byla určena z Arrheniovy rovnice pro výpočet rychlostní konstanty oxidace, byla nejvyšší v případě vrstvy $Zr_{27}Hf_{27}Cu_{46}$. To znamená, že oxidová vrstva vytvořená během ohřevu na povrchu vrstvy $Zr_{27}Hf_{27}Cu_{46}$ slouží jako nejúčinnější ochranná bariéra zabraňující difúzi částic z námi vyšetřovaných vrstev.

B V této části byl vyšetřován vliv přidání Al (až 17 at.%) nebo Si (až 12 at.%) do ternárních tenkovrstvých slitin Zr–Hf–Cu na jejich teplotní chování a oxidační odolnost. Všechny připravené vrstvy Zr–Hf–Al/Si–Cu měly amorfní strukturu, ale teplota skelného přechodu byla rozpoznána pouze v případě vrstev do 12 at.% Al nebo 6 at.% Si. Bylo pozorováno, že přidání Al nebo Si do vrstev Zr–Hf–Cu vede ke zvýšení jejich teplotní stability. To lze vysvětlit zvyšujícím se podílem kovalentní složky ve smíšené kovalentně-kovové vazbě v důsledku zvyšování obsahu Al a Si ve vrstvách. Dále bylo pozorováno, že přidání Al do kovových skel Zr–Hf–Cu vede k rozšíření oblasti přechlazené kapaliny a přidání Si ke zlepšení oxidační odolnosti kovových skel Zr–Hf–Cu.

C Vliv prvkového složení binárních tenkovrstvých slitin W–Zr na vytvoření rozdílných struktur a fází ve vrstvách byl studován ve velmi širokém rozsahu složení (3 – 99 at.% Zr). Byl diskutován vliv jednotlivých metastabilních fází na výslednou mikrostrukturu a vlastnosti vrstev. Bylo zjištěno, že struktura vrstev s vysokým obsahem W (až do 24 at.% Zr) je tvořena tuhým roztokem α-W(Zr). Tyto vrstvy vykazují zvýšenou tvrdost (až 16,1 GPa) a nízkou hodnotu zbytkového pnutí (až -0,05 GPa). Amorfní vrstvy W–Zr s velmi nízkou drsností povrchu (až 0,4 nm) a charakteristickými vlastnostmi kovových skel byly připraveny v případě obsahu Zr mezi 33 a 83 at.%. Tvrdost těchto vrstev se s rostoucím obsahem Zr postupně snižovala, což bylo způsobeno klesající průměrnou vazebnou energií. Na rozdíl od krystalických vrstev vykazovaly všechny amorfní vrstvy tlakové pnutí. Vrstvy s vysokým obsahem Zr (> 88 at.% Zr) byly krystalické a jejich struktura byla převážně dvoufázová s postupným přechodem od metastabilního tuhého roztoku β-Zr(W) (86 – 96 at.% Zr) přes metastabilní tuhý roztok ω-Zr(W) (94 – 100 at.% Zr) až k termodynamicky stabilní fázi α-Zr (99 – 100 at.% Zr). V přechodových oblastech mezi plně krystalickou a skelnou strukturou pak došlo k vytvoření dvoufázové skelno-krystalické struktury.

D V případě vrstvy W–Zr s 28 at.% Zr připravené magnetronovým naprašováním dochází během depozice k vytvoření unikátní dvoufázové skelno-krystalické struktury. Ta se skládá z kónických krystalických oblastí tvořených tuhým roztokem α-W(Zr) obklopených amorfními oblastmi, které odpovídají kovovému sklu W–Zr. Většina kónických oblastí, jejichž osy jsou kolmé k povrchu vrstvy, má vrchol na povrchu substrátu nebo v jeho blízkosti. Tento bod (vrchol) je zároveň bodem primární nukleace. Poměr skelné a krystalické fáze na povrchu vrstvy je pak závislý na tloušťce vrstvy. K vytvoření této dvoufázové struktury dochází pouze ve velmi úzkém rozsahu prvkového složení. Předpokládáme, že kromě prvkového složení vrstev hraje při vzniku této dvoufázové struktury důležitou roli také difuzivita a mobilita naprašovaných atomů.

E Oxidační odolnost a teplotní stabilita tvrdých a opticky transparentních amorfních vrstev $Hf_7B_{10}Si_{32}C_2N_{44}$, $Hf_6B_{12}Si_{29}Y_2C_2N_{45}$ a $Hf_5B_{13}Si_{25}Ho_3C_2N_{48}$ byla vyšetřována ve vzduchu a inertních plynech až do teploty 1600 °C. Vyšetřován byl také vliv rostoucí teploty na strukturu, tvrdost a optické vlastnosti vrstev. Bylo zjištěno, že přidáním Y nebo Ho do vrstev Hf–B–Si–C–N dochází ke stabilizaci tetragonálního HfO_2, který se nachází po ohřevu v povrchové oxidové vrstvě. Nejtenčí povrchová oxidová vrstva byla vytvořena během ohřevu ve vzduchu v případě vrstvy s Y. Během ohřevu v He nebyla u vyšetřovaných vrstev pozorována žádná změna hmotnosti až do teploty 1315 °C (v případě vrstvy

$Hf_6B_{12}Si_{29}Y_2C_2N_{45}$ dokonce do 1350 °C). Tvrdost vrstvy $Hf_6B_{12}Si_{29}Y_2C_2N_{45}$ se po ohřevu v He na 1300 °C zvýšila z 22,2 na 25,9 GPa a tato vrstva zůstala opticky průhledná i po ohřevu na 1400 °C. Ke krystalizaci amorfní struktury došlo při teplotě kolem 1400 °C.

Kapitola IV se věnuje závěrům disertační práce. V kapitole V je uveden seznam dalších publikací kandidáta.